Spatial and temporal variability in salinity and tidal flow in a shallow tidal channel

（浅い感潮水路における塩分と潮流の空間的および時間的変動性）

April 2022

Hiroshima University

Nguyen Thi Hiep

ACKNOWLEDGEMENT

I would like to express my sincerest gratitude to my supervisor, Prof. Kiyoshi Kawanishi, who has always supported me throughout my research. He has instructed me how to solve academic research, as well as, interact and develop in international environmental education.

I would also like to gratefully acknowledge my co-supervisors, Prof. Yoshihisa Kawahara, Prof. Tatsuhiko Uchida, for their kind instructions and supports during my research program.

I am particularly grateful to Asst. Prof. Mohamad Basel Al Sawaf, Dr. Cong Xiao, my labmates, and the other students at the Coastal Engineering Laboratory of Hiroshima University for assisting with the field observations.

I must also thank the Vietnamese Government Scholarship Student for the funding support during my PhD's course. Besides, I would like to express my gratitude to Hiroshima University and National University of Civil Engineering (Vietnam) for giving me the chance to study in Japan.

Finally, I give special thanks to my children, my family members who are living in Vietnam for their love, support, and encouragement.

Hiroshima, April 2022

Nguyen Thi Hiep

CONTENT

ABSTRACT

Estuaries are often the transport connection between rivers and the ocean as well as the source of several factors that impact on human life such as food, water consumption, economic, and so on. The results of the interaction between freshwater and saltwater will create a unique environment of each estuary, which affects significantly several estuarine species. Salinity that is the salt amount dissolved in water body and water current caused by the tides from the ocean always change within the time and space. Understanding the mechanisms that control the salinity and tidal flow has an important role in estuarine management.

This work focuses on indicating the spatial and temporal variability in salinity and tidal flow in the Ōta diversion channel which is one branch of the Ōta river system in Hiroshima city, Japan. With the longest distance, large tidal flats, and freshwater run-off is limited by the gates, the Ōta diversion channel becomes the most important branch of the Ōta river system in controlling flood, transportation, economic development, etc. Besides, with the tidal range of 0.5 m to 4 m, the bottom of the Ōta diversion channel is completely submerged at high water and partly dries out at low water, which indicates that the Ōta diversion channel is a shallow tidal estuary.

The present study also aims to examine the performance of the proposed scheme using the FAT system, which is a zigzag configuration in a rectangular tomographic domain of 700 m × 170 m, in terms of providing sufficiently accurate and cost-effective method to estimate riverine characteristics.

Three field observations were conducted during both neap and spring tides in a river segment with the length of 850 m at the central part of the Ōta diversion channel (about 4.5 km from the estuary) to collect the data set of salinity, water temperature, water density, and tidal current. Analyzing these data set results in the spatial and temporal variation of salinity and tidal flow, then the estuarine dynamics will be displayed.

By using the quantity and the depth of stratification layers as well as the surface-to-bottom salinity difference deduced from the transverse and vertical distributions of salinity, the stratification/de-stratification degree is evaluated in a shallow, narrow, and tidal estuary. In detail, it was found that, in the lateral and vertical dimensions, density driven is the main mechanism that controls the stratification in the Ōta diversion channel. Stratification occurs during spring-ebb tides and early of neap-flood tides because of the effect combination of tidal straining, tidal asymmetry and freshwater inflow from upstream, while the lateral distribution of salinity appears during spring-flood tide and the late of neap-flood tides due to the lateral density gradient.

In the longitudinal dimension, it was found that both tidal flow and salinity patterns reveal a completely tide-dominated influence. The tidal flow is asymmetry, mostly due to the interaction of the $O_1 – K_1 – M_2$ tidal constituents; and the topographic effects. The longitudinal dispersion coefficient was

found to increase toward the mouth of the river, and the tide-driven mechanism might be the dominant mechanism in the dispersion process in the study site.

The salinity in the Ōta diversion channel does not response to the water level fluctuations immediately. It was found that there are delays in time between the salinity and water level variations, with the salinity response time lags ranged from approximately 12 minutes to 1.5 hours, corresponding to a phase lag range of 13°–47°. The time lags increase seaward along the channel, and decrease corresponding with the increase of the upstream freshwater release.

Finally, the present research shows that with the lower needed instrument number, the new zigzag configuration of FATs can be an accurate and cost-effective measurement method for monitoring estuarine physics.

CHAPTER 1 INTRODUCTION

1.1 Introduction

Generally, estuary is partially enclosed coastal area where the tide spreads along channels and mixes with fresh run-off water from one or more rivers flowing into them. Thus, estuaries are characterized by both river environments and maritime environments. Also, estuaries are subjects both to fluvial influences such as freshwater and sediment and ocean influences such as tides and saline water.

Estuaries constitute a significant object of several physical processes that vary in time and spatially, including freshwater input, salinity intrusion, and tidal movement. The salinity intrusion, tides propagating, and the interaction of tide and/or wave with fresh run-off water will affect all estuarine activities, including domestic, industrial, agriculture, and aquaculture. Thus, understanding the distribution of salinity and tidal flow along the river as well as river cross-sectional is necessary for water resource management.

1.1.1 The vital role of transverse salinity dynamic

Recently, several types of research on the salinity dynamics and its contributing factors have been done to provide the overall comprehension of the estuarine dynamics. The previous researchers have tried to understand how the freshwater, saline water, and/or tide exchange creates a complex environment. Those previous studies conducted in a various kinds of estuaries, such as a tideless shallow coastal lagoon (Schumann et al., 2006), a deep and narrow

dredged channel (Conroy et al., 2020). Besides, most published studies on salinity dynamics were implemented using numerical models for deep and wide estuaries (Wang et al., 1992, Lerczak & Geyer, 2004, Martyr-Koller et al., 2017). There are fewer studies focused on tidal shallow and narrow estuaries where the interaction between freshwater, saltwater, and tide often occurs very fast. Furthermore, salinity dynamics, mixing mechanisms, and salinity transport downstream in estuaries are convoluted and primarily depend on estuarine characteristics and three-dimension process i.e. estuarine circulation. In a three-dimension structure, the motions in transverse and vertical directions in estuaries are usually smaller than the horizontal motion, but these motions have an essential role in the estuarine dynamics (Lerczak & Geyer, 2004, Hunkins K., 1981). However, the dynamics of lateral salinity in estuaries have not known full well. Thus, a research on salinity dynamic in lateral direction in a tidal shallow estuary is a necessary task in order to understand the estuarine dynamics fully.

1.1.2 The longitudinal distributions of salinity and tidal flow

The ability to accurately estimate the salinity intrusion and mixing in estuaries is critical to coastal engineering and our understanding of estuarine dynamics. Saltwater intrusion is regulated primarily by the tide and river runoff (Laenen & Smith, 1983) and influenced by factors including topography, wind stress, vertical mixing, tidal range, and freshwater flow (Prandle, 2006, Chen et al., 2019, Li et al., 2012). However, the real-time monitoring of river discharge is necessary to analyze the estuary functioning at an adequate level of precision and to obtain accurate measurements of temporal variations in the freshwater inflow regime over spans of time ranging from several minutes to multiple years (Garel & D'Alimonte, 2017).

Continuous and long-term readings of freshwater inputs to estuaries are acquired using stage–discharge rating curves established empirically at upstream gauging stations (K. Kawanisi et al., 2016, Maghrebi et al., 2016). In estuaries influenced by salinity intrusion, estimating the cross-sectional average velocity and discharge from spatial estimation (using limited velocity measurements) is problematic due to the possible distortions in conventional, i.e., log or power law, profiles (Garel & D'Alimonte, 2017).

Most methods of estimating the horizontal distribution of salinity and velocity may be classified as either direct or indirect. For direct methods, information about salinity and velocity is typically collected during field observations using various instruments deployed at several locations within the target site at different time periods (Geawhari et al., 2014, McManus, 2005, Dyer et al., 1992). For indirect methods, one-dimension (1D), two-dimension (2D), or three-

dimension (3D) models are used to simulate the interactions among factors such as river discharge, tidal variation, bathymetry, and wind effect that significantly influence salinity intrusion and mixing mechanisms (Li et al., 2012, Vaz et al., 2005).

However, the current methods of estimating the horizontal distribution of salinity and velocity in estuaries are affected by four limiting factors. First, there are uncertainties associated with freshwater supplementation from sources such as tributaries, localized rainfall, and human activities. Moreover, freshwater loss due to diversion and other causes may significantly reduce the accuracy of discharge and salinity measurement estimates which are not typically addressed in related work. Second, the representation of the spatiotemporal evolution of salinity fields in an estuary is inadequate because of the gaps in time and space in the instrument′s data. Using spatial interpolation from sparse data points to obtain the spatial distribution of salinity and temperature generally results in a low quality of estimation. Third, for numerical and analytical models, insufficient observational data limits the interpretation of sensitivity tests. Thus, a significant challenge is how to apply a suitable theory appropriately to fill the gaps between the model and observations. Fourth, the large number of instruments that must be deployed over a study site to obtain sufficiently accurate field data, and analysis results adds significantly to the overall cost of the system. For example, (Vaz et al., 2005) used ten instruments to collect the water temperature and salinity from an 11 km long study site. Thus, a cost-effective measurement method that is able to provide accurate and beneficial information on estuarine physics is needed.

The fluvial acoustic tomography (FAT) system, developed at Hiroshima University in 2008, is a highly versatile hydro-acoustic system for investigating hydrological and hydraulic processes. In prior research, the FAT system was used to estimate continuous long-term river flow and streamflow direction (K. Kawanisi et al., 2018, Bahreinimotlagh et al., 2016) to map the horizontal velocity of the current field in a depthless river (Xiao et al., 2021, Razaz et al., 2015), and to measure minimal flow rates in extremely shallow streams (Al Sawaf et al., 2020). Based on the above, FAT is a valid system for measuring river discharge and exploring various advanced applications in the water resources domain. An aim of this study is to examine the performance of the proposed scheme using the FAT system in terms of providing sufficiently accurate estimates of river discharge in tidal estuaries. The significance of this work is its exploration of the results of examining the cross-sectional average stream velocity in both landward and seaward directions.

However, most published studies on salinity intrusion, stratification, estuarine circulation, and salinity flux that employed FAT were implemented using a traditional scheme that included an oblique transmission line and several FAT units. A new FAT deployment pattern is proposed to investigate the longitudinal distribution of salinity and tidal flow in a tidal shallow channel. That method is expected to expand and improve the unique ability of FATS in monitoring estuarine physics. Thus, a research that can apply the new FAT schemes in a real estuary is necessary.

1.2 Objectives and challenges

1.2.1 Challenges

Firstly, the Ōta River system, located in Hiroshima city, Japan has a vital role in its transportation and ecosystem, with a coastal ecosystem for many tidal species. Changing salinity is one of the most important factors affecting the productivity aquaculture and agriculture. The Ōta River system consists six branches, in which the Ōta diversion channel is the longest and largest one (see Fig. 2.1). With the largest width and the extensive tidal flats, the Ōta diversion channel has the important role in the transportation and flood control. Furthermore, the gates located in the upstream area limited the freshwater flow, which creates the low freshwater status, and influences the salinity intrusion in the Ōta diversion channel, resulting in large change of water depth and salinity. Thus, the salinity variation in the Ōta diversion channel is the one of the important factors that influence the Ōta River system activities such as domestic, ecosystem, industrial. To understand the salinity dynamics in the Ōta diversion channel is a crucial task. That is why the Ōta diversion channel is chosen to be the observation site.

To clarify the salinity dynamic process in the Ōta diversion channel, the following important questions need to be answered: 1) How is the stratification formed? 2) How and why do the stratification layer depths (see Chapter 2, Section 2.5.1) change? and 3) What are the main controls on stratification in the Ōta diversion channel?

Secondly, a cost-effective measurement method able to provide accurate and beneficial information on estuarine physics is needed. A new method is proposed (see Chapter 1, Section 1.1.2) in order to solve those challenges. There are two important questions related to that proposal method needed to be answer: (1) Can an alternative configuration of FAT acoustic stations improve flow direction measurement capabilities and cover a wider measurement area

at a relatively lower cost? (2) What is the accuracy of the proposed FAT deployment and what are the associated challenges/difficulties?

1.2.2 Objectives

In view of these challenges mentioned above, the objectives of this study are:

- To examine how the saline water mixes and exchanges with freshwater through a dynamic process in the Ōta diversion channel, which is the tidal shallow and essential channel in the Ōta River system in Hiroshima city, Japan;
- To apply the new FAT deployment to investigating the longitudinal distribution of salinity and tidal flow in a tidal shallow channel;
- To examine the performance of the proposed scheme using the FAT system in terms of providing sufficiently accurate estimates of river discharge in the mesoscale estuary: the Ōta diversion channel, in Hiroshima, Japan as a case study;

1.3 Outline of the thesis

The thesis is divided into four parts, including introduction (see Chapter 1); the transverse and vertical distribution of salinity (see Chapter 2) and longitudinal distribution of salinity and tidal flow (see Chapter 3) of the Ōta diversion channel; the summary conclusions and recommendations (see Chapter 4).

Chapter 1 shows the general introduction, the information of the study site, challenges and objectives of the study. It also presents a brief introduction of estuaries, tides propagating, salinity intrusion and the interaction between freshwater and saline water.

Chapter 2 presents a method to clarify the salinity dynamics in a shallow and narrow estuary, based on the stratification layer. Chapter 2 investigates the vertical and lateral distribution of the salinity. Chapter 3 shows the longitudinal distributions of tidal flow and cross-sectional average salinity. Chapter 4 shows the recommendations and conclusions of the study. The recommendation section presents the further research based on the limitation of the present study. The conclusions summarize and reflect on the research, it also shows what new knowledge the present study has contributed.

CHAPTER 2 VERTICAL AND LATERAL DISTRIBUTIONS OF SALINITY AND DENSITY

2.1 Introduction

The motions of transverse and vertical directions in estuaries are usually smaller than the horizontal motion, but these motions have an essential role in the estuarine dynamic (Fischer, 1976, 1972). Several studies have increased attention on longitudinal structures of salinity and flow, and the limitation of that approach was also noted by Fischer (1972, 1976). To fully understand the dynamic process of an estuary, the complete three-dimensional description of the estuary need to be presented. Thus, the understanding requirement of the transverse and vertical structures of salinity and density is crucial. The degree of salinity and density stratification in single cross sections has important role in vertical mixing mechanism. To clarify how does a shallow and narrow estuary develop and break the stratification will give a better understanding of the estuarine dynamics.

The Ōta Diversion channel is the largest branch in the Ōta River system, which is the most crucial river in Hiroshima city, and has a vital role in its transportation and ecosystem (Gotoh et al., 2013). Flow rate and salinity intrusion (K. Kawanisi et al., 2015, Soltaniasl et al., 2013), salt flux variability, and water circulation (Soltaniasl et al., 2013), were investigated to examine the estuarine dynamic in the Ōta River estuary. Soltaniasl (2013) used the gradient Richardson number and the stratification parameter that is a dimensionless variable to evaluate the stratification variation in the Ōta River estuary around a high tide

during the period of four hours. Their research contributed an important finding to the stratification mechanism understanding in the Ōta River estuary during the later period of the spring tide. The results show the tidal mixing contributes to decreasing the stratification over the whole cross-section. However, in order to fully understand the stratification process, and thus the lateral salinity dynamics, investigations of salinity distribution in the cross sections during a tidal cycle are needed.

The present research investigates vertical and lateral salinity variations over a tidal cycle in both spring tide and neap tide. This research aims are to examine how the saline water mixes and exchanges with freshwater through a dynamic process in the Ōta diversion channel, which is the tidal shallow and essential channel in the Ōta River system in Hiroshima city, Japan. This study is expected to answer the important questions, including 1) How does the stratification form? 2) How and why do the stratification layer depths (see Chapter 2, Section 2.5.1) change? and 3) What are the main control factors on stratification in this area? By discussing these questions, the transverse salinity dynamics in the Ōta diversion channel will be clarified.

2.2 Study area

2.2.1 Ōta diversion channel

The Ōta River diversion channel in Hiroshima City, western Japan, is the monitoring site used in this study. The diversion channel is a tidally dominated channel with floodgates located around 9 km upstream from the mouth that restricts the freshwater runoff from further upstream. The bathymetry of the Ōta diversion channel shows a typical shallow estuary that is presented in several previous studies (Robins & Davies, 2009): whole bottom is submerged at high water and part of bottom dries out at low water. The estuary has irregular bathymetry with extensive tidal flats and significant variations in the cross-sectional profiles (Gotoh et al., 2013). The mixed tides in this estuary include diurnal and primary semidiurnal components, and the tidal range at the river mouth ranges from 1.2 m at the neap tide to about 4 m at the extreme spring tide. The Ōta River has vital environmental characteristics, with an ecosystem for many tidal species, a large portion of which are oysters in the downstream area.

The freshwater runoff is controlled by the Gion sluice gates (see Fig. 2.1) located 4.5 km upstream from the observation site. During the observation period, the Gion sluice gates

were operated under normal conditions, with only one of the three gates partially open and a cross-sectional stream area of 32 m × 0.3 m for the spilling flow (Kawanisi et al., 2010).

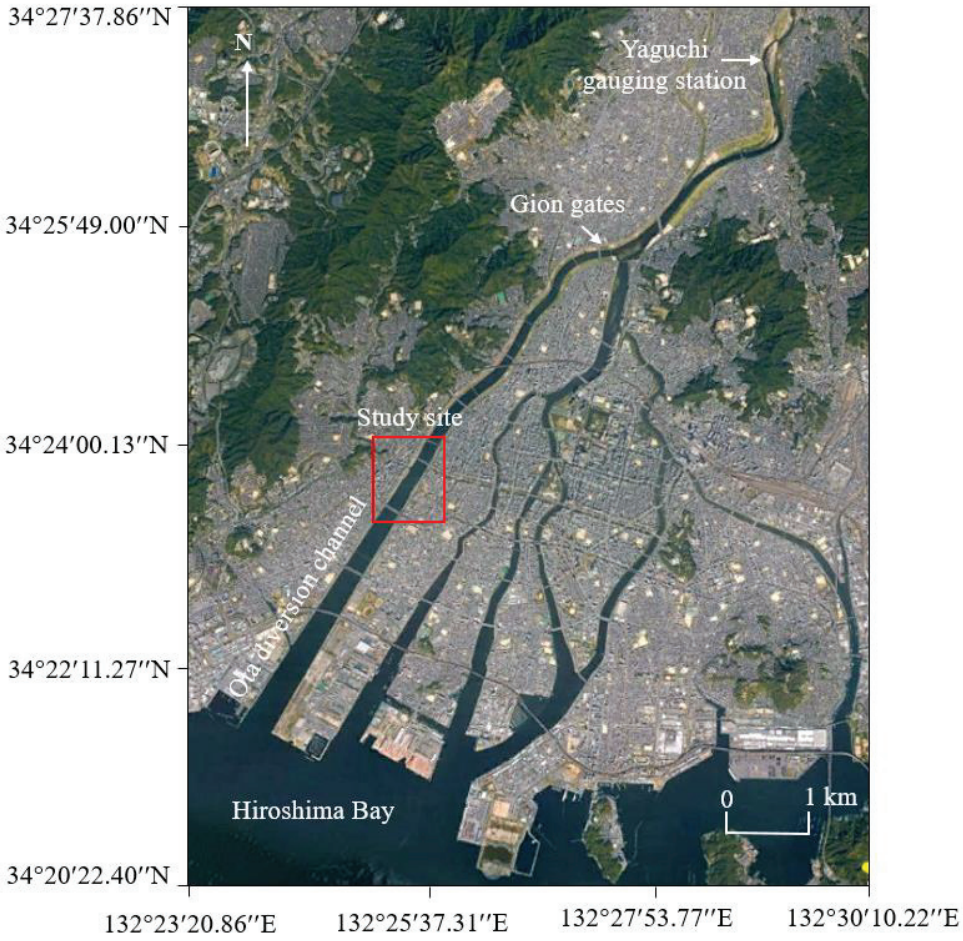

Figure 2.1 The detail of the study site

Figure 2.2 shows the bathymetry distribution of the Ōta diversion channel, based on the data set of a remote controlled boat campaign in 2019 (see Chapter 2, Section 2.3.3). The bathymetry of the Ōta diversion channel shows the complicated distribution. The shape of the river bed varies slightly at the middle section, and fluctuates significantly near the river mouth and the meandering location.

2.2.2 Study area

Figures. 2.1 and 2.3 illustrate the location of the study site and the detail of the observation area, respectively. It is located around 4.3 km upstream from the river mouth. The research′s experiments were conducted in the river segment between two bridges (Asahi Bridge and Shinkoi Bridge); the distance between the two bridges is approximately 850 m.

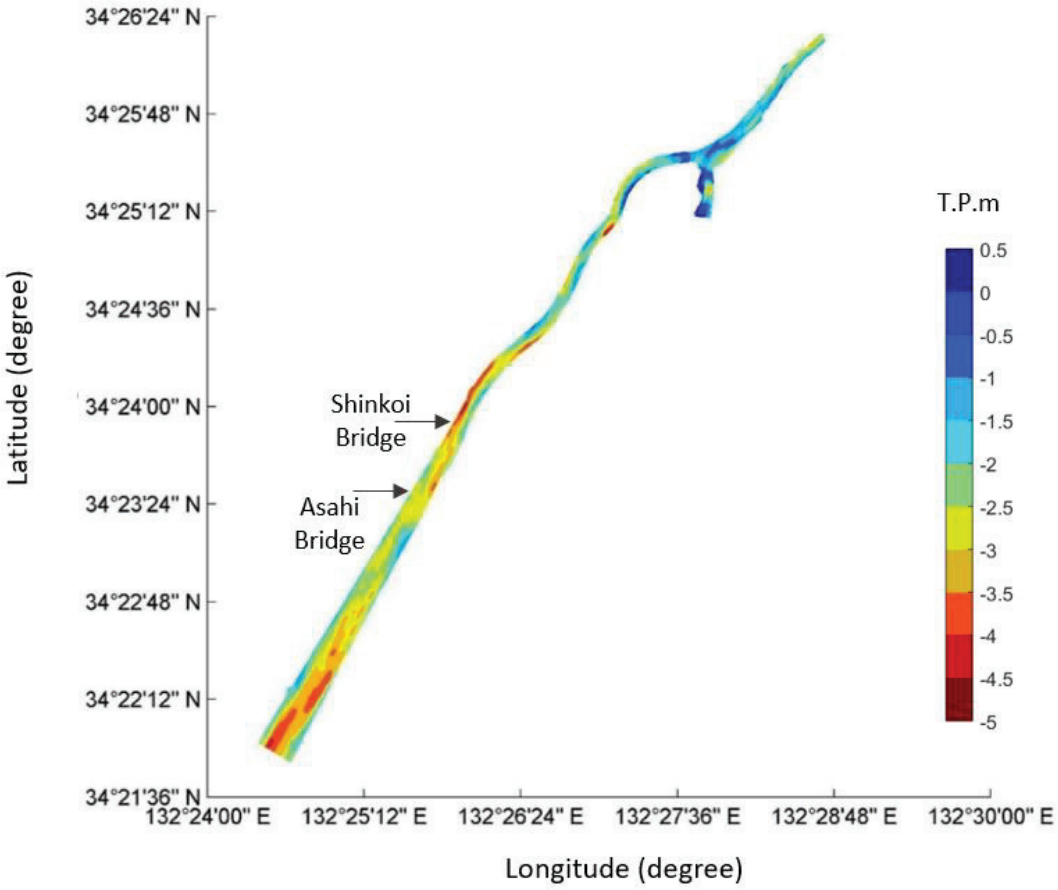

Figure 2.2 The bathymetry distribution of the Ōta diversion channel *(Gusti & Kawanisi, 2020)*

Figure 2.3 The detail of the study site

The bathymetry distribution of the observation area is presented in Figure 2.4. It can be seen that, the left riverbank side is deeper than the right riverbank side on the middle of the channel segment, and the right bank side is deeper than the left bank side at the areas near to the two bridges (Shinkoi Bridge and Asahi Bridge), resulting in a meandering in the observation site.

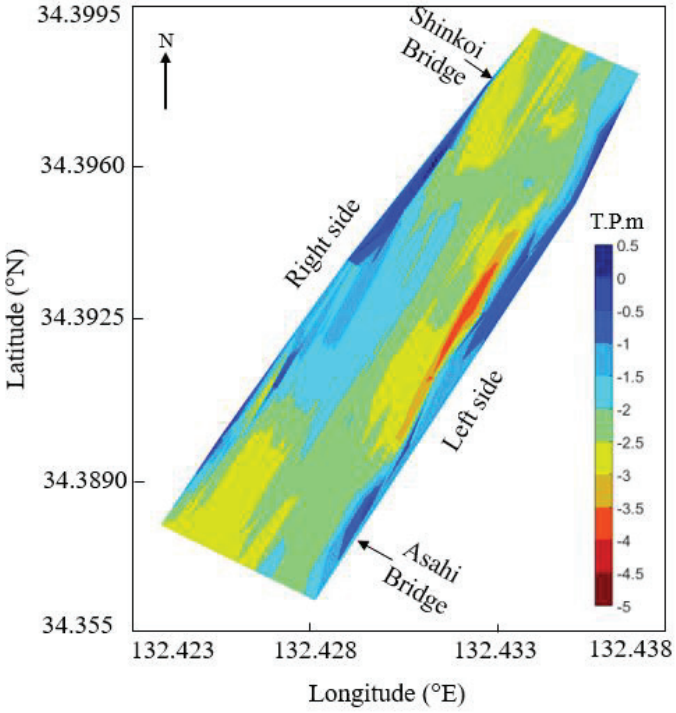

Figure 2.4 The bathymetry distribution of the observation site

2.3 Instrumentations

2.3.1 Compact CTD (Conductivity, Temperature, Depth) sensor

Compact-CTD is a small & light-weight temperature/salinity/depth logger. The compact titanium pressure case, carrying 60 mm in diameter, 462 mm in overall length & light weight of 1.0 kg. In water provides optionally the chlorophyll/turbidity sensor and this instrument is appropriate to multi-parameter water-quality measurement. The system is comprising of sonde unit with sensors, interface unit and communication cable, and is designed so as to proceed the measured data and do various setups through PC. This Compact-CTD newly features a time-trigger function in addition to a depth-trigger provided on our conventional memory CTD.

Figure 2.5 Compact CTD (Conductivity, Temperature, Depth) sensor (*Source: JFE advantech Co., Ltd*)

Table 2.1 Compact-CTD specifications (*Source: JFE advantech Co., Ltd*)

Sensor	Type	Range	Resolution	Accuracy	Time constant
Depth	Semiconductor Pressure sensor	0 – 600 m	0.01 m	0.3 % FS	0.03 sec.
Temperature	Thermistor	-5 – 40 °C	0.001 °C	±0.02°C	0.15 sec.
Salinity (Conductivity)	UNESCO Formula Inductive cell	0 –40 0 – 60 mS/cm	0.001 0.001 mS/cm	±0.03 ±0.05 mS/cm	0.15 sec.

2.3.1.1 Depth sensor of CTD

This is a type of absolute pressure detection and also affected by fluctuation of atmospheric pressure. Moreover, the zero-point is loosing off a little bit due to environmental temperature variation. For those, this sensor provides an automatic zero-point function and executes an automatic compensation in order to clear the error factors caused by the change of atmospheric pressure and temperature variation. Pressure portion of depth sensor is

protected by white polyacetar resin cap with small holes. When the holes, therefore, are choked, the pressure transmission is affected, so it is recommended to clean here regularly.

2.3.1.2 Water temperature sensor of CTD

High-reliable & fast-responding thermistor sensor is used and this sensor is unified with electric conductivity sensor to let the response time match each other. This mechanism is to avoid the salinity spike generated when the data are analyzed. Since this sensor is very much stable, there might not be much affection for temperature measurement even if the dirt and bio-fouling are occurred, but clean up the sensors regularly as the response speed becomes slow due to heavy dirt. Pay your special attention to the damage of the sensor since it is very thin.

2.3.1.3 Electric conductivity sensor of CTD

The conductive rate adjacent to the sensor is measured based on the electromagnetic inductive method. Hence, in case something is existed beside the sensor, it affects much to the measurement. Moreover, the accuracy becomes inferior for the dirt fouling, so it is recommended to clean up the sensor by brush, etc. regularly, especially the inner of ceramic tube of the inductive cell.

2.3.2 Fluvial Acoustic Tomography (FAT) system

The FAT is an advanced hydro-acoustic instrument designed by Hiroshima University that uses submerged acoustics to observe various hydrological properties of rivers at levels ranging from 0.28 m to 10 m in depth. FAT emits omnidirectional acoustic signals at different central frequencies (mainly between 7–53 kHz). The FAT system contains GPS receivers that help synchronize both FAT units to guarantee the high-precision transmission of pulses. The periodicity of acoustic pulses was 30 secs, synchronized with a GPS clock.

FAT uses the time-of-travel tomography method and can be used for the long-term measurement of the velocity and salinity in both freshwater and tidal rivers (Kawanisi et al. 2011; Kawanisi et al. 2010).

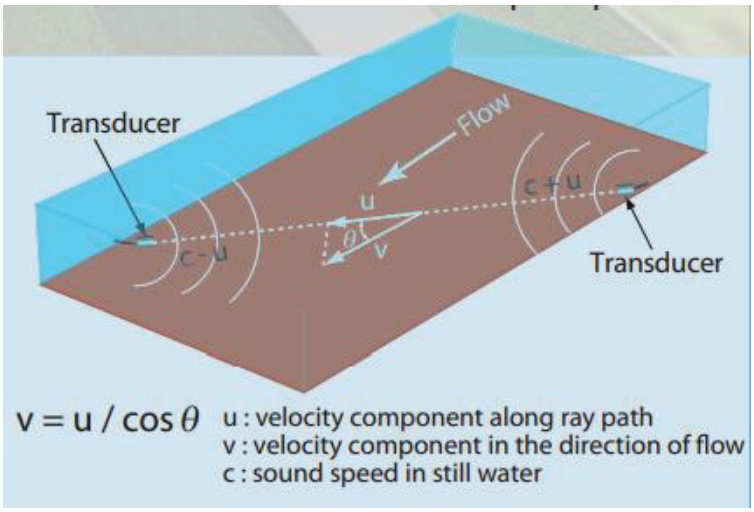

Figure 2.6 The scheme and principle operation of the FAT system ((K. Kawanisi et al., 2010))

2.3.3 Hydrographic survey remote controlled boat RC-S3

The hydrographic survey remote controlled boat RC-S3 was developed by Coden Co., Ltd to collect depth data; the depth range is 0.5 – 80 m. The boat is equipped with GPS and echo-sounder, it allows transfer obtained data together with GPS data real-time to the PC receiver (hereinafter base station). The surveying points of 225 and/or measuring lines of 128 can be pre-set.

Table 2.2 Remote controlled boat RC-S3 specifications (*Source: CODEN Co.,Ltd*)

1. Boat	
Length	1.200 mm
Width	350 mm
Height	250 mm (excluding antenna)
Weight	13 Kg (16 Kg with batteries)
2. Echo Sounder	
Frequency	200 KHz
Depth range	0.5 m − 80 m

Resolution	0.01 m
3. GPS	
Positioning accuracy	SBAS (< 0.5 m)
Positioning resolution	1/10000 sec (about 0.03 m)

In the present research, authors used this boat to collect the bed altitude of the Ōta diversion channel (see Figs. 2.2 and 2.4).

2.4 Methodology

2.4.1 Salinity and density data set collection

The information of salinity was collected from two cross-channel transects in the middle Ōta diversion channel using two CTD campaigns.

The first campaign was conducted from 14:00 to 17:00 on September 5th, 2018, during neap tide. This work was done simultaneously along two bridges, Asahi Bridge and Shinkoi Bridge. The distance between the two bridges was approximately 850 m (see Fig. 2.7). In this campaign, the vertical salinity distributions were measured at five points every thirty minutes along the 150 m length of Shinkoi Bridge and the 200 m length of Asahi Bridge, respectively (see Fig. 2.7).

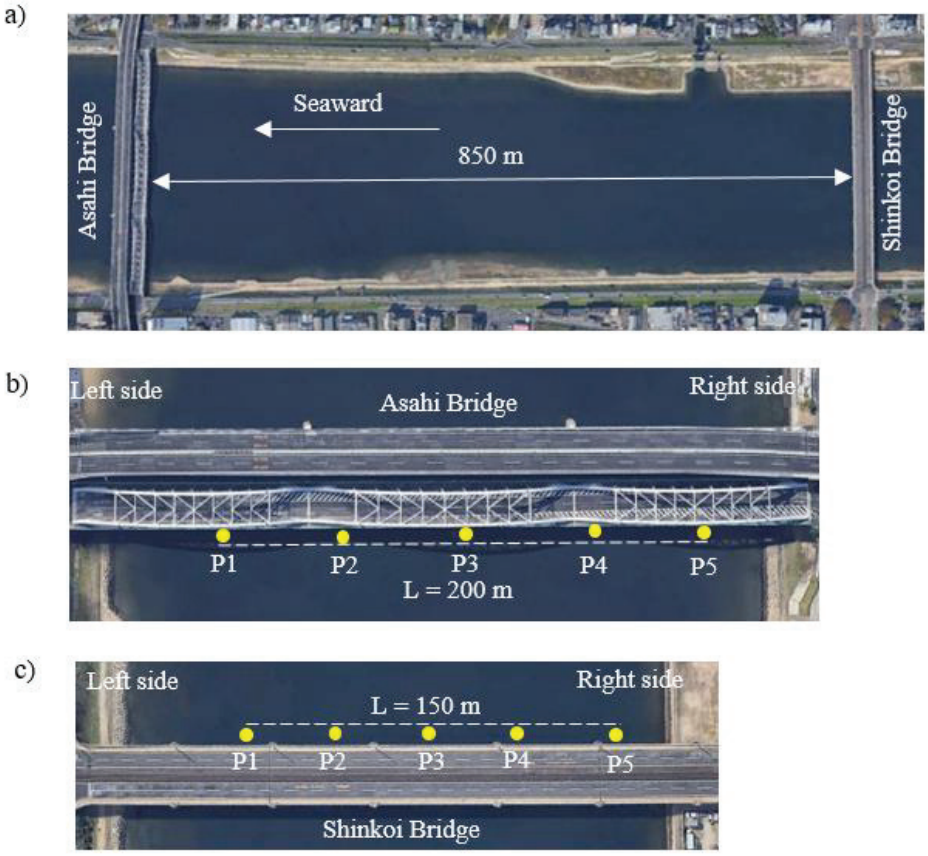

Figure 2.7 a) The observation site for the first campaign; b) and c) the transverse lines of Compact CTD measurement, yellow symbols indicate the locations of the data collected points (P_1–P_5)

The second campaign was operated on October 2nd, 2020, from 8:00 to 23:30, during spring tide at Shinkoi Bridge, in which Compact CTD ran at six points along the 150 m length of the bridge every thirty minutes (see Fig. 2.8). Besides, two FAT units were deployed on the left and right sides of the river near Shinkoi Bridge with a transmission length of 160 m for four days, from October 1st 2020 to October 5th 2020. The purpose of using FATS here is to collect the data to estimate the section-average salinity. The combination of the cross-sectional average salinity deduced from FAT data and vertical structure of salinity by the CTD will bring the clearly understanding of transverse salinity dynamics in Ōta diversion channel.

The purpose of the data collection by iterating the channel intersects is to acquire the distribution of salinity, temperature and density in the cross section. The first campaign was conducted at two parallel transects separated by 850 m in three hours while the second

campaign was conducted at one transect in 16 hours during one tidal cycle. Thus, the data were ensured good quality to determine the transverse and vertical structures.

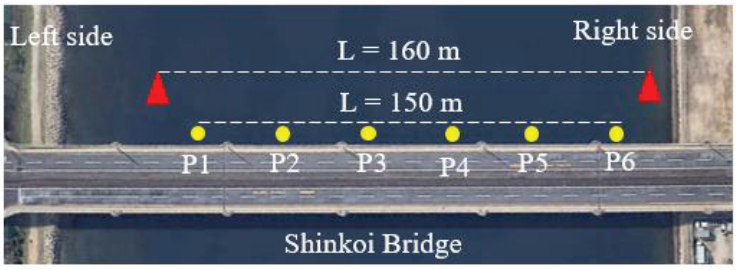

Figure 2.8 The observation site for the second campaign; yellow symbols indicate the locations of the data collected points (P_1–P_6) by Compact CTD, red triangles indicate the locations of FATS.

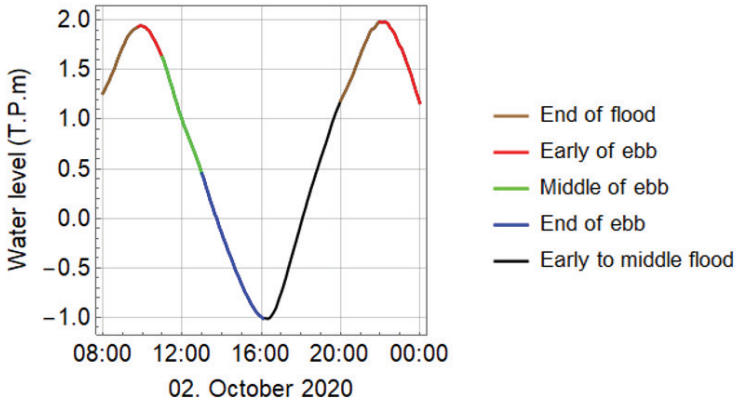

Figure 2.9 Seven stages of the second campaign

The more extended campaign was divided into seven stages (see Fig. 2.9) for further clarification, they are the end of the flood of the first tide, early in the ebb of the first tide, middle of the ebb, the end of the ebb, early to middle of the flood, the end of the flood of the second tide, and early in the ebb of the second tide. The stage classification is based primarily on the pattern of the salinity distribution in the cross section. During the observation period, the times that show the similar pattern of salinity distribution in the cross section will be grouped into the same stage. For the present research, the quantity and the depth of stratification layers, and the surface-to-bottom salinity difference were used to evaluate the stratification/de-stratification degree.

2.4.2 Fluvial Acoustic Tomography (FAT) system

2.4.2.1 Estimating sound speed using FATS

FAT uses the time-of-travel tomography method. The speed of sound (c) is evaluated based on respective travel times, (t_{up}) and (t_{down}), at the upstream and downstream stations, as follows:

$$c = \frac{L}{2}\left(\frac{1}{t_{up}} + \frac{1}{t_{down}}\right) \tag{2.1}$$

2.4.2.2 Estimating depth- average salinity using FATS

As described by Medwin (1975), the speed of sound in water is generally a function of salinity, water temperature, and depth:

$$S = 35 + (c - 1449.2 - 4.6T + 0.055\,T^2 - 0.00029\,T^3 - 0.016\,D)/(1.34 - 0.01\,T) \tag{2.2}$$

where T is water temperature (°C), c is speed of sound (m/s), and D is depth (m). The valid parameter ranges in Equation 2.2 are as follows: $0 \leq T \leq 35$ °C, $0 \leq D \leq 1000$ m, and $0 \leq S \leq 45$. This relationship helps estimate the cross-sectional average salinity using the speed of sound in water computed by the FAT system.

2.4.3 Freshwater discharge data

The present study also discusses the effects of freshwater discharge on salinity and density distribution. Thus, the information of freshwater flow was also presented in this chapter. There is a Yaguchi Gauging Station that is located at approximately 14 km upstream from the river mouth (see Fig. 2.1).

From the previous studies (Kawanisi et al., 2010), during normal conditions, the freshwater rate at Ōta Diversion channel counts approximately 10 ÷20 % of the total river discharge of the Ōta River.

The Yaguchi Gauging Station is not tidally modulated, as a result, the freshwater discharge in October 2020 can be deduced by using the rating curves as below:

$$Q_{YI} = 102.44\,(H+0.05)^2;\ H \leq 0.92 \text{ m} \tag{2.3}$$

and

$$Q_{Y2} = 84.65\ (H+0.22)^2;\ H > 0.92\ \text{m} \tag{2.4}$$

where Q_{Y1}, Q_{Y2} (m^3/s) are discharges and H is water level (T.P. m). T.P is the average water level in Tokyo Bay.

Figure 2.10 shows the freshwater discharge recorded at Yaguchi Gauging Station as the results of using rating curve method.

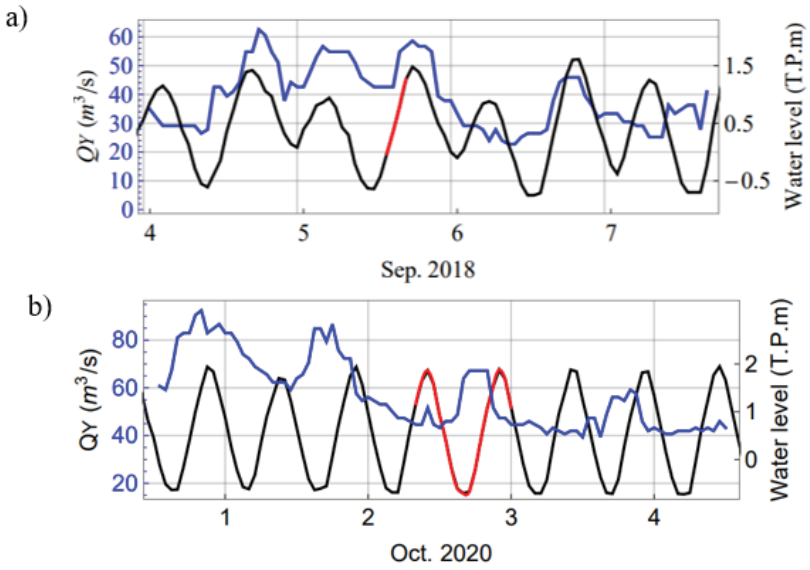

Figure 2.10 Temporal variations in freshwater discharge at Yaguchi Gauging Station (blue line), the water level at the observation site (black line), and the studied periods (red line) for a) the first campaign and b) the second campaign

2.4.4 Cross-correlations

Cross-correlations is the term that denotes the correlations between two time series in different space or times, and is used to measure the degree of similarity between them. One of the valuable applications of the cross-correlation is to investigate the time delays. Calculating the cross-correlation will return the maximum of the cross-correlation function (see Eq. 2.5), which points clearly to the time in which these two time series are best matched, and indicating the time delay between them.

The cross-correlation function between two independent time series is defined as follow:

$$R_{X,Y}(\tau) = \frac{E(X_{t+\tau} - \bar{X})(Y_t - \bar{Y})}{\sqrt{Var(X_{t+\tau})Var(Y_t)}} \tag{2.5}$$

where X,Y are the random variables, t is the time, τ is the displacement, also known as *lag*. The overbar refers the value of the variable mean. *Var* means the variance, and E is expected value.

2.5 Results

2.5.1 Salinity distributions in the cross section

Results from two campaigns show the different range of stratification conditions observed between spring tide and neap tide as well as between ebb and flood tide conditions in the Ōta River as shown in Figures. 2.11, 2.12, 2.13 and 2.14. Stratification highly develops during ebb tide periods while de-stratification occurs during higher flood tides. The stratification degree is stronger during neap tide than during spring tide.

In the present research, the salinity contours in all mentioned figures are showed with the step of one psu. Thus, the terms "stratification layers" and "stratification layer depth" are considered basing on the one-psu-difference contour of salinity.

2.5.1.1 Spring tide (the first campaign)

A. The ebb stages

The salinity distribution in the cross section of the ebb stages during spring tide, including early in the ebb of the first tide, early in the ebb of the second tide, the middle of the ebb, and the end of the ebb are shown in Figures. 2.11, 2.12, 2.13 and 2.14, respectively. Overall, the figures of ebb stages revealed a complete stratification, with the stratification degree increasing sharply from the early to the end of the ebb tide.

The early part of the ebb stages

Figure 2.11 shows there are five significant stratification layers at the beginning of the stage, with corresponding salinity ranges from 26 ÷ 31psu (see Fig. 2.11a). There was a sharp difference in depth of these stratification layers; the saltiest layer (above 30 psu) had the highest depth of approximately 2 m, while the total depths of the remaining layers are approximately 1 m. The number of these significant layers increased, and thus their depths decreased at the end of the stage, however, the depth of the saltiest layer was always higher than the total depths of the remaining layers. A similar phenomenon was also found in the early part of the ebb of the second tide (see Fig. 2.12). This phenomenon suggests that at the

beginning of ebb tide, the stratification occurred more strongly at the surface than in the middle and bottom parts of the water column.

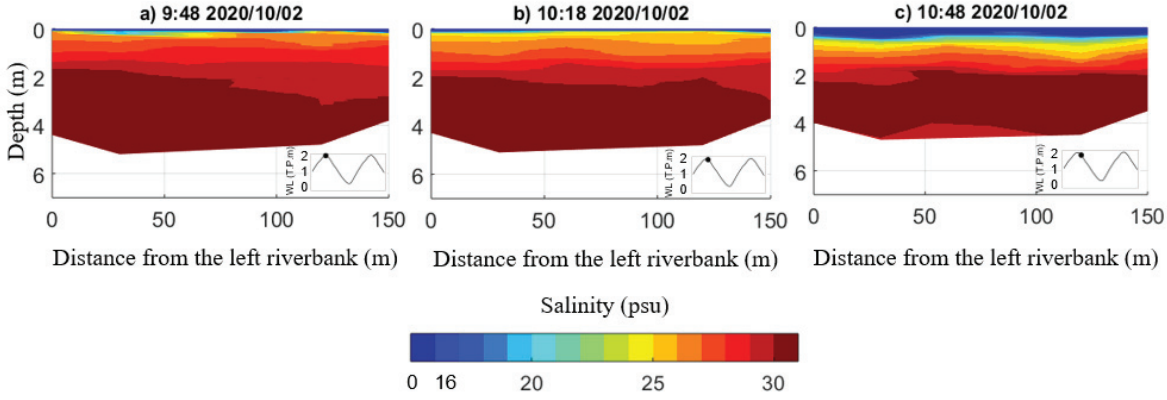

Figure 2.11 Salinity distributions in the cross section of the early ebb during spring tide (the first tide stage)

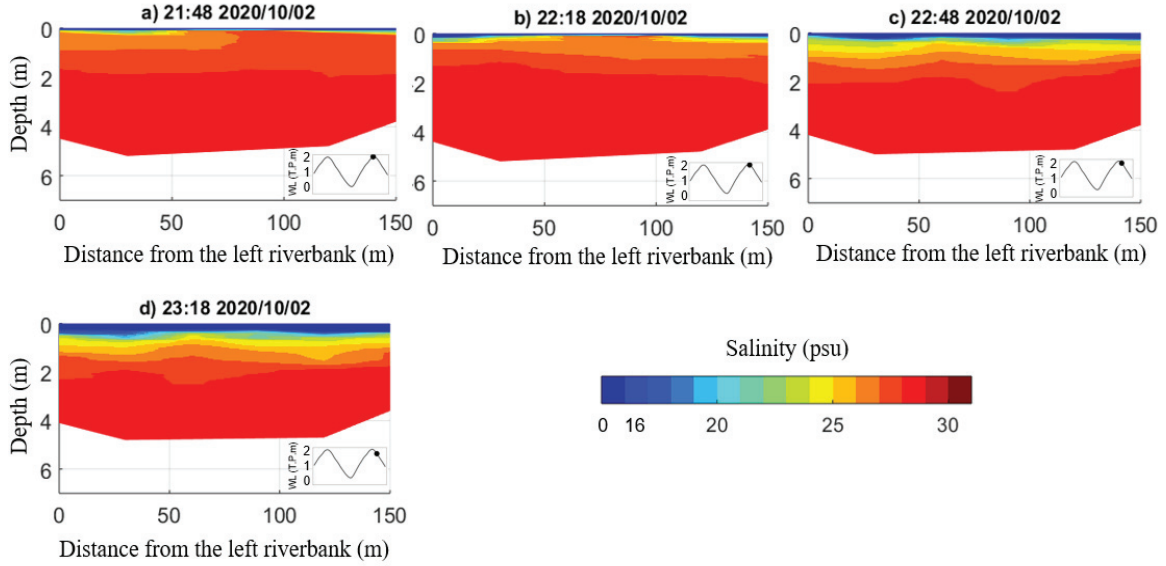

Figure 2.12 Salinity distributions in the cross section of the early ebb during spring tide (the second tide stage)

The mid ebb and the end of ebb stages

The stratification continues to rise during these stages. The end of the ebb stage presented the highest number of stratification layers over the observation period (see Figs. 2.14c and 2.14d), which suggests that the strongest stratification happened at the end of ebb tide period. In the middle of the ebb stage, the depth of the saltiest layer (above 29 psu) is still high,

approximately 1.5 m (see Fig. 2.13a), and dropped down gradually during the first half of the ebb tide (see Figs. 2.13b and 2.13c). However, it fell more rapidly during the last half of the ebb tide (see Figs. 2.13d, 2.13e and 2.13f).

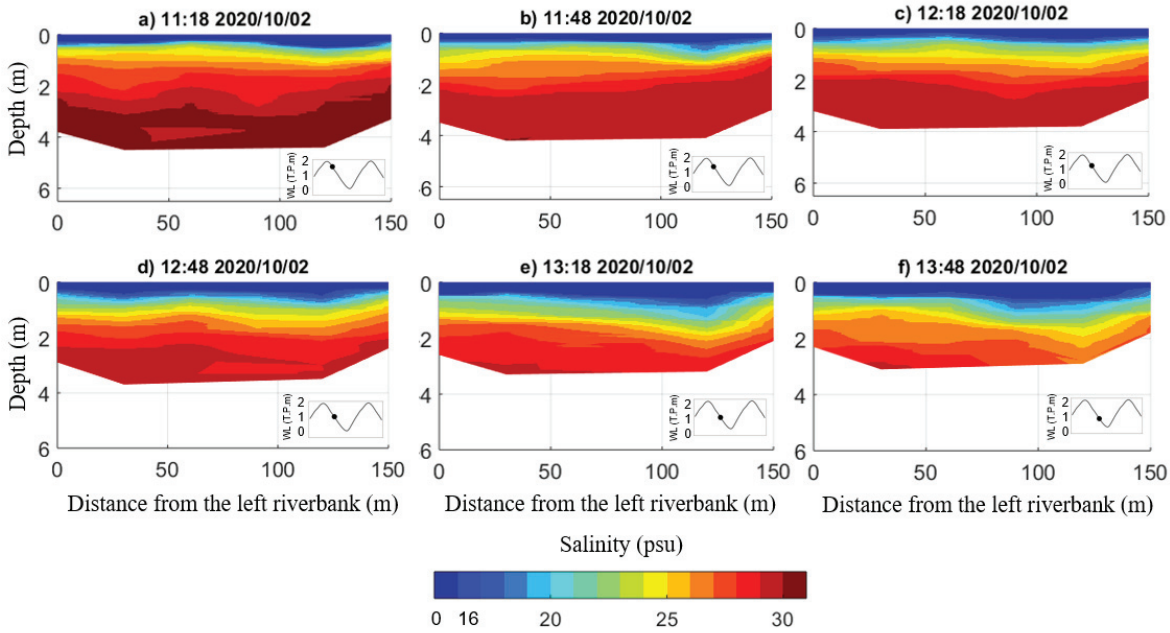

Figure 2.13 Salinity distributions in the cross section of the middle ebb stage during spring tide

The last figure of the middle of ebb tide (see Fig. 2.13f) and the first one of the end of ebb tide (see Fig. 2.14a) also show an equal depth for all significant stratification layers, approximately 0.2 m. After that, the depth of the layers that were in the middle of the water column increased twofold while the depth of the layers located on the bottom decreased rapidly (see Figs. 2.14 b, 2.14c, 2.14d, and 2.14e). During the end of the ebb and early stage of flood tide (see Fig. 2.14f), the depths of the significant stratification layers become almost equal again. The depth variation of the significant stratification layers suggested that the stratification developed gradually from the surface to the bottom of the water column over the ebb tide period.

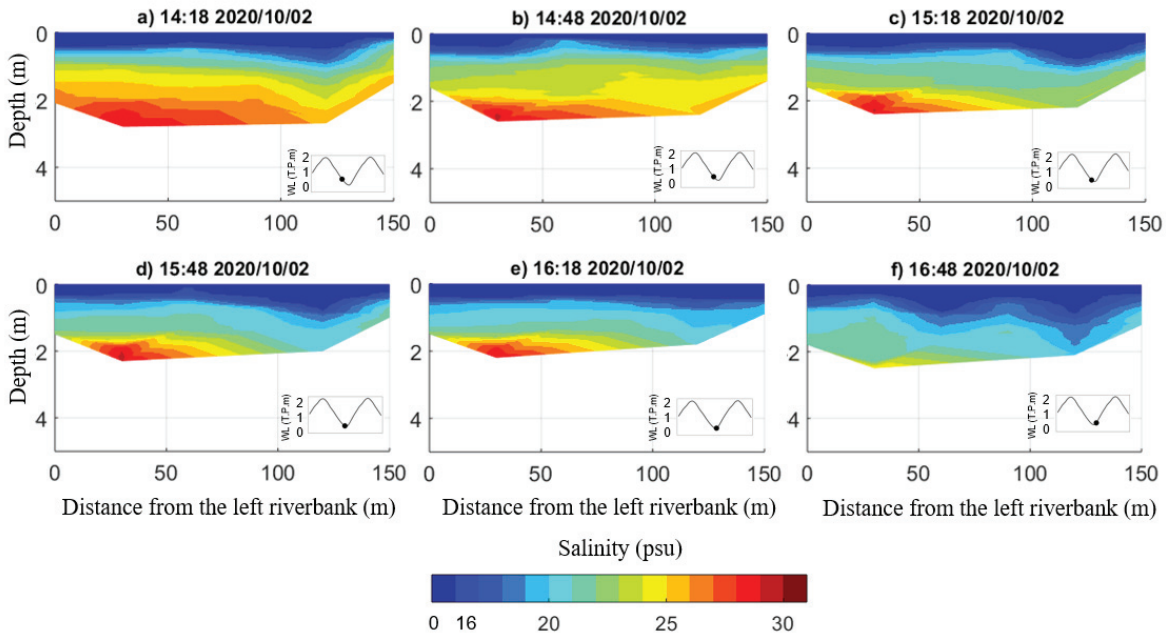

Figure 2.14 Salinity distributions in the cross section of the end ebb stage during spring tide

B. The flood stages

The plots of the surface-to-bottom salinity of the flood tides during spring tide, including the end of the first flood tide, the end of the second flood tide, and the early to middle flood are shown in Figures 2.15, 2.16, and 2.17, respectively. These figures revealed the main trend of the salinity dynamic during flood tide, which is that the salt wedges moved from the left side to the right side of the river, resulting in the lateral distribution of salinity. The salinity distribution in the cross section is not symmetric, as the water was fresher on the right side than on the left side. This might be because of the influence of bathymetry, which will be discussed in the following parts. The plots of salinity distribution over the cross-sectional during flood stages also show a high de-stratification rate, essentially for the early flood stage.

The early to middle flood stage

This stage showed a complete lateral salinity distribution. The lateral salinity gradient was highest at the beginning of the stage (see Fig. 2.17a) close to the previous ebb, decreasing during mid flood and increasing again during the late flood tide (see Fig. 2.17f). The difference in advection of the longitudinal salinity gradient during flood tide is claimed to intensify the force of lateral density gradients, thus increasing the lateral salinity gradient.

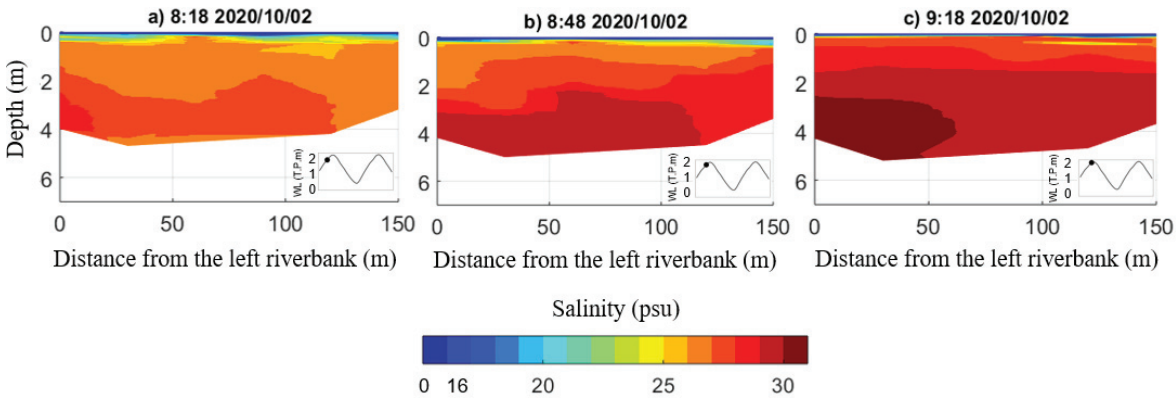

Figure 2.15 Salinity distributions in the cross section of the end of the first flood tide during spring tide

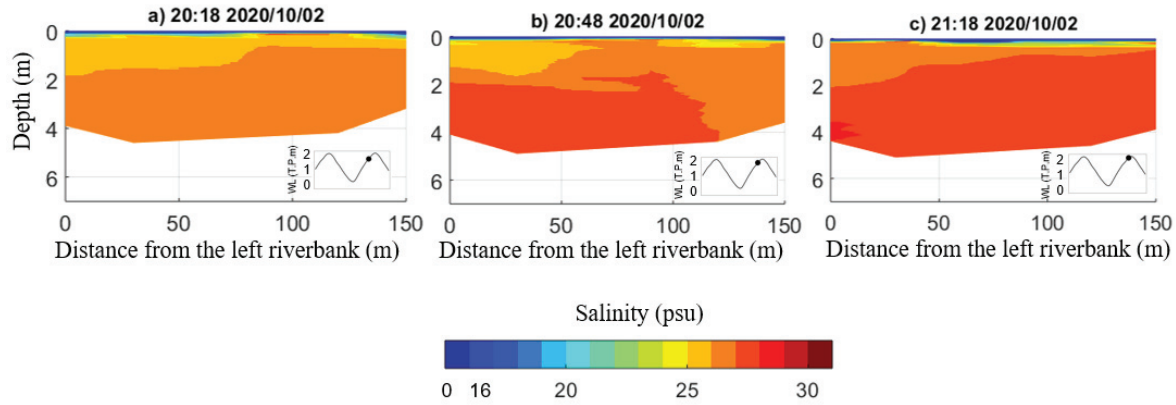

Figure 2.16 Salinity distributions in the cross section of the end of the second flood tide during spring tide

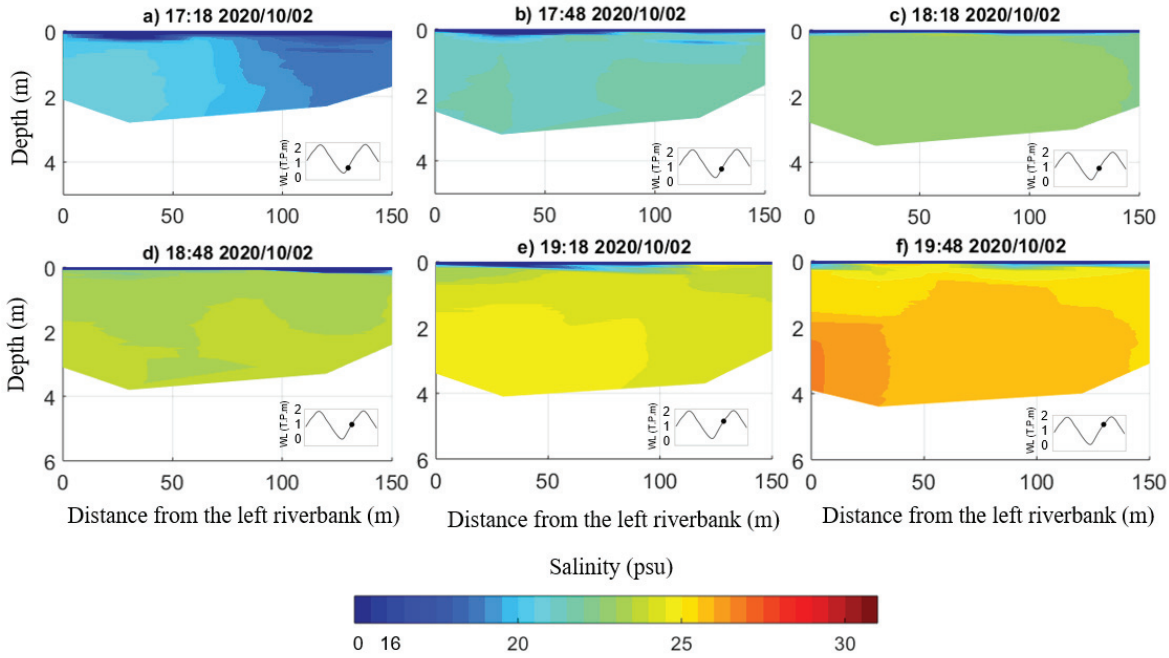

Figure 2.17 Salinity distributions in the cross section of the early to mid flood stage during spring tide

2.5.1.2 Neap tide (the second campaign)

Vertical profiles of salinity at the cross-sectional estimate by CTD

Figures 2.18 and 2.19 show the vertical salinity profiles at five points, P_1 – P_5 (see Fig. 2.7b and 2.7c) at the Shinkoi Bridge and Asahi Bridge during the flood neap tide, respectively. In general, the surface-to-bottom differences of salinity in both upstream and downstream areas are similar and not too big during the observation period, with value of approximately 5 psu. That means the vertical salinity gradients at the observation site are small. The surface salinities recorded at the observation site are almost approximately 20 psu, and the bottom salinity values are around 25 psu. The highest salinity is found at the point P2 that is located on the left side of the river bank.

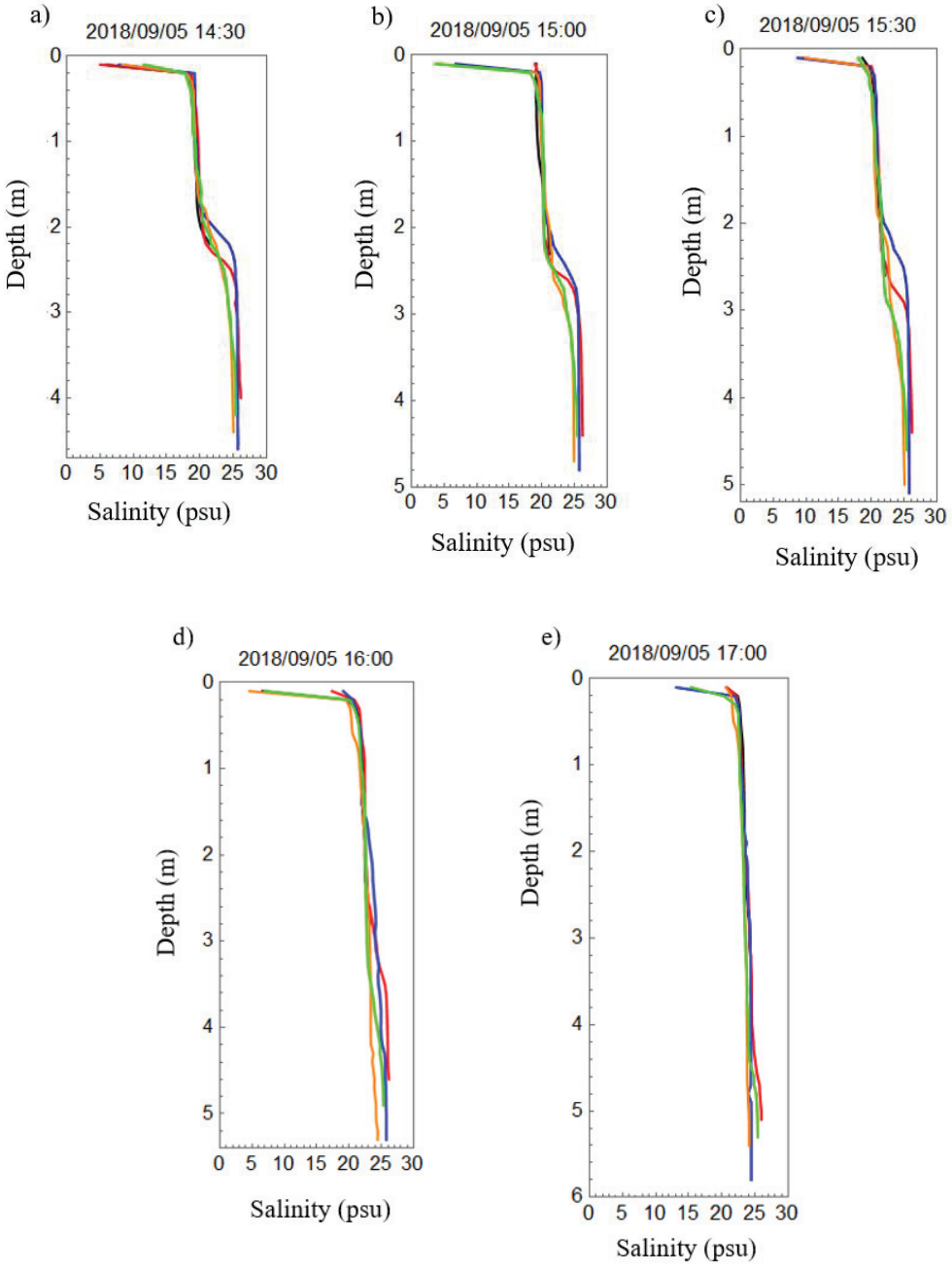

Figure 2.18 Vertical profiles of salinity at the cross-sectional (Shinkoi bridge) estimated by CTD, P_1 (black line), P_2 (red line), P_3 (blue line), P_4 (orange line), P_5 (green line)

However, there is a difference between salinity vertical structures recorded at upstream and downstream sections. At hours 14:30, 15:00 and 15:30, there are significant changing in vertical salinity profile at the middle part of the water column near to Shinkoi Bridge (see Figs. 2. 18a, 2.18b, and 2.18c) while at the same time the significant changing in vertical salinity profile recoded near to Asahi Bridge is found at the bottom of the water column (see Figs. 2.19b, 2.19c, and 2.19d).

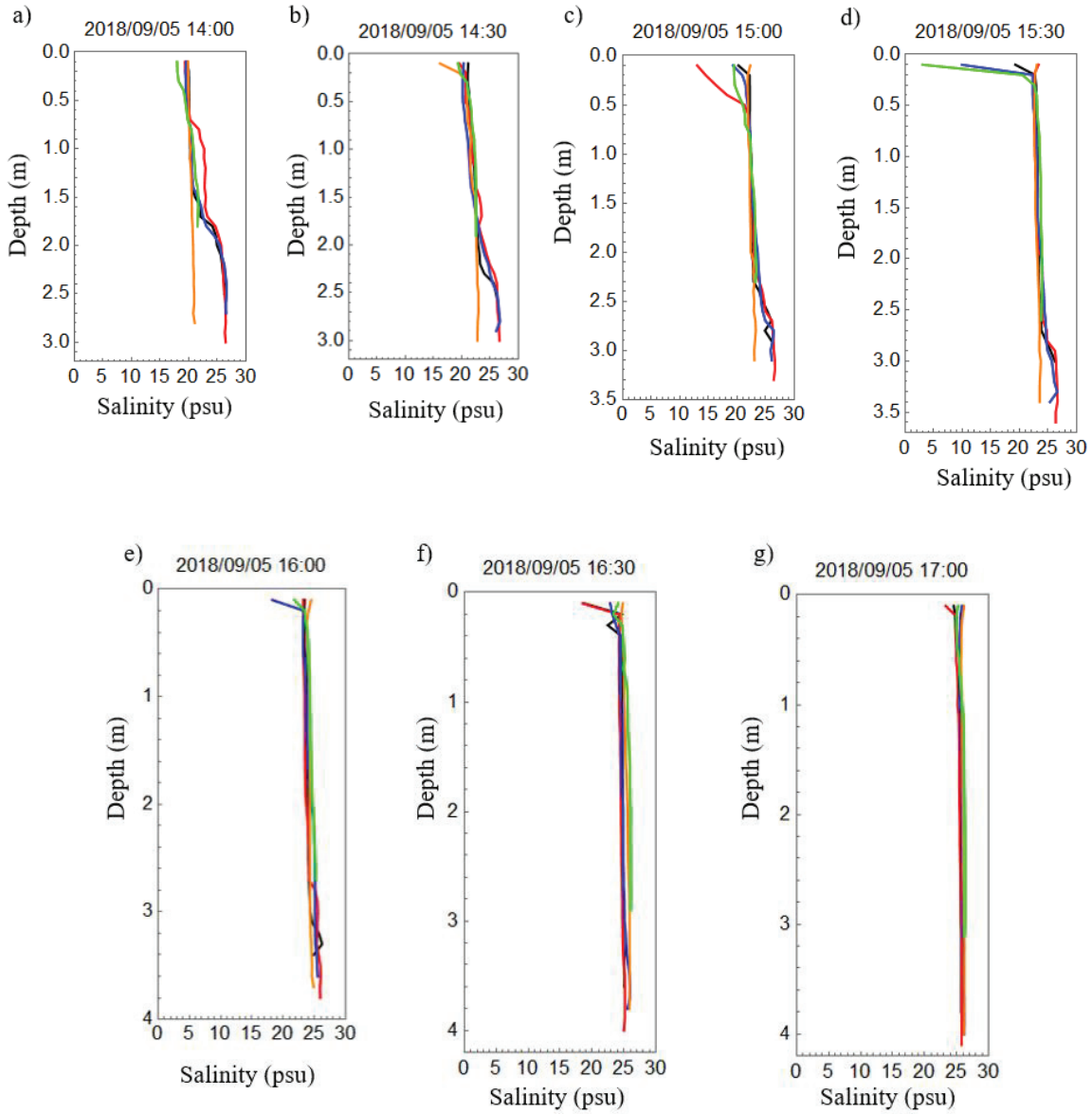

Figure 2.19 Vertical profiles of salinity at the cross-sectional (Ashahi Bridge) estimated by CTD, P_1 (black line), P_2 (red line), P_3 (blue line), P_4 (orange line), P_5 (green line)

The vertical salinity profiles measured using CTD of the mid flood during neap tide at the upriver and the downriver sections are shown in Figures 2.20 and 2.21, respectively. In general, during neap flood tide, salinity distributions in the cross sections at the downstream and upstream areas are similar, with stratification developed during the middle of the flood tide, and is weakened during the end of flood tide. There is a slight difference in de-stratification process close to the end of flood tide between the two locations, with the de-stratification sharper at the downstream (see Figs. 2.21e and 2.21f) than upstream area (see Figs. 2.20d and 2.20e).

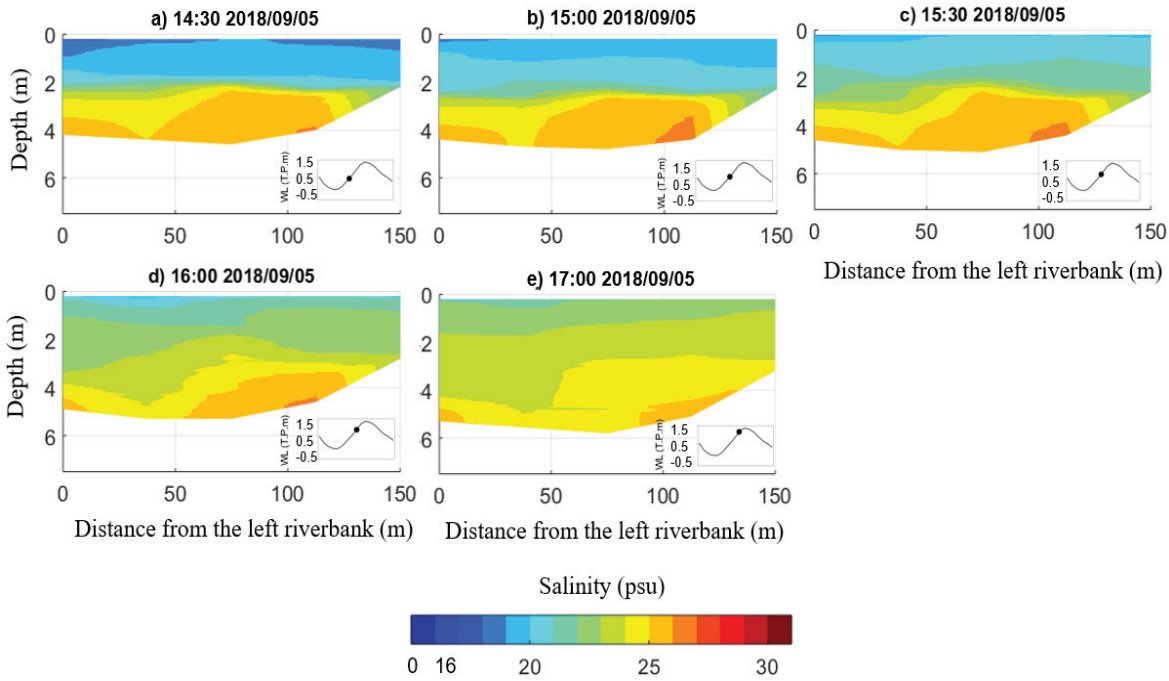

Figure 2.20 Salinity distributions in the cross section at the upstream area (Shinkoi Bridge) during neap tide

In general, the surface-to-bottom distribution of salinity at the locations along the estuary at different distances from the river mouth is expected to be different because of several factors such as the longitudinal salinity gradient and the bathymetry effect. However, it seems that the distance of 850 m between the two locations in this study is insufficient to reveal the expected difference. A study in vertical salinity distribution at locations along the Ōta River estuary with longer distance apart is needed in the future.

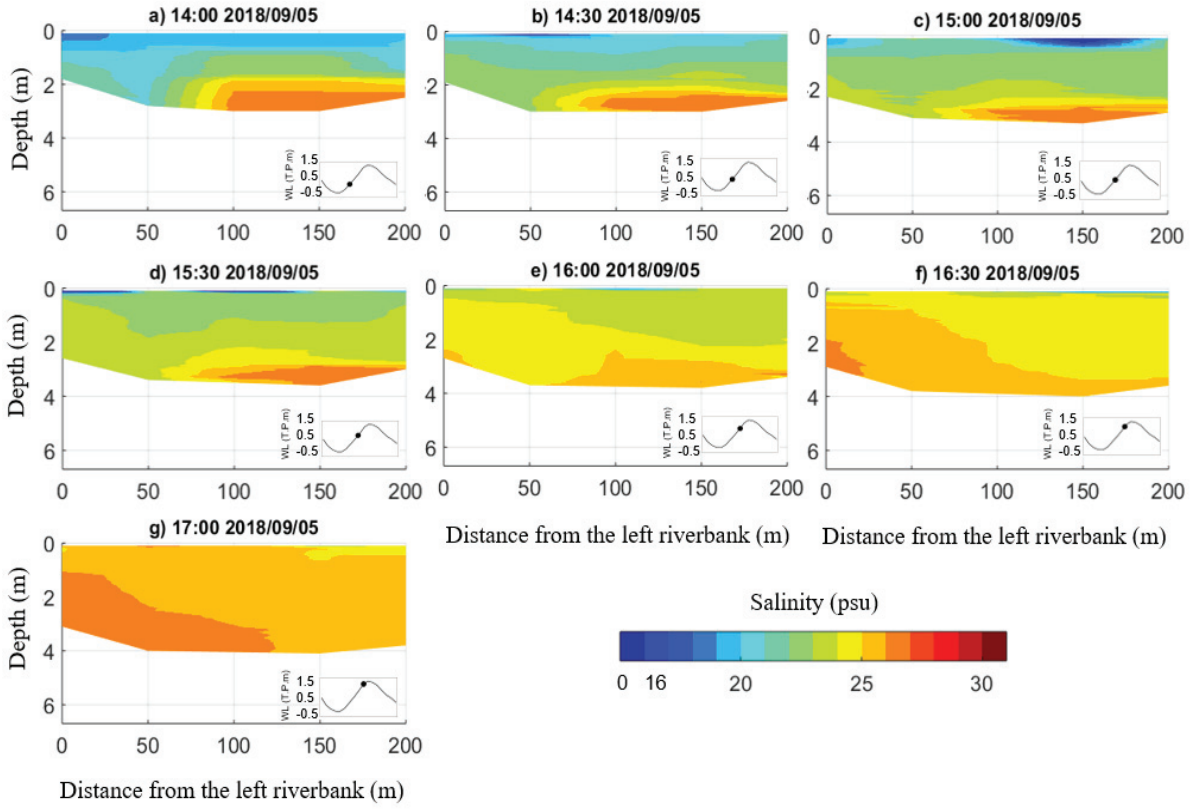

Figure 2.21 Salinity distributions in the cross section at the downstream area (Asahi Bridge) during neap tide

Also, the comparison between figures of surface-to-bottom salinity of mid flood during the two periods (December 5th 2018 and October 2nd 2020) presents a remarkable difference in stratification process between neap and spring conditions, with stratification increasing significantly more during the neap tide than during spring tide. During spring tide, salinities in cross section distribute mostly laterally (see Fig. 2.17), while during neap tide the surface-to-bottom salinity difference was 5 ÷ 8 psu (see Figs. 2.20 and 2.21), or 20% ÷ 32% (mean of 25 psu). At the middle of the neap flood tide (see Figs. 2.20a, 2.20b, 2.20c and Figs. 2.21 a, 2.21b, 2.21c, 2.21d), the number of significant stratification layers is seven over a water depth of 4 m, indicating a well stratified water column, then decreases and thus the significant stratification layer depths increases. On the neap tide, the tidal range of the estuary decreases and the currents are moving more slowly than at the spring tide. It is because the vertical mixing reduces and instantaneous mixing energy reaches the minimum value over a spring - neap tidal cycle that leads to stronger stratification during the neap tide periods than during the spring tide periods. Stratification between neap and spring conditions are significantly different, which suggests that the salinity dynamics of these two tidal periods are different.

2.5.2 Density distributions in the cross section

2.5.2.1 Tidally periodic density distributions

Tidally periodic stratification is explored as the mechanism of several phenomena in estuaries such as mixing, salinity intrusion (Stacey et al., 2008). The most common reason for the tidally periodic stratification of density is tidal straining (Simpson et al., 1990). Figures 2.22 and 2.23 show the vertical distribution of density recorded at the Shinkoi Bridge during the first and second peak of the water level, respectively. The results were estimated from the CTD data set recorded on October 2nd, 2020. It is can be seen that, the density distributions during spring tide at the observation site have clear tidally periodic characteristic.

In both slack periods, heavier density fluxes move from the left side to the right side of the river bank at the end of the flood tides. In the early of the ebb tides, when the lateral salinity intrusion process finished, resulting in vertical density distribution.

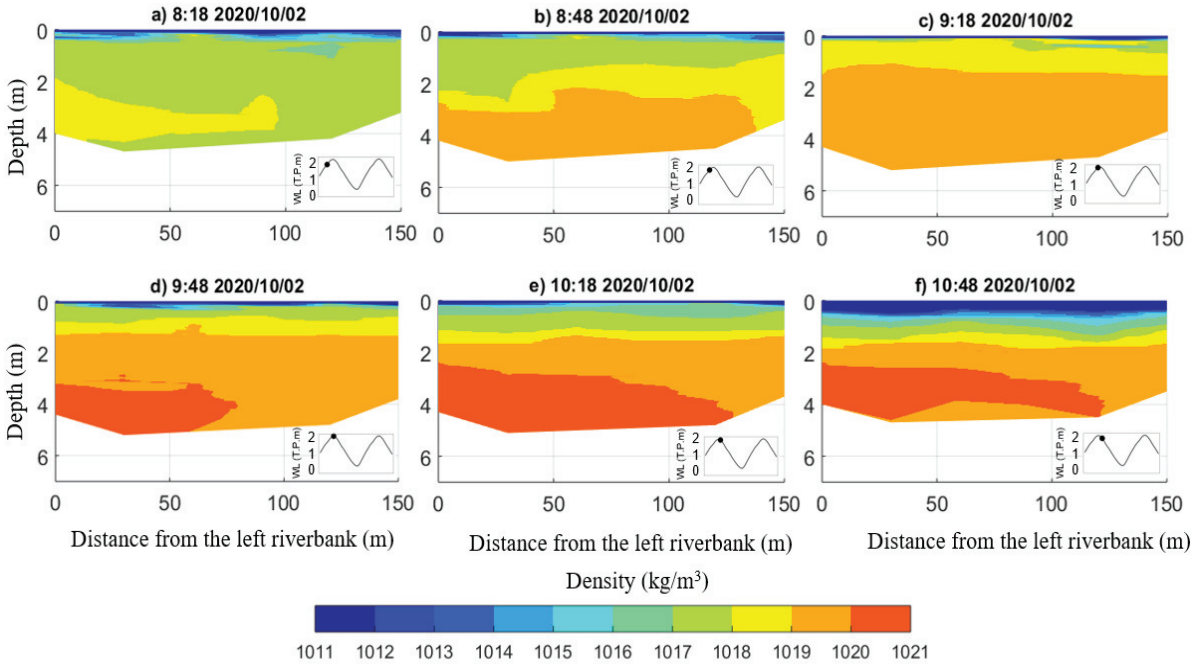

Figure 2.22 Density distributions in the cross section at the first high water slack during spring tide

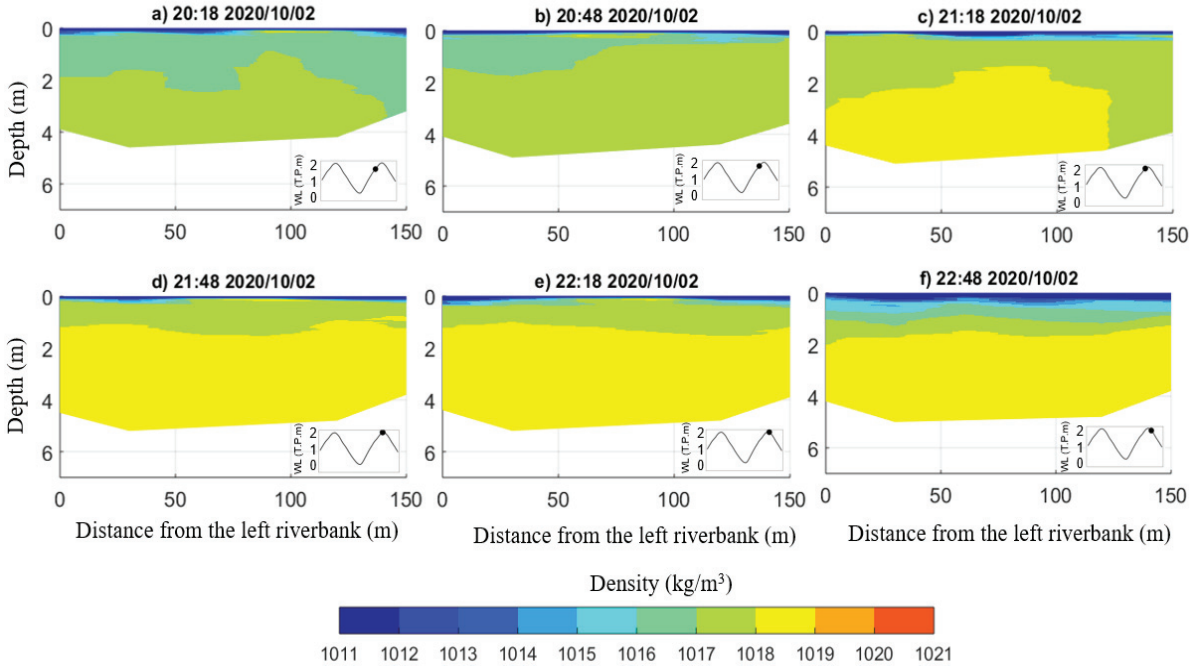

Figure 2.23 Density distributions in the cross section at the second high water slack during spring tide

2.5.2.2 Lateral density gradient distributions

Figure 2.17 shows a strong lateral salinity distribution during flood tide. To consider the relationship between the lateral distributions of salinity and density, the variation of the lateral density gradient during a flood tide is estimated and plotted in Figure 2.24. The lateral density gradient ($\partial\rho_y/\partial y$) indicates the density variation in cross section of channel. In this study, lateral density gradient is estimated from the data set collected in the second CTD campaign, (ρ_y) is the water density collected at the observation points (P_1−P_6) (see Fig. 2.8), and (y) is the cross-sectional distance.

During approximately three hours, from the early to the late of the flood tide, the value of the lateral density gradient changed significantly. However, the variation trend of lateral density gradient is stable. It is evident that in spite of the significant change of density, the lateral density gradient is likely to remain unchanged.

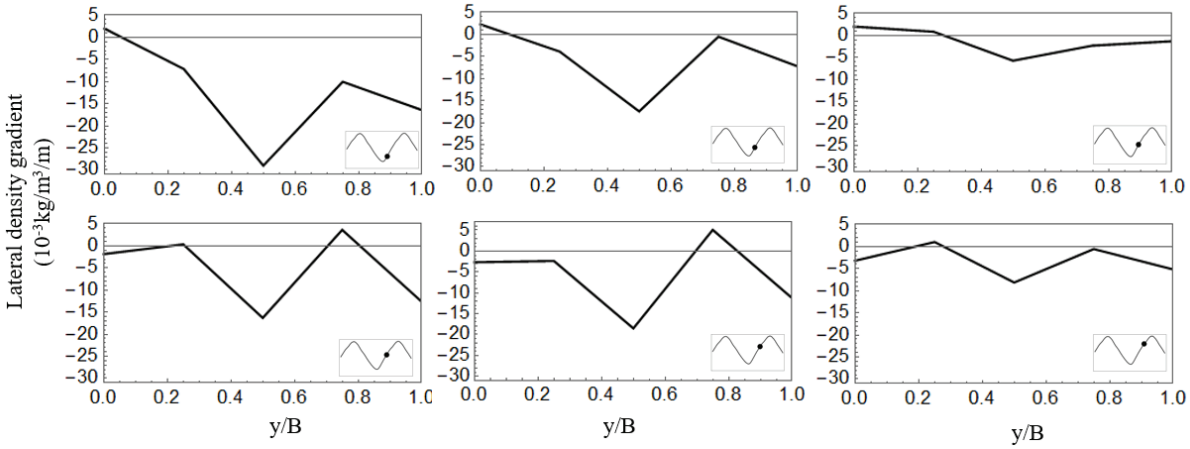

Figure 2.24 Lateral density gradient, averaged over a depth from 0 to 2.5m below the surface at Shinkoi Bridge during a typical flood tide (October 02, 2020), (y) is the lateral distance from the left river bank, (B) is the cross-section length of the channel at the observation site.

Normally, the turbulent mixing in the late of the flood tides decreases which maintains the lateral density gradient, and pushes the surface flows to the channel center and leading to lateral salinity distribution of the water column. For further clarification, Figures 2.25a−2.25e show the distributions of the lateral density gradient at flood tides. It can be seen that the surface flows are pushed into the center of the channel, resulting lateral flows (see Fig. 25f) and lateral salinity distribution as well (see Fig. 2.17). Figures 2.17a and 2.25b respectively present the distributions in the cross section of salinity and lateral density in the early of flood tide at Shinkoi Bridge. These figures show clearly the relationship between the lateral distributions of density gradient and salinity as addressed above, with the former is the leading cause of the later. Nunes & Simpson (1985) and Lacy et al. (2003) also described a similar phenomenon in their studies, and concluded that the relaxation of the lateral density gradients is a usual mechanism of lateral salinity distribution.

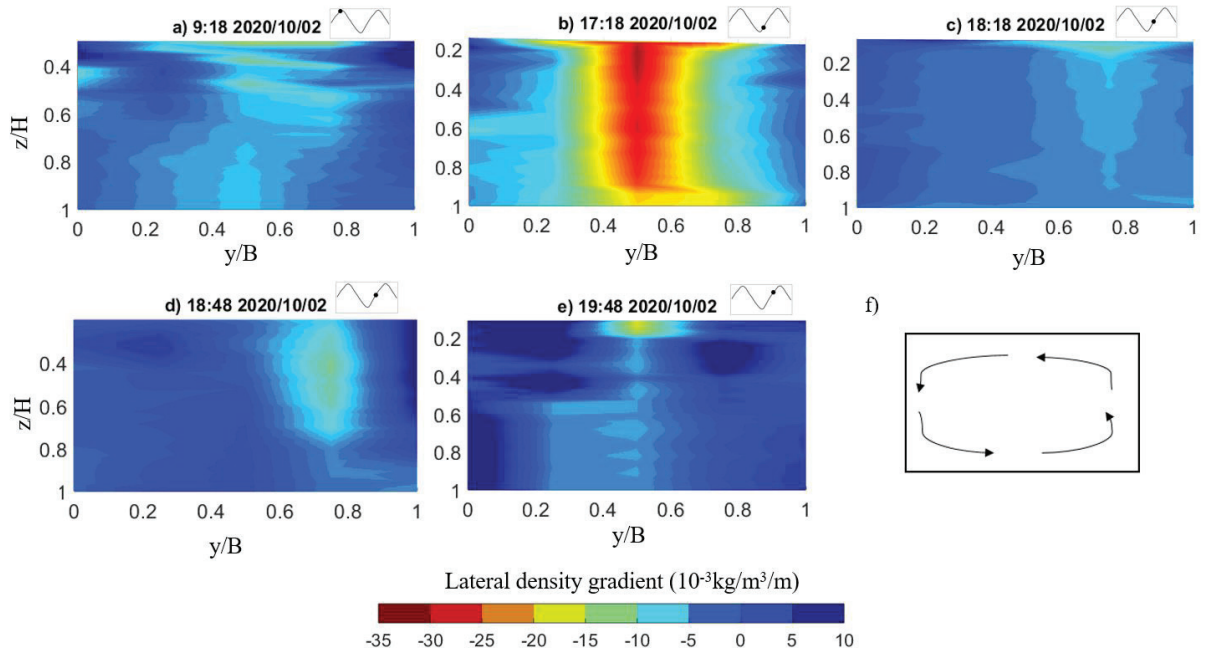

Figure 2.25 (a−e) Distributions of lateral density gradient during flood tides at Shinkoi Bridge, "*z*" is the vertical distance from the water surface, "*H*" is the water depth, "*y*" is the lateral distance from the left river bank, "*B*" is the cross-section length of the channel at the observation site, and f) Schematic of lateral circulation.

2.5.2.3 Vertical density gradient distributions

Figures 2.26 and 2.27 present the density distributions in the cross section during a typical neap flood tide at Shinkoi Bridge and Asahi Bridge, respectively. The results were estimated from the CTD data set recorded on September 5th, 2018 during a period of four hours. In general, the vertical density variation at both upstream area (Shinkoi Bridge) and downstream area (Asahi Bridge) have the similar range, from approximately 1012 kg/m^3 to 1016 kg/m^3.

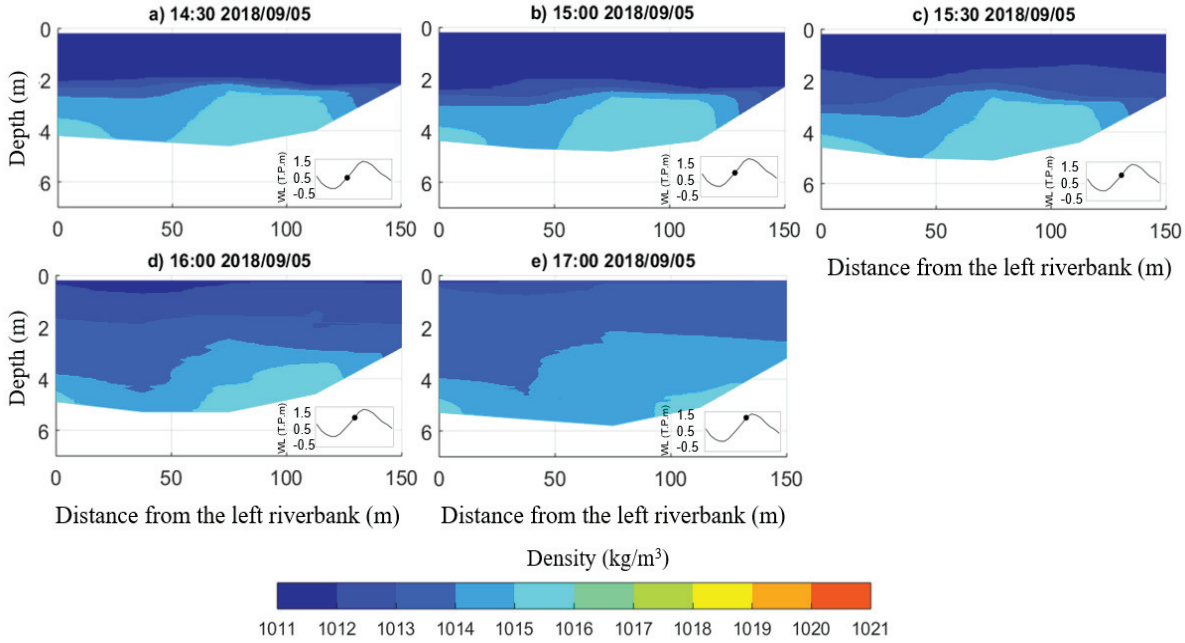

Figure 2.26 Density distributions in the cross section at upstream area during neap tide

In Figures 2.26a, 2.26b, 2.26c and Figures 2.27a, 2.27b, 2.27c, the degree of the vertical density fluctuations in the middle of the neap flood tide at the two sections are nearly similar, with the vertical density gradient increases in the mid-depth parts. However, close to the end of the flood tides, the vertical density fluctuation at the upstream section (see Fig. 2.26e) is stronger than the downstream section (see Fig. 2.27e) at the same phase. In detail, figure 2.26e shows that the vertical density ranges from 1012 kg/m^3 at the surface to 1016 kg/m^3 at the bottom of the water column while figure 2.27e shows the vertical density′s range of 1015 – 1016 kg/m^3.

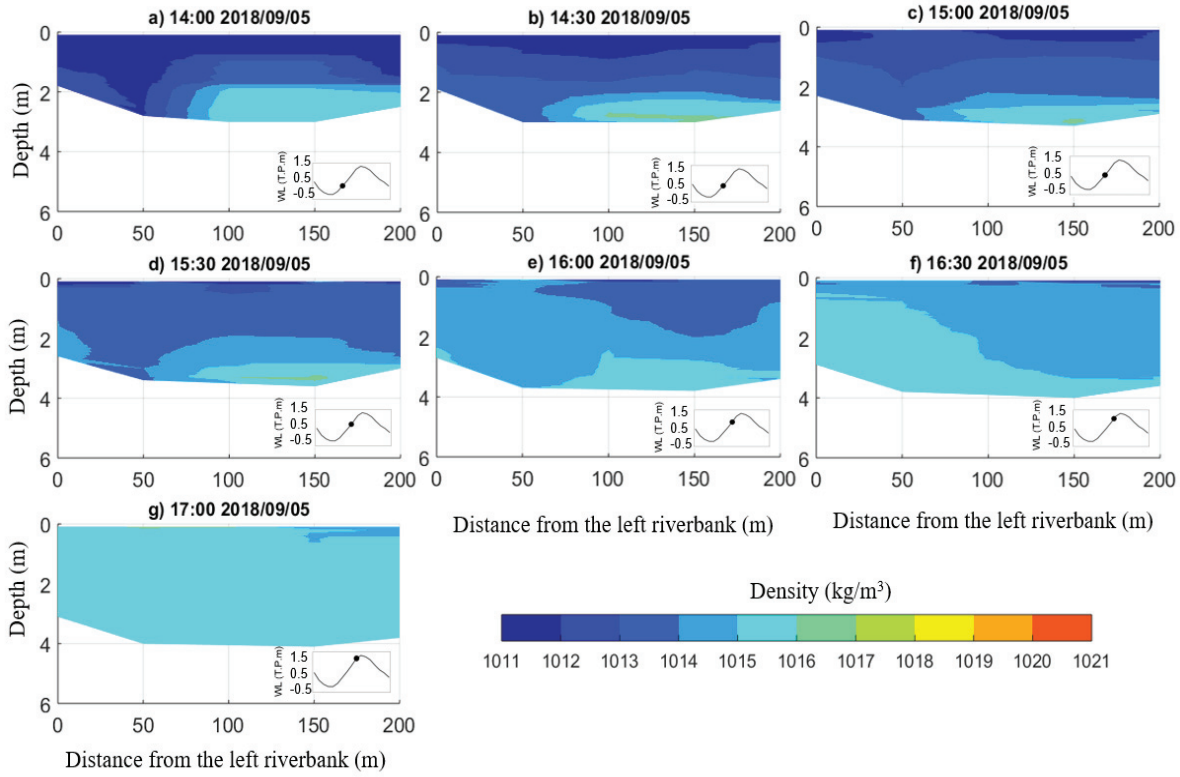

Figure 2.27 Density distributions in the cross section at Asahi Bridge during neap tide

Figures 2.28 and 2.29 present the vertical density gradient distributions during neap tide at Shinkoi Bridge and Asahi Bridge respectively. General, there is a significant difference between the vertical density variations in the downstream and upstream areas over the river segment length of 850m, which located around 4.5km from the mouth. At the upstream area (Shinkoi Bridge), during the middle of flood tide, vertical density gradient is strong in the middle of the water column at almost positions from the left to the right sides of the riverbank (see Figs 2.28 a, 2.28b, 2.28c), then becomes very weak at the late of flood tide (see Figs. 2.28d, 2.28e). However, at the downstream area (Asahi Bridge), vertical density gradient develops from the middle to the bottom of the water column at the early of flood tide (see Figs. 2.29a, 2.29b, 2.29c), then becomes weak at the end of flood (see Figs. 2.29d, 2.29e). The onset of the phenomenon that shows vertical density gradient is stronger at the middle of the water column than that at the surface and the bottom parts can be controlled by the vertical straining due to the surface-to-bottom difference of transverse velocity. A previous study (Soltaniasl et al., 2013) showed that the surface-to-bottom difference of transverse velocity in the Ōta diversion channel is significantly which creates a oscillatory flow between the surface to the bottom of

the water column. This flow may create a straining of the density field in the middle part of the water column, and enhancing stratification.

Similarly, vertical salinity distributions of this period has the same pattern compare to the variation of vertical density gradient. At the upstream area (Shinkoi Bridge), a strong stratification is found in the middle of the water column during the middle of neap-flood tide (see Fig. 2.20). At the downstream area (Asahi Bridge), the stratification strongly develops in the surface and middle of the water column, then becomes weaker; and the salinity distributions in the cross section at this area is lateral distribution at the late of the flood tide (see Figs. 2.21). Thus, the vertical density gradient distributions in the Ōta diversion channel might be an important factor that controlled the stratification during flood tide.

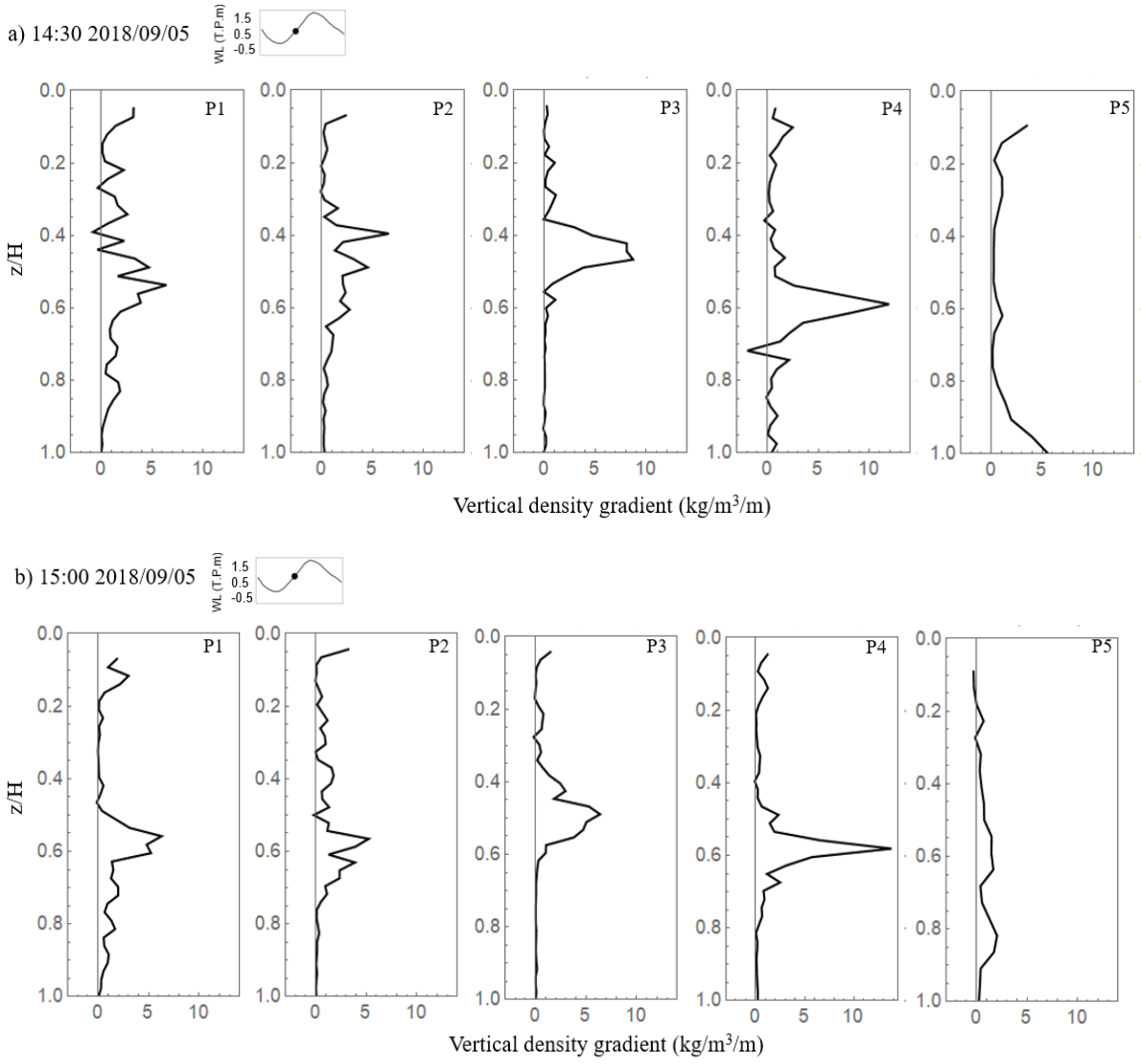

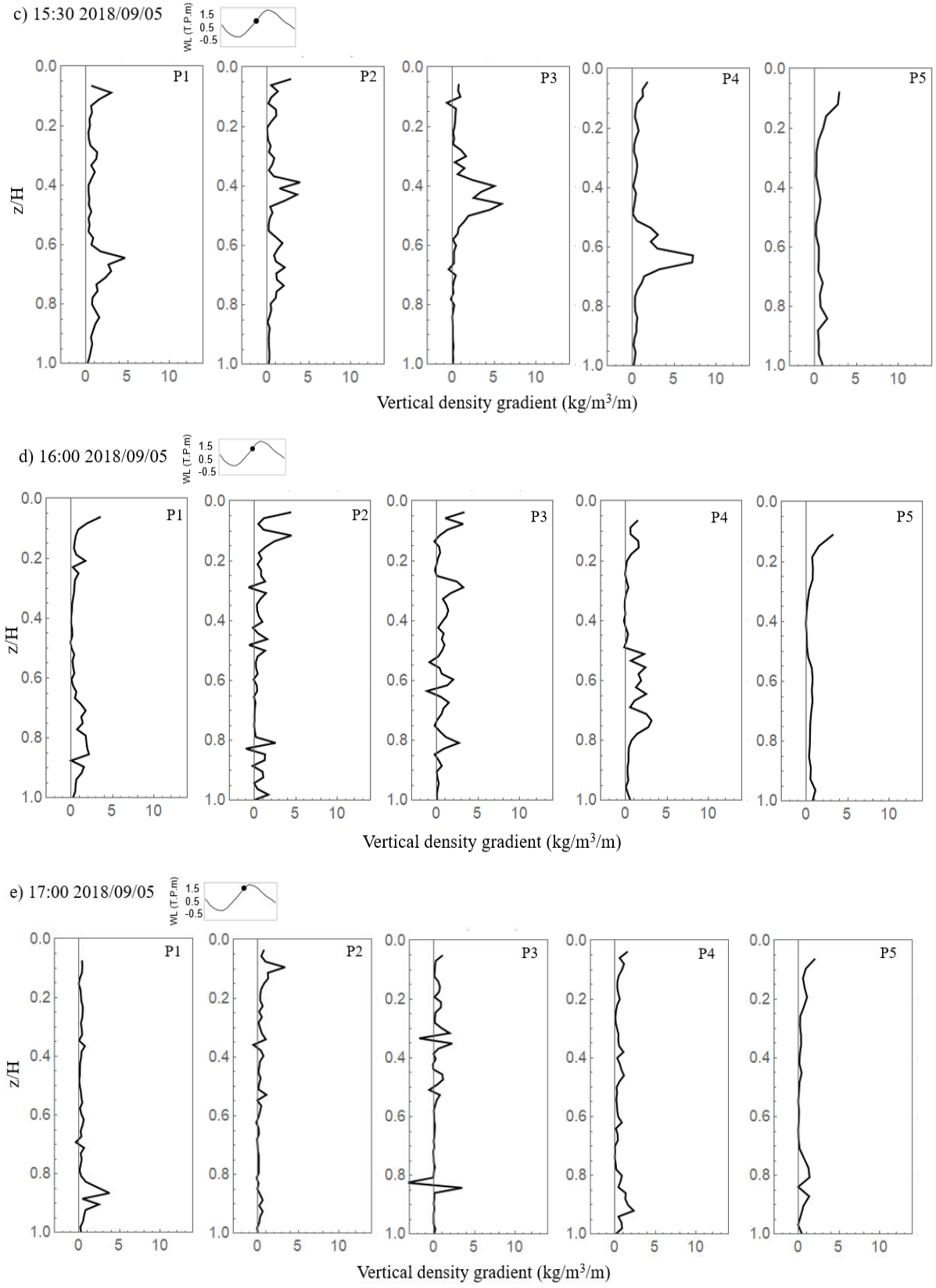

Figure 2.28 Vertical density gradient distributions at Shinkoi Bridge during neap tide

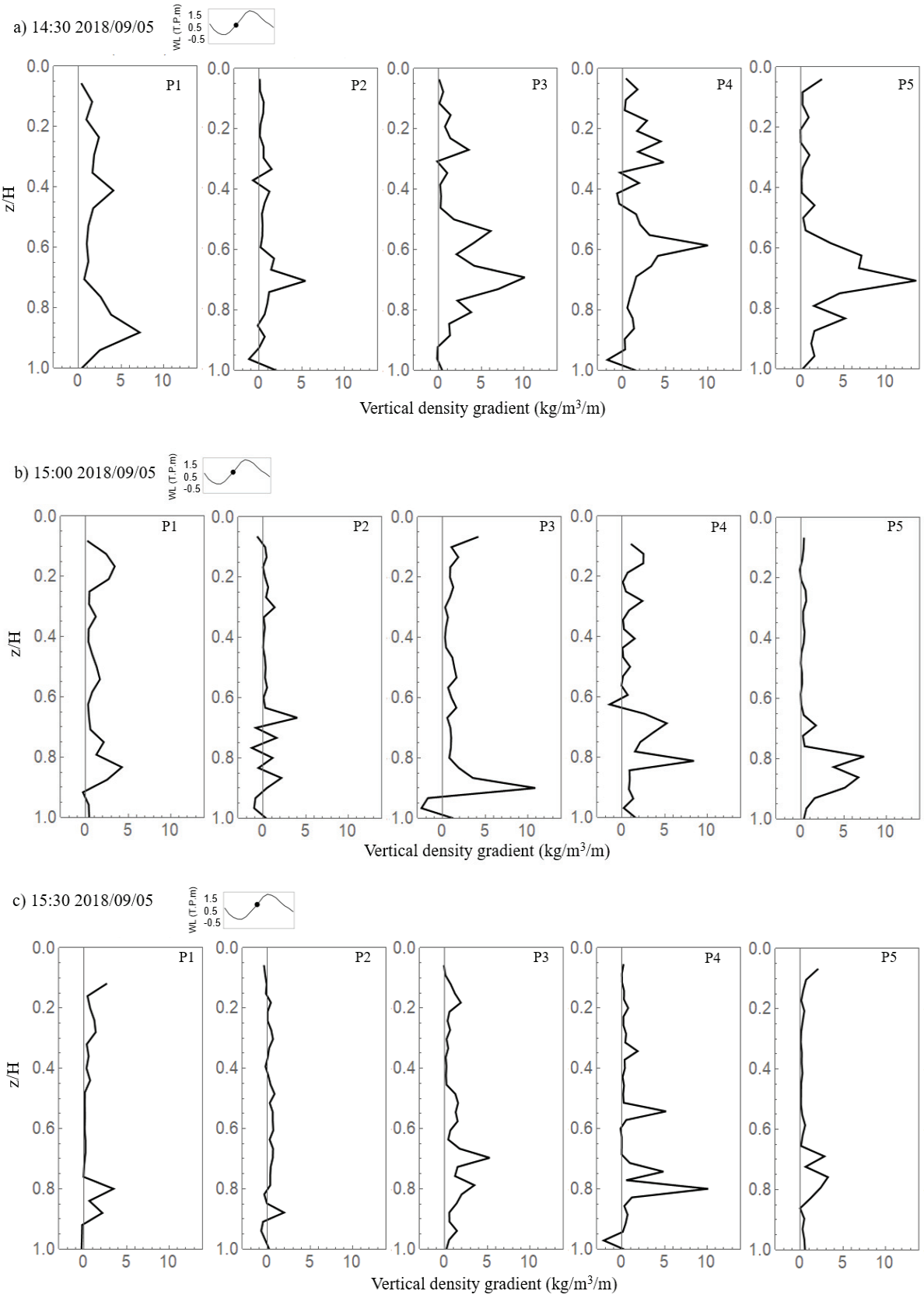
a) 14:30 2018/09/05
WL (T.P.m)
1.5
0.5
-0.5
P1
P2
P3
P4
P5
z/H
0.0
0.2
0.4
0.6
0.8
1.0
0
5
10
Vertical density gradient (kg/m3/m)
b) 15:00 2018/09/05
c) 15:30 2018/09/05

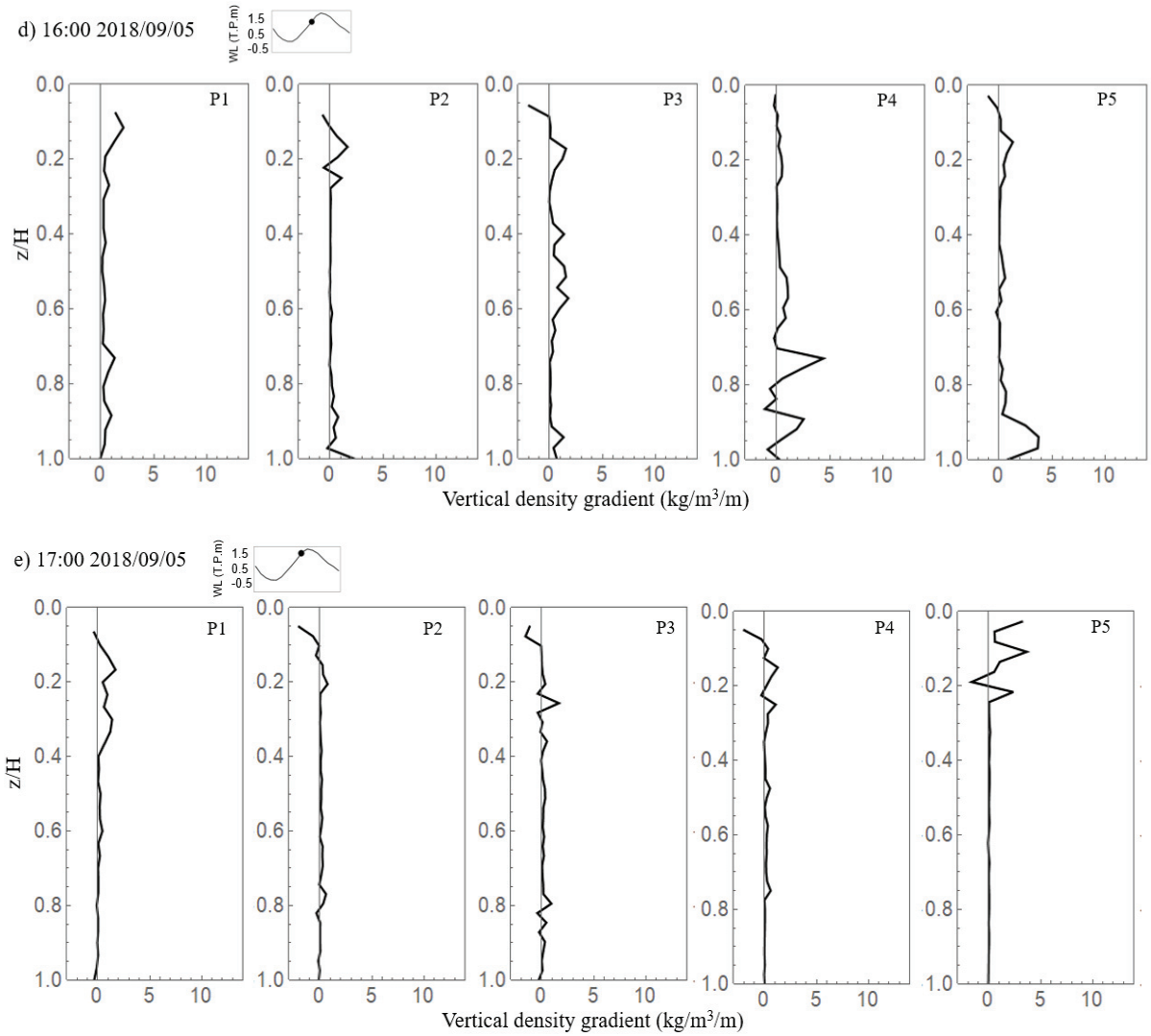

Figure 2.29 Vertical density gradient distributions at Asahi Bridge during neap tide

2.6 Discussion

The following parts will discuss the contribution of the factors and mechanisms that may control the stratification process in the Ōta diversion channel.

2.6.1 The effect of freshwater discharge on stratification

Although the water depths at the two peaks of tide are similar (see Fig. 2.10b), the salinity peak during the first tide is approximately 2 psu higher than during the second tide (see Figs. 2.15c and 2.16c). The lateral salinity gradient in the first tide is also higher than that in the second tide. Besides, the number of significant stratification layers during the first tide ranged from 5–15 (see Fig. 2.11) is higher than that during the second tide of 3–10 (see Fig. 2.12). This is because, during the second tide, freshwater inflow recorded at Yaguchi Gauging Station

almost doubled during the first tide, from approximately 40 m^3/s to approximately 70 m^3/s (see Fig. 2.10). Comparing the vertical salinity profile between the two stages of the end of flood, the significant influence of the freshwater flow on stratification process is evident. Thus, the salinity dynamic process in the Ōta River estuary is affected significantly by freshwater input upstream.

Furthermore, a re-stratification process occurred during late in the flood tide. During this period, tidal currents decelerated leading to a rapid diminishment of turbulent mixing. The force deduced from the lateral density gradients (see Fig. 2.25) tends to become stronger and overtake the turbulent mixing, enhancing the vertical stratification. The reason for this phenomenon has been discussed in previous studies with the term "lateral straining" (Scully & Geyer, 2012, Geyer & MacCready, 2014). Thus, the stratification development during flood tides in the Ōta River estuary might be due to of the lateral density.

2.6.2 The effect of bathymetry on salinity stratification

Another reason for the lateral salinity gradient is the effect of significant variation of the bathymetry at the study site. Valle (1997) conducted an observation in one of the largest estuaries in the United States to describe the influence of the bathymetry on the transverse hydrographic structure. Their study stated that the geostrophy of the river bed is one of the main factors that influence to the dynamics in the transverse direction.

The bathymetry of the Ōta diversion channel is complicated and represented by shoals and flood flows (Gotoh et al., 2013). The Ōta diversion channel is the main entrance channel of the Ōta River system where the transportation happens regularly. As shown in Figure 2.4, the left riverbank side is deeper than the right riverbank side on the middle of the channel segment, and the right side is deeper than the left side at the areas close to the two bridges, resulting in an irregular bathymetry in the observation site. During the flood tide, at the bottom of water column, the water that is saltier and low-moving tends to move toward the deeper area of the channel while at the surface, river flow tends toward straight. This lateral shear creates a remarkable lateral salinity gradient during the early and middle flood. Previous studies (Ralston et al., 2010, Fischer, 1972) have reported similar findings and stated that the transverse shear generates a lateral salinity gradient.

Also, the comparison of the transverse salinity distribution between this stage and other stages, including the end of ebb and the end of second flood stages, shows that the stratification and de-stratification respond quickly to tidal changing. In Figure 2.14f, the salinity distribution

in the cross section showed a high stratification with the stratification layer depths equal at the end of ebb tide, then changes quickly to the lateral salinity distribution after 30 minutes at the early stage of flood tide (see Fig. 2.17a). Similarly, the re-stratification happens at the end of flood tide, close to the high water level (see Fig. 2.16a) after the previous lateral distribution stage (see Fig. 2.17f). To evaluate fully this rapid change, a consideration of the spatial and temporal variabilities is necessary in future research. In this case, the reason of quick changing in salinity distributions at the end of ebb and flood tides might be attributed to the shallow depth of the estuary.

2.6.3 The effect of the water temperature

Generally, the density stratification of a water column is controlled by water temperature and/or salinity because the water density is a function of the water temperature and salinity (Millero & Poisson, 1981). Table 2.3 shows the typical computed values of sea water density depending on the variations of temperature and salinity. When salinity ranges from 20−35, and temperature ranges from 15−30°C, density changes approximately 0.026% for temperature difference of 1.0°C. However, the density change by the 1-psu change of salinity is around 0.075%, shows triple the amount of density change as temperature difference. The surface-to-bottom temperature differences at the study site are not significant in both CTD campaigns, under 1.5°C (see Figs. 2.30 and 2.31). This might suggest that salinity dominated the density change in Ōta diversion channel, and the effect of temperature variation in vertical direction on salinity dynamics is not significant compare to other factors that mentioned above.

Table 2.3 The sea water density variations based on the variations of temperature and salinity (Millero & Poisson, 1981)

Salinity (psu) Temperature (°C)	0	10	20	35	40
0	999.843	1007.950	1016.010	1028.110	1032.150
15	999.102	1006.780	1014.440	1025.970	1029.830
30	999.651	1003.100	1010.530	1021.730	1025.480
40	992.220	999.575	1006.910	1017.970	1021.680

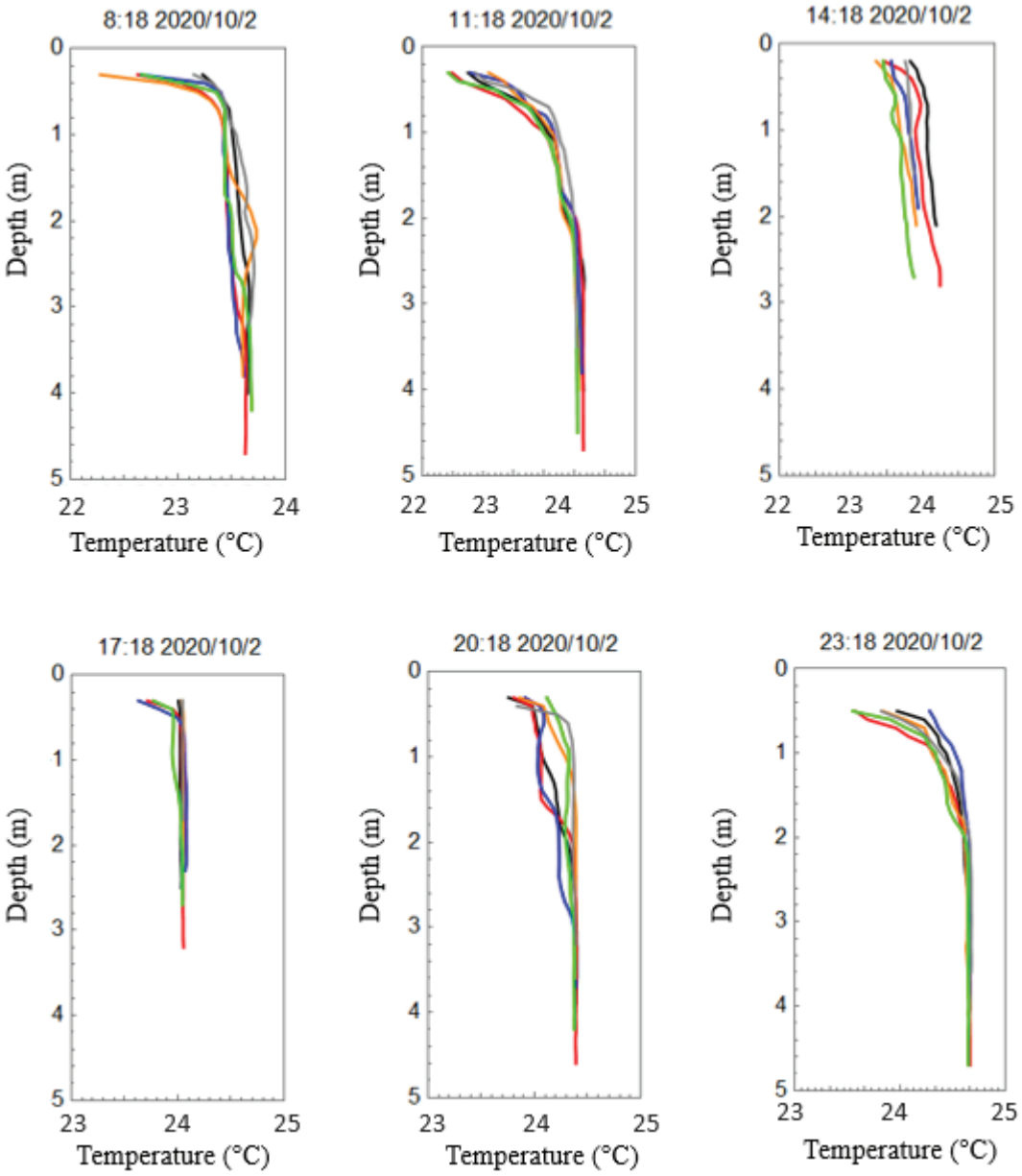

Figure 2.30 Vertical profiles of temperature at the cross section estimated by CTD of the second campaign at Shinkoi Bridge, P_1 (black line), P_2 (red line), P_3 (blue line), P_4 (orange line), P_5 (green line) and P_6 (gray).

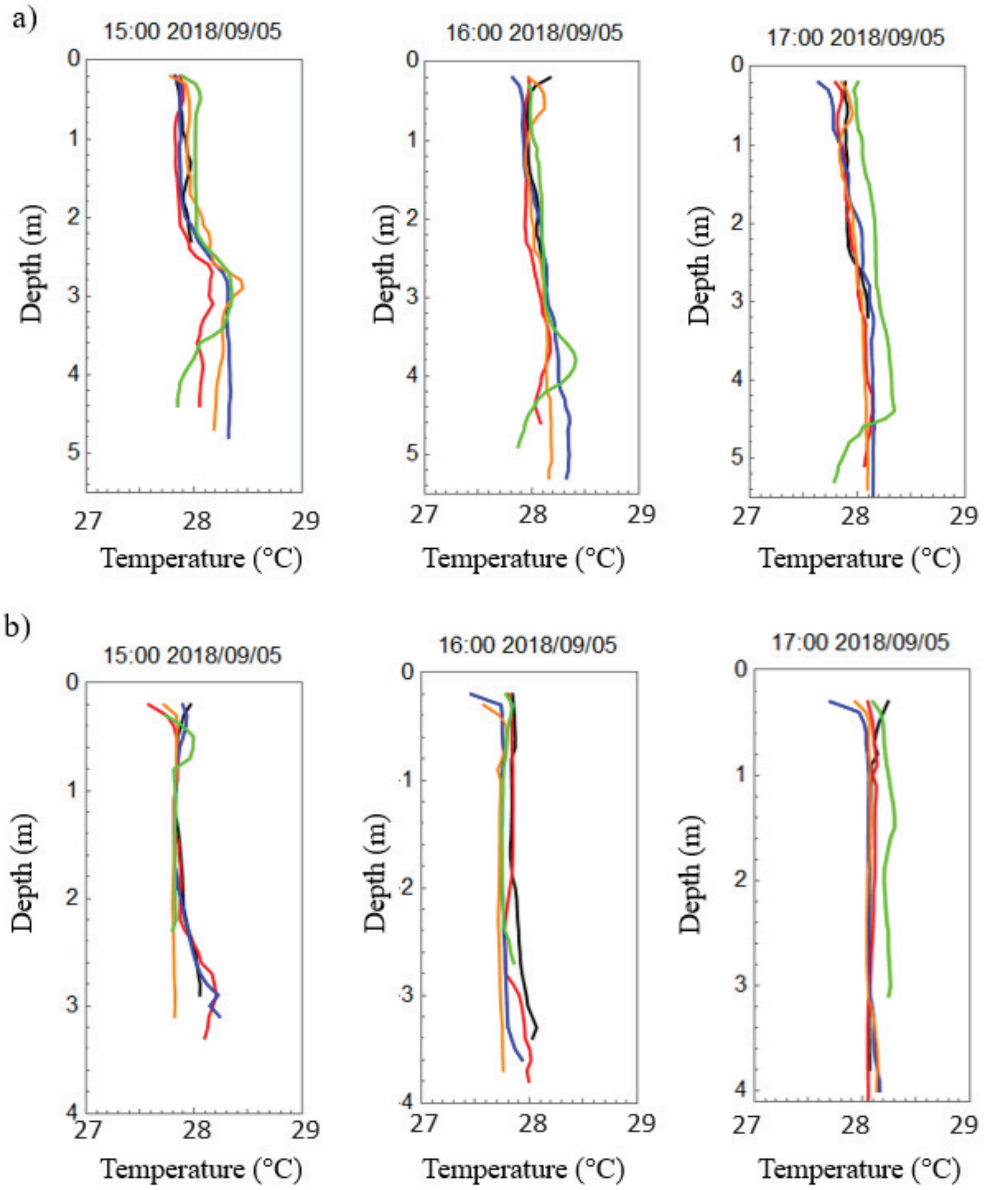

Figure 2.31 Vertical profiles of temperature at the cross section estimated by CTD of the first campaign at a) Shinkoi Bridge, and b) Asahi Bridge. P_1 (black line), P_2 (red line), P_3 (blue line), P_4 (orange line), P_5 (green line).

2.6.4 The time delays of the salinity

Delays in time of salinity maximum are found during slack water periods, with the range is from approximately 30 minutes to 1 hour. Figures 2.11a and 2.11b show qualitatively that the first high water slack occurred at approximately 9:48 while salinities reached its maximum value approximately 30 minutes after that. Similarly, during the end ebb stage, the low water

slack happened between 15:48 and 16:18 (see Figs. 2.14d and 2.14e), while the lowest salinity (salinity at all layers < 25 psu) occurred around 16:48 (see Fig. 2.14f). Similarly, the second high water slack occurred at about 21:48 (see Fig. 2.12a). It can be seen that the depth of the last layer (between 28 psu and 29 psu) is highest at hour 22:18 (see Fig. 2.12b), that means the maximum of the depth average salinity during this stage happened 30 minutes later, around 22:18.

For further clarifications, the FATS data set that collected from the second campaign (see Fig. 2.8) will be analyzed to add more information about time delays of salinity peaks. The correlation between cross-sectional average salinity estimated by FATS and the water level is showed in Figure 2.32 and Table 2.4 as follow.

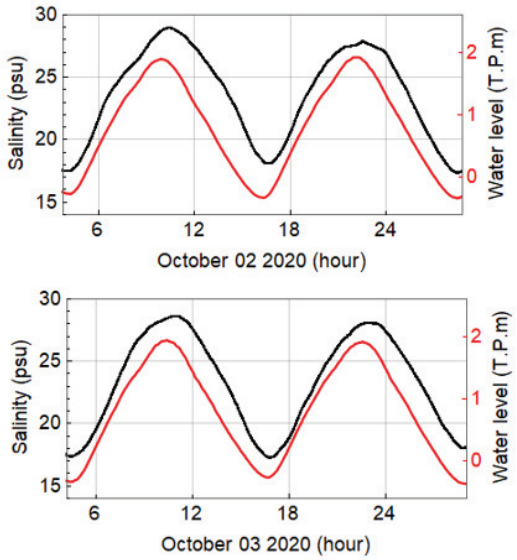

Figure 2.32 The comparison between the cross-sectional average salinity acquired using FATS (black lines) and water level (red lines) at the study site

Figure 2.32 shows a good correlation between cross-sectional average salinity and water level and delays in the time of the salinity maximum to the peak water level are presented in detail in the Table 2.4.

The time delay between salinity maximum and the peak water level are determined using the cross-correlation method (see Chapter 2, Section 2.4.4). In this study, cross-correlation is used to measure the time lags between cross-sectional average salinity deduced from FATS and water level. Calculating the cross-correlation for salinity and water level will return the maximum of the cross-correlation function that points clearly to the time when these two time series are best matched, indicating the time delay between them.

Figure 2.33 shows a typical of cross-correlation function between cross-sectional average salinity deduced from FATS and the water level. The cross-correlation function is maximum at the time 61 minutes, meaning the time delay between them is 61 minutes.

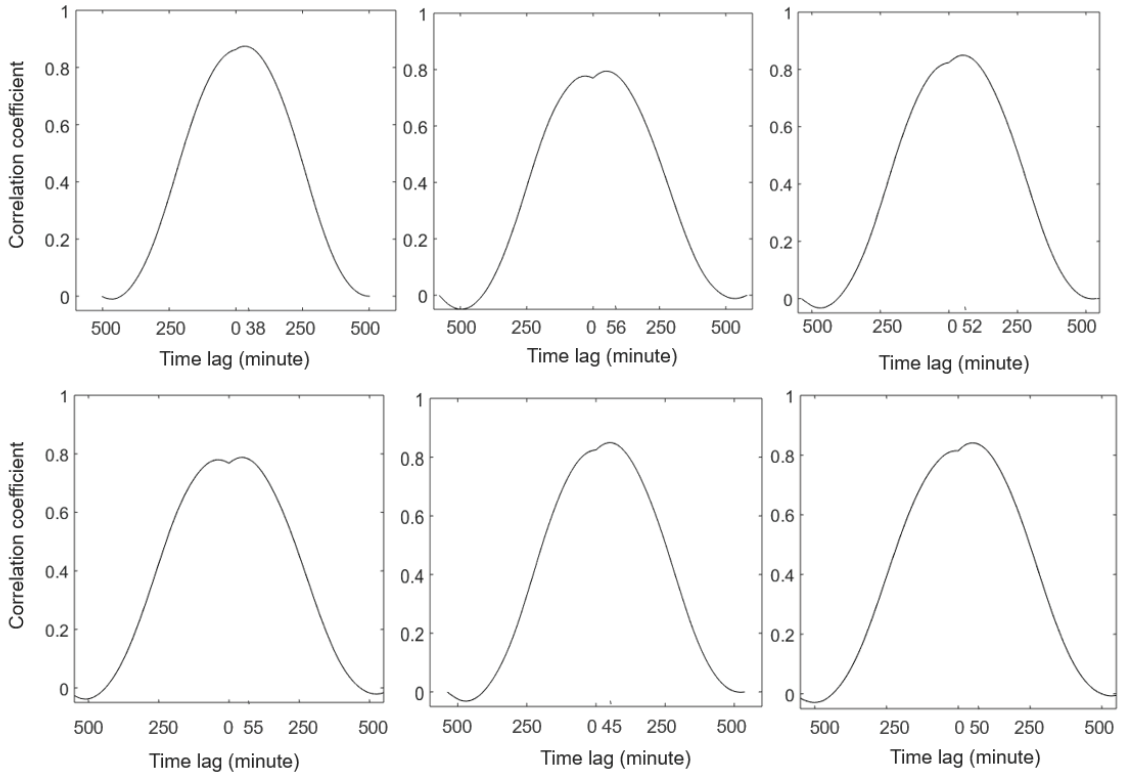

Figure 2.33 Cross-correlation of salinity versus the water level in Ōta diversion channel during the study period

Delays from 38 minutes to 56 minutes are seen for the six salinity peaks. With the tidal period of the Ōta River is approximately 12.48 hours, the phase shifts are generally of the order 18.27°–26.92°.

Table 2.4 The time delays of the salinity peaks

Peak number	Time lag (minute)	Phase lag (°)
1	38	18.27
2	56	26.92
3	52	25.00
4	55	26.44

5	45	21.63
6	50	24.04

Dyer (1973) stated that the density current effects, changes in water depth likely cause these delays in time of the salinity peak. In Ōta River estuary, another reason for that phenomenon is the effects of the freshwater flows from the Yaguchi Gauging station located upstream (Nguyen & Kawanisi, 2021, Kawanisi et al., 2011). Figure 2.34 also shows the relationship between the freshwater discharge recorded at Yaguhi Gauging Station and the delays in time of salinity peaks. It can be seen that the time lags raise corresponding with the decrease of the freshwater discharge. It is evident that the freshwater discharge from upstream affects significantly these time lags. Section 3.6.6 (Chapter 3) addresses in detail this phenomenon.

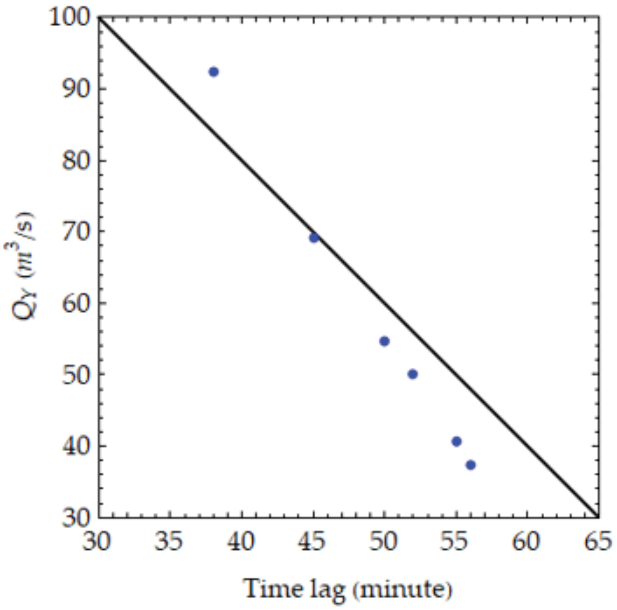

Figure 2.34 The association between freshwater discharge recorded at Yaguchi Gauging Station and delays in time of salinity

2.6.5 The effect of the tidal straining and tidal time scale

The field observations of the present research are conducted to collect the data of salinity and density without velocity data. However, some previous studies addressed the contribution of vertical and lateral variations in velocity to the stratification process. Besides, the characteristics for velocity in the Ōta diversion channel also are addressed by some previous

studies. Thus, this section discusses the role of tidal current in the stratification process in the Ōta diversion channel by citing the previous results.

2.6.5.1 The effect of the tidal straining

Tidal straining is the phenomenon that describes the straining effect induced by the vertical shear of swing tidal currents that act on horizontal density gradients. Another definition of tidal straining was presented by (Simpson et al., 1990), the interaction of the longitudinal density gradient in estuaries with the vertical shear in the tidal current leads to a forcing mechanism termed ‘‘tidal straining’’. There are two main types of tidal straining, horizontal tidal straining and vertical tidal straining. Horizontal tidal straining is lateral mixing between water masses which are advected at different speeds, due to lateral gradients in the longitudinal velocity. Vertical tidal straining is vertical mixing between water masses advected at different speeds due to vertical gradients in the longitudinal velocity.

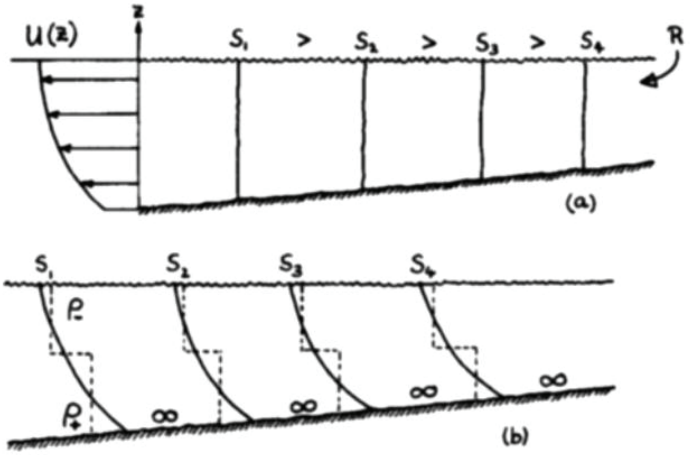

Figure 2.35 Schematic of tidal straining: (a) isolines vertical at start of ebb (b) stratification induced by shear on the ebb modified by top and bottom mixing (*Simpson et al., 1990*).

Figure 2.35 shows the mechanism of tidal straining process. The stratification is created by shearing of the faster and lighter layer of the water column over the saltier and slower-moving water of the next lower layer.

During ebb tides, the surface water that caries freshwater from upstream is often lighter and will move faster toward the river mouth and overtake the lower layers that are saltier and heavier. This process will continue to happen between two layers that are close, resulting in a stable structure and suppressing turbulent mixing. During the flood phase of the tide, this process will be reversed, thus, the stratification will reduce due to the effect of vertical shear.

In a previous research that carried out at Ōta diversion channel, Soltaniasl et al. (2013) showed that during ebb tide the velocity range of the lighter surface water (salinity variation of 2 – 8 psu) is +0.1 – +0.3 m/s ("+" denotes downward direction) while the saltier water (salinity variation of 14 –16 psu) locate on the river bottom and have velocity variation of −0.05 – −0.1 m/s ("−" denotes upward direction) (see Figs. 2.36 and 2.37).

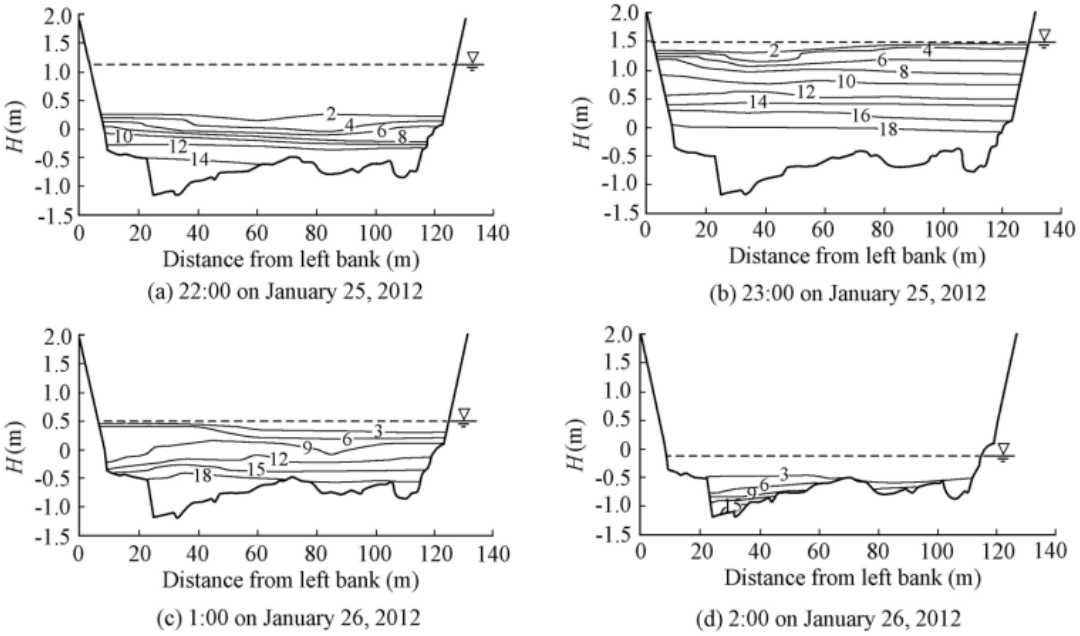

Figure 2.36 Contour plots of salinity at cross-sectional in the Ōta diversion channel estimated using CTD during a typical ebb tide (*Soltaniasl et al., 2013*)

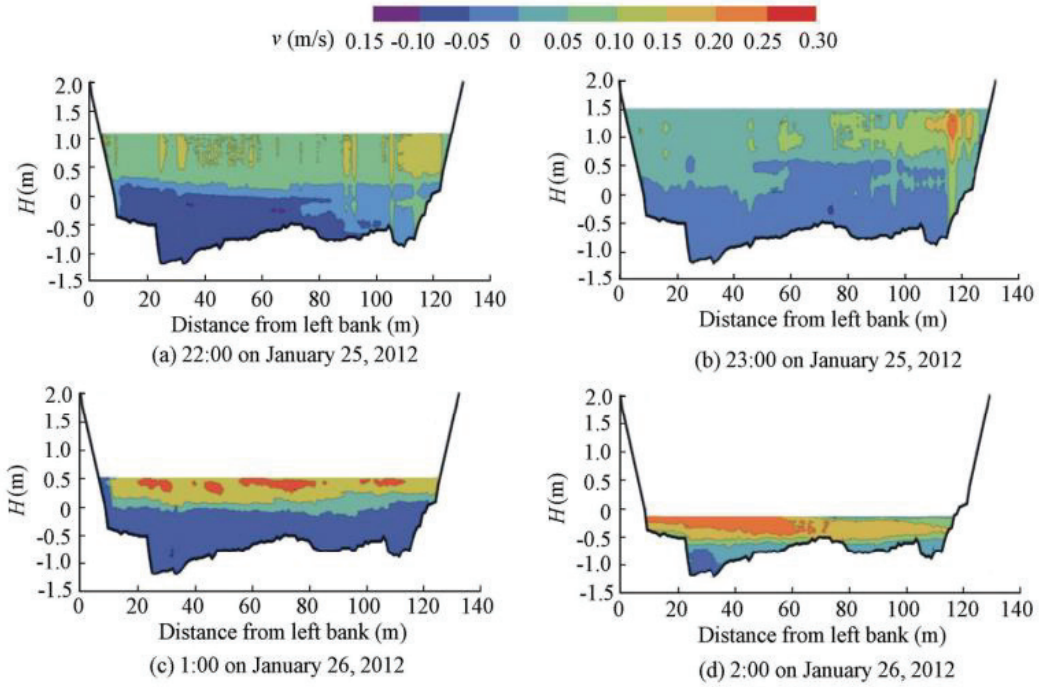

Figure 2.37 Contour plots of longitudinal velocity at cross-sectional in the Ōta diversion channel estimated using ADCP during a typical ebb tide (*Soltaniasl et al., 2013*)

2.6.5.2 Contribution from the tidal time scale

Nguyen (2021) and Razaz (2013) showed that the Ōta diversion channel is an ebb-dominant estuary, with an asymmetry in ebb-tide and flood-tide velocities: the highest velocities occurring during the ebb tide. Some previous studies have been conducted on the influence of the tidal time scale on the variation of stratification. Jay (1990) stated that the tidal asymmetry during a spring - neap tidal cycle plays an important role in stratification variability. Simpson (1990) also addressed that this asymmetry creates a vertical shear, and thus a straining; this phenomenon was described as tidal straining. During ebb tides, the surface current will accelerate and strain the horizontal salinity gradient, which might increase the stratification. Furthermore, the combination of strong advection and straining during ebb tides may also enhance the stratification process.

2.7 Conclusions

This chapter presents the variations of salinity and density in the vertical and lateral directions in the Ōta diversion channel. To clarify a transverse dynamic process throughout an investigation of salinity and density distribution in the cross sections, a field observation in the Ota diversion channel was conducted. The main novelty of the present research is using the

number of stratification layers and their depth, as well as the surface-to-bottom salinity difference to evaluate the stratification/de-stratification degree in a tidal shallow and narrow estuary.

At the middle part of the Ōta diversion channel (approximately 4.5 km from the river mouth), the distributions of salinity, density, and water temperature were measured over a tidal cycle at both spring and neap tides, using Compact Conductivity-Temperature-Depth sensor as a main instrument with other instruments, including FATs, CT sensors, remote controlled boat. Two CTD campaigns to collect salinity data sets were carried out across the river at two bridges (Shinkoi and Asahi bridges), with a longitudinal distance of approximately 850 m between the two bridges.

The vertical profiles of salinity, density, and temperature are analyzed over the two periods of time, the first one is on September 5th 2018 referring a neap tide, and the second one is on October 2nd 2020 referring a spring tide.

The results of salinity distributions in the cross sections indicate that the density driven might be the mechanism of the stratification process in the Ōta diversion channel.

In detail, salt wedges moved from the left side to the right side of the riverbank during both neap flood tide and spring flood tide, resulting in lateral salinity distribution. It is likely due to the effects of cross-channel bathymetry variation, and the lateral density gradients. The effect of temperature variation on stratification at the study site was weak compare to the above mentioned factors.

Besides, the stratification developed gradually from the surface to the bottom of the water column over the ebb tide period primarily is caused by the tidal straining, tidal time scale, and freshwater discharge. The quick response of stratification and de-stratification to tidal changing seems related to the shallow water condition.

The cross-correlation method is used to estimate the time lags between salinity and water level variations. The results indicate that delays in time of salinity range from approximately 38 minutes to 56 minutes, and the phase shifts range from 18.27°–26.92°. The delays in time is affected by the freshwater runoff from upstream.

The density distribution at the observation site has clear tidally periodic characteristic. The saltier water moved from the left side to the right side of the river bank at the end of the flood spring tides, resulting in lateral density distribution. And density variation shows a vertical distribution in the early of the ebb spring tide. During the flood tides, vertical density gradient increases at the middle water column, and lateral density gradient pattern almost remains

unchanged. The lateral density gradient might lead to lateral salinity distributions during flood tides. Besides, the vertical density gradient at the downstream area seems smaller than that at the upstream area, due to the effect of freshwater inflow from the upstream.

CHAPTER 3 LONGITUDINAL DISTRIBUTIONS OF SALINITY AND TIDAL FLOW

3.1 Introduction

Section 1.1.2, Chapter 1 mentions the important role of the Ōta diversion channel as well as the necessity of investigating the longitudinal distributions of salinity and tidal flow using an accurate and cost-effective method. Several previous studies strongly suggest that FATs is a state-of-the-art technique because of its reliable and accurate feature for the long-term measurement of river discharge, even in shallow, wide rivers or tidal estuaries with saltwater intrusions (Soltaniasl et al., 2013, K. Kawanisi et al., 2017, K. Kawanisi et al., 2018).

However, most published studies on salinity intrusion, stratification, estuarine circulation, and salinity flux that employed FATs were implemented using a traditional scheme that included an oblique transmission line and several FAT units. Thus, the main objective of this study is to apply the new FAT deployment pattern to investigate the longitudinal distribution of salinity and tidal flow in a tidal channel.

The aim of this study is to examine the performance of the proposed scheme using the FAT system in terms of providing sufficiently accurate estimates of river discharge in tidal estuaries, a mesoscale estuary, the Ōta diversion channel, in Hiroshima, Japan is used as a case study. The main novelty of this work is the use of a new scheme for the tomographic deployment of the FAT system. Two pairs of four FAT units were installed along a 700 m

length of estuarine floodway in a zigzag configuration. The significance of this work is its exploration of the results of examining the current velocity in both landward and seaward directions.

3.2 Study site

The Ōta River estuary in Hiroshima City, western Japan, is the monitoring site used in this study. A map of the study location is shown in Figure 3.1. The FAT system is deployed about 4.3 km upstream from the estuary. The tomographic scheme is presented in Figure 3.1b, and the CTD-FAT campaigns for validation during a typical spring tide are shown in Figure 3.1c. In this study, a series of four FAT units with different transmission lengths are deployed in a zigzag distribution pattern. The present study focuses on assessing the potential advantages of the zigzag pattern rather than a conventional pattern (i.e., measurement at one cross-section) to trace the velocity behavior over the main channel during flood and ebb tides (i.e., landward and seaward flow directions). As shown in Figure 3.1c, the tomographic zone is extended over 700 m × 170 m. During the observation period, the freshwater runoff is limited by the Gion sluice gates (see Fig. 3.1a) located 4.5 km upstream from the observation site; the cross-sectional area of stream was 32 m × 0.3 m for the spilling flow (Kawanisi et al., 2010). The water level is recorded at Yaguchi Gauging Station located approximately14 km upstream from the river mouth (see Fig. 3.1a).

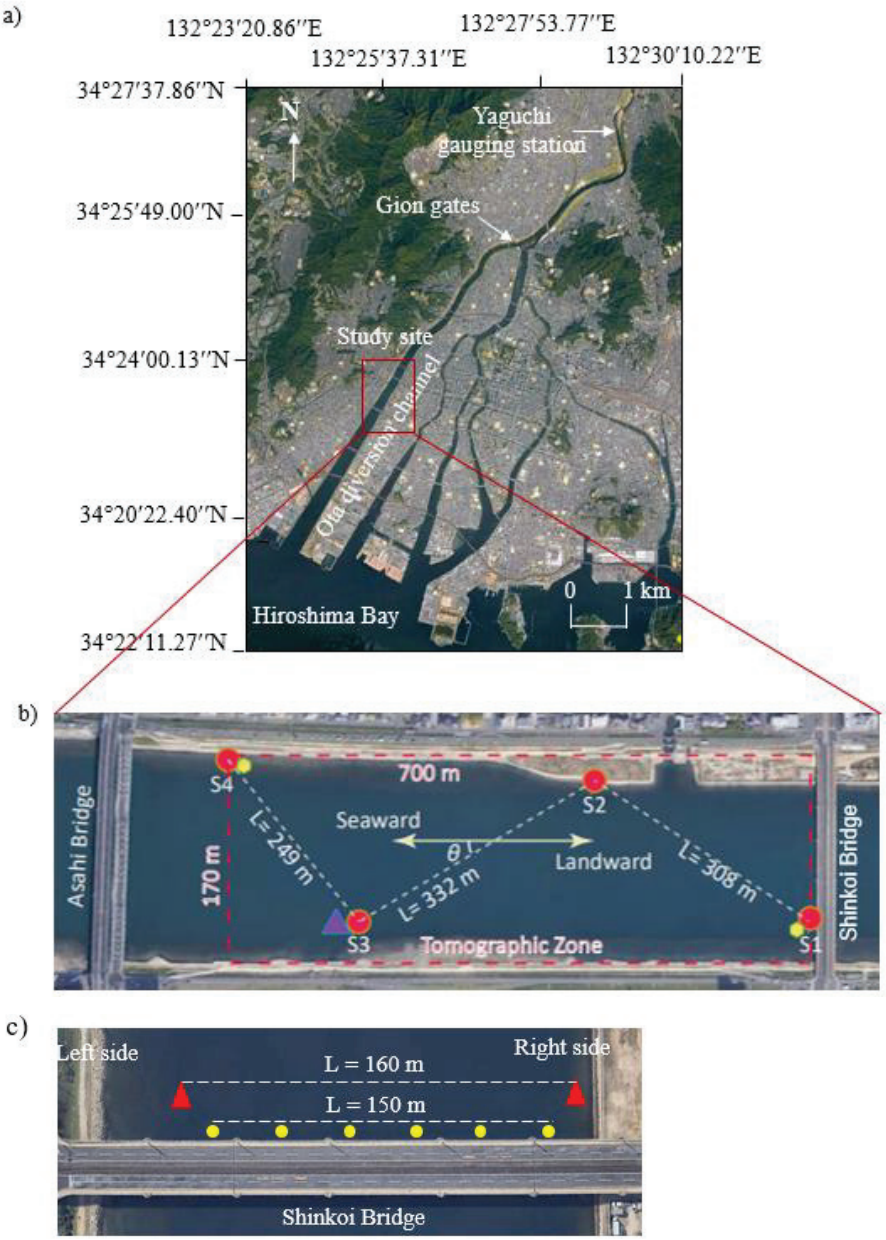

Figure 3.1 a) The location of the field observation at the Ōta diversion channel; b) the arrangement of the tomographic scheme of the FAT system over the diversion channel. Yellow and purple symbols indicate the locations of the CT instruments; and c) the Compact CTD (yellow circles) and FAT (red triangles) campaigns for validating section-average salinity using the FAT system.

The bathymetry distribution of the Ōta diversion channel is presented in Figure 2.2. Figure 3.2 shows the oblique cross-sections between each pair of acoustic stations. The cross-sectional areas along the transmission lines are estimated from the data set collected using Stream-Pro ADCP. In general, the riverbed is irregularly shaped and not flat. The river bed altitudes along

S_1S_2 and S_3S_4 transmission lines have the similar trend that decreases from the left side to the right side of the river while the river bed altitude of the transmission line along S_2S_3 shows the opposite trend, resulting in a meandering along the observation site.

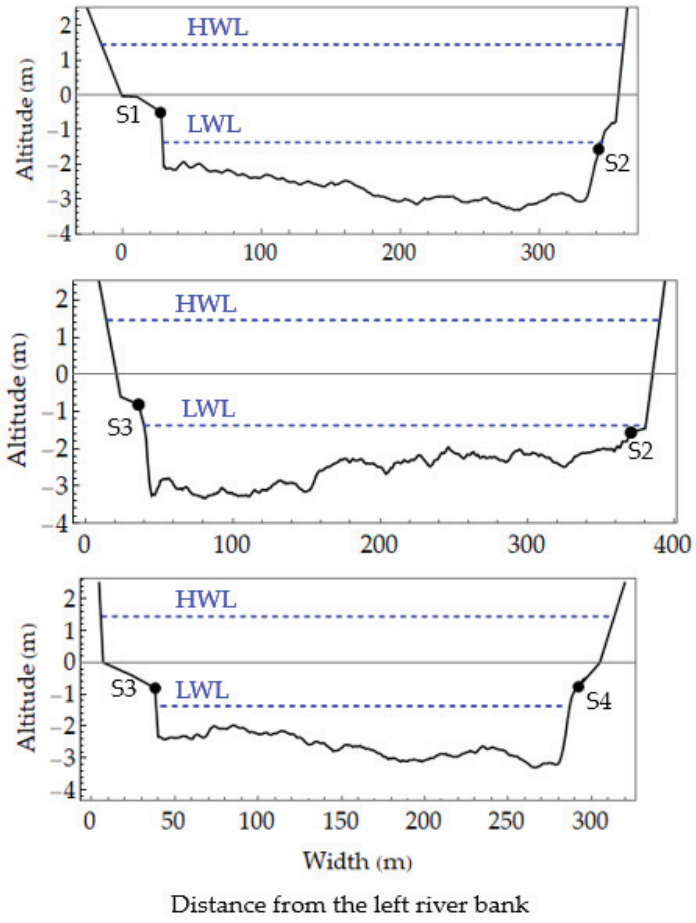

Figure 3.2 Oblique cross-sections along transmission lines between S_1S_2, S_2S_3, and S_3S_4. Dashed lines denote the Highest Water Level (HWL) and the Lowest Water Level (LWL), and black dots denote the locations of transducers.

3.3 Instrumentation

3.3.1 Fluvial Acoustic Tomography (FAT) system

Section 2.3.2, Chapter 2 shows the measurement principle as well as the specifications of FATs. This part will introduce the unique ability of FATs in monitoring the estuarine physics in detail. During a time period of 12 years (from 2010 – 2021), objects of FATs application have expanded continuously in both study area as well as FATs scheme.

FATs can be applied in several kinds of area, including deep, shallow to extreme shallow rivers; tidal and non-tidal rivers; river conjunction; river bifurcation. The required number of the deployed FATs in the field observation also varies diversely, according to the research purpose. For example, to investigate the depth average velocity along a channel, FATs mostly is deployed with a pair of transducers at both sides of the river. To investigate the two-dimension field of velocity/salinity, a network of FATS is required.

In the present study, FATs are used as the main instrument, in the zigzag configuration.

3.3.2 Acoustic Doppler Current Profiler (ADCP)

The Stream-Pro ADCP is an equipment for measuring velocity and discharge in shallow stream (from 0.15 − 6m in depth), using the sound wave′s Doppler effect. Stream-Pro has four broadband transducers (see Fig. 3.3). The monostatic system measures the Doppler shift of the sound pulses under the water in different directions. In this study, we attached this equipment into a moving boat to collect the discharge and river bed shape data along the three transmission lines of FATs (see Fig. 3.1b).

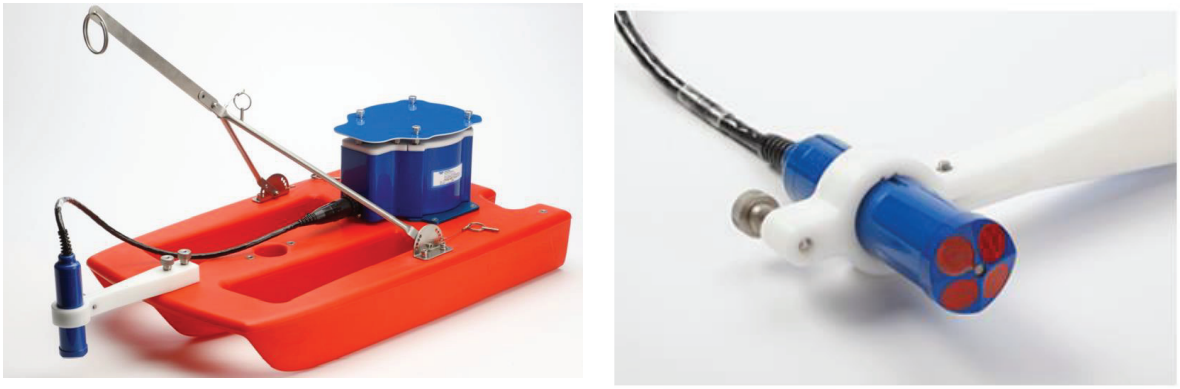

Figure 3.3 StreamPro Acoustic Doppler Current Profiler (ADCP) (*Source: Teledyne Marine*)

Table 3.1 Stream Pro specifications (*Source: Teledyne Marine*)

Max Profiling Range	6m
Max Bottom Tracking Range	7m
Max Depth Detection	7m
Velocity Accuracy (typical)	±1.0% of measured velocity, ± 0.2 cm/s
Velocity Range	±5 m/s

Resolution	0.1 cm/sec
Data output rate	1 Hz
Beam Angle	20°
Standard Sensors	Temperature, tilt, compass
Communications	RS-232, Bluetooth
Weight in air	5 Kg
Dimensions	Electronics housing: 15 x 20 x 10 cm Transducer: 3.5 cm diam. x 15cm length Float: 44 x 70 x 11 cm

3.3.3 CT (Conductivity, Temperature) sensor

INFINITY-CT is an accurate conductivity and temperature meter making use of 7-electrode sensor. This 7-electrode generates an electric current only inside of the conductivity cell, minimizing external influences and improving data quality. Thus, precise salinity measurements are possible under bio-foul forming conditions. The compact design is suitable to be deployed/integrated with various sites/platforms. Some of the technical specifications of CT sensor are presented in Table 3.2.

Table 3.2 CT sensor specifications (*Source: JFE advantech Co., Ltd*)

Model	A7CT2-USB (for shallow water)	
Parameter	Temperature	Conductivity
Principle	Thermistor	7-electrode
Range	-3–45 °C	0.5 – 70 mS/cm
Resolution	0.001 °C	0.001 mS/cm
Accuracy	±0.05 °C (0 – 35°C)	±0.05 mS/cm (28–65 mS/cm)

3.3.4 Other instruments

This study also uses the data that collected using another instruments, such as water level logger, Compact CTD (Conductivity, Temperature, Depth) sensor, remote controlled boat.

3.4 Methodology

3.4.1 The Fluvial Acoustic Tomography (FAT) system

The FAT is an advanced hydro-acoustic instrument designed by Hiroshima University that uses submerged acoustics to observe various hydrological properties of rivers at levels ranging from 0.3 m – 10 m in depth (Razaz et al., 2015, Al Sawaf et al., 2020). FAT emits omnidirectional acoustic signals at different frequencies (mainly between 7–53 kHz). The FAT system contains GPS receiver that helps synchronize FAT units to guarantee the high-precision transmission of pulses. The acoustic pulse was transmitted every 30 secs in the experiments.

In this work, four broadband transducers with a central frequency of 30 kHz were used to measure the cross-sectional average velocity, discharge, and salinity over the period from December 28th 2018 to January 16th 2019, and were deployed as shown in Figure 3.1b. The horizontal distances are shown in Figure 3.1b, with the longest transmission line between S_2S_3 (332 m) and the shortest between S_3S_4 (249 m).

3.4.1.1 Estimating tidal current and water discharge using FATS

FAT system uses the time-of-travel tomography method. The mean velocity along the transmission line (u) and mean speed of sound (c) are evaluated based on respective travel times, (t_{up}) and (t_{down}), at the upstream and downstream stations, as follows:

$$c = \frac{L}{2}\left(\frac{1}{t_{up}} + \frac{1}{t_{down}}\right) \tag{3.1}$$

and

$$u = \frac{L}{2}\left(\frac{1}{t_{up}} - \frac{1}{t_{down}}\right) \tag{3.2}$$

where L is the horizontal spacing between the upstream and downstream stations. For a given cross-section, the section-averaged velocity (V) and discharge acquired by FAT (Q) are calculated using the following equations:

$$V = {}^{u}/_{cos\,\theta} \tag{3.3}$$

$$Q = V \times A(H) \times sin\,\theta \tag{3.4}$$

where *A (H)* is the cross-sectional area along the ray path as a function of the water level (*H*), and θ is the angle between the ray path and streamline.

3.4.1.2 Estimating depth- average salinity using FATS

As described by Medwin (1975), the speed of sound in water is generally a function of salinity, water temperature, and depth:

$$c = 1449.2 + 4.6T - 0.055T^2 + 2.9\,10^{-4}T^3 + (1.34 - 0.01T)(S - 35) + 0.016D \quad (3.5)$$

The cross-sectional average salinity can be deduced from Equation (3.5) as:

$$S = 35 + (c - 1449.2 - 4.6T + 0.055\,T^2 - 0.00029\,T^3 - 0.016\,D)/(1.34 - 0.01\,T) \quad (3.6)$$

where *T* is water temperature (°C), *c* is speed of sound (m/s), *D* is depth (m), and *S* is salinity. The valid parameter ranges in Equation 3.5 are as follows: $0 \leq T \leq 35$ °C, $0 \leq D \leq 1000$ m, and $0 \leq S \leq 45$. This relationship helps estimating the cross-sectional average salinity using the speed of sound in water computed by the FAT system.

3.4.2 Estimating the residual current velocity and residual water discharge

In this study, the term "residual current" refers to the current left after removing the tidal component from the observed current. In general, this residual current might be due to several factors, such as freshwater inflow from the upstream, wind forcing, the interaction of tidal motion and bathymetry, etc.

The residual current and residual discharge in the study will be estimated using low-pass filter method. In this case, digital low-pass filter is used to remove the tidal components from the current and discharge data. The mixed tides in the Ōta river estuary include diurnal and primary semidiurnal components, thus, the cutoff period of low-pass filter was set to the tidal period of 24.5 hours.

3.4.3 Determination of flow direction using FATS

3.4.3.1 Estimating the flow direction

The accurate calculation of the flow direction angle is critical to obtaining precise results. Bahreinimotlagh et al. (2016) proposed an equation for calculating the flow direction, using four transducers to create two crossed acoustic transmission lines. The equation is based on the continuity condition: the water discharge of the two related parts should be equal.

Many factors influence the degree of fluctuation in discharge along the channel. However, it is assumed in this study that the discharge variations are negligible because of the short distance of the study site (700 m). Thus, for simplicity, the degree of discharge fluctuation was not considered in the calculations. Equation 3.7 was used to calculate the temporal variations in the flow direction obtained from the FAT system data:

$$\theta_1 = cos^{-1}\left(\frac{1}{2}\sqrt{\frac{\sqrt{2}cos(\emptyset)\sqrt{A_1^2u_1^2 + cos(2\emptyset)(A_1u_1 - A_2u_2)^2 + 6A_1A_2u_1u_2 + A_2^2u_2^2} + cos(2\emptyset)(A_2u_2 - A_1u_1) + 3A_1u_1 + A_2u_2}{A_1u_1 + A_2u_2}}\right) \quad (3.7$$

where $\emptyset$ is the angle between two transmission lines (e.g., S_1S_2 and S_2S_3). The $\emptyset$ may be expressed as:

$$\emptyset = tan^{-1}\left(\frac{X_2Y_1 - X_1Y_2}{X_1X_2 + Y_1Y_2}\right) \quad (3.8)$$

where X_1, X_2, Y_1 and Y_2 are determined using the coordinates of the acoustic stations.

3.4.3.2 Estimating the relative errors

A formulation of the structure of the relative error was also proposed in this study that included the following five terms:

$$\frac{\delta\theta}{\theta} = \frac{\delta\theta_\emptyset}{\theta} + \frac{\delta\theta_{A_1}}{\theta} + \frac{\delta\theta_{A_2}}{\theta} + \frac{\delta\theta_{u_1}}{\theta} + \frac{\delta\theta_{u_2}}{\theta} \quad (3.9)$$

The error term $\left(\frac{\delta\theta_\emptyset}{\theta}\right)$ represents the uncertainty in the angle between two crossed paths and has a large impact on the error analysis. The second and third error terms $\left(\frac{\delta\theta_{A_1}}{\theta}, \frac{\delta\theta_{A_2}}{\theta}\right)$ are

errors in the water level measurements. The fourth and last terms $\left(\frac{\delta\theta_{u_1}}{\theta}, \frac{\delta\theta_{u_2}}{\theta}\right)$ are errors in the mean velocity along the transmission lines. The detailed equations of these error components are shown in Appendix A.

3.4.4 Estimating the total error components of measurements of water discharge using FATs

An important issue to be addressed in discharge computation is how to quantify the error structures in the discharge measurements made by the FAT system. Kawanisi et al. (2016) stated that the error structure of the discharge estimating by the FAT system is induced by the following terms:

(i) errors in water depth measurements;

(ii) riverbed uncertainties;

(iii) velocity measurements;

(iv) flow direction estimates.

The error structures induced by the discharge measurements of the FAT systems are summarized in Equation 3.10 below:

$$\begin{aligned}\left|\frac{\delta Q_{FAT}}{Q_{FAT}}\right| &= \left|\frac{\delta Q_H}{Q}\right| + \left|\frac{\delta Q_A}{Q}\right| + \left|\frac{\delta Q_u}{Q}\right| + \left|\frac{\delta Q_\theta}{Q}\right| \\ &= \left|\frac{\delta H}{H}\right| + \left|\frac{\delta Z_Z}{H}\right| + \left|\frac{\delta u}{u}\right| + \left|\frac{\delta\theta}{\cos\theta\ \sin\theta}\right|\end{aligned} \tag{3.10}$$

where:

$\left|\frac{\delta Q_H}{Q}\right|$: $\left|\frac{\delta H}{H}\right|$ is the error component that relative to the mean water depth;

$\left|\frac{\delta Q_A}{Q}\right|$: $\left|\frac{\delta Z_Z}{H}\right|$ is the error component that relative to the imperfection of the bathymetry survey and the variations of the bottom shape;

$\left|\frac{\delta Q_u}{Q}\right|$: $\left|\frac{\delta u}{u}\right|$ is the error component that relative to the velocity deduced from FATs;

$\left|\frac{\delta Q_\theta}{Q}\right|$: $\left|\frac{\delta\theta}{\cos\theta\ \sin\theta}\right|$ is the error component that relative to the angle between the flow direction and the transmission line.

Finally, the results of the error calculation process were compared with the results of the moving boat Stream – Pro ADCP (Acoustic Doppler Current Profiler), which measured at the same three transmission lines for 2 days (December 12-14th 2019).

3.4.5 Longitudinal distributions of salinity, salinity gradient, and dispersion coefficient

The salinity gradient and dispersion coefficient is estimated using the distribution of longitudinal salinity. The longitudinal dispersion coefficient indicates the capacity of a river flow to scatter substances in the longitudinal direction. In a normal channel, the advective transport is proportional to the water velocity and longitudinal concentration gradient. Salinity transport may be calculated using the following equation:

$$\frac{\partial S}{\partial t} + u\frac{\partial S}{\partial x} = D_x \frac{\partial^2 S}{\partial x^2} \tag{3.11}$$

where S is the section-averaged salinity, u is the water velocity, x is the distance upstream from the estuary's mouth, and D_x is the longitudinal dispersion coefficient.

3.4.6 Measurements of temperature, depth, and bathymetry

As mentioned in the previous section, Stream-Pro ADCP (Teledyne RDI; Stream-Pro Acoustic Doppler Current Profiler) was used to obtain the data on the bathymetry of the riverbed of the monitored cross sections and to determine the flow directions for the measured flow. In addition, the discharge data generated by the Stream-Pro ADCP was compared to the discharge estimated by FAT. During the observation period, the moving-boat ADCP campaigns were regularly carried out.

The temporal variations in water temperature were measured using three CT (conductivity and temperature) sensors attached to tripods side-by-side to the S_1 station at 0.52 m, S_3 station at 0.5 m and S_4 station at 0.4 m above the bottom. The temperature data were used to calculate salinity using Equation 3.6 (see Fig. 3.1).

The temporal variations in water level (H) were recorded using water level loggers deployed side-by-side at each acoustic station (i.e., at S_1, S_2, S_3, and S_4). The water level records provided temporal data on water surface heights, which were used to measure the temporal variations of the cross-sectional area at each transmission path.

3.4.7 Confirming the FATS feasibility to measure the section-average salinity

CTD campaigns were carried out at two FAT units between the left and right sides of the river bank concurrently along Shinkoi Bridge during a typical spring tide to confirm the feasibility of the FAT system for measuring the section-average salinity. The measurements of

salinity distribution in the cross-sectional were taken on October 2nd 2020, from 08:20 to 23:30 (see Fig. 3.1c). During these campaigns, two FAT units were deployed on the left and right sides of the river near Shinkoi Bridge with a transmission length of 160 m. The CTD collected the vertical salinity distribution at six points along the bridge every thirty minutes.

3.5 Results

3.5.1 Temporal variations in water level along the channel

The temporal variations in the water levels recorded at S_1S_2, S_2S_3, and S_3S_4 are shown in Figure 3.4. Compared to the average water level in Tokyo Bay (T.P), the water level was estimated to evaluate the temporal variations of the cross-sectional area for each section. In the present study, water level data was collected from the water level loggers that were attached into the transducer tripod at each station. The missing data occur at the low water periods during the spring tide because of the instrument were dried out.

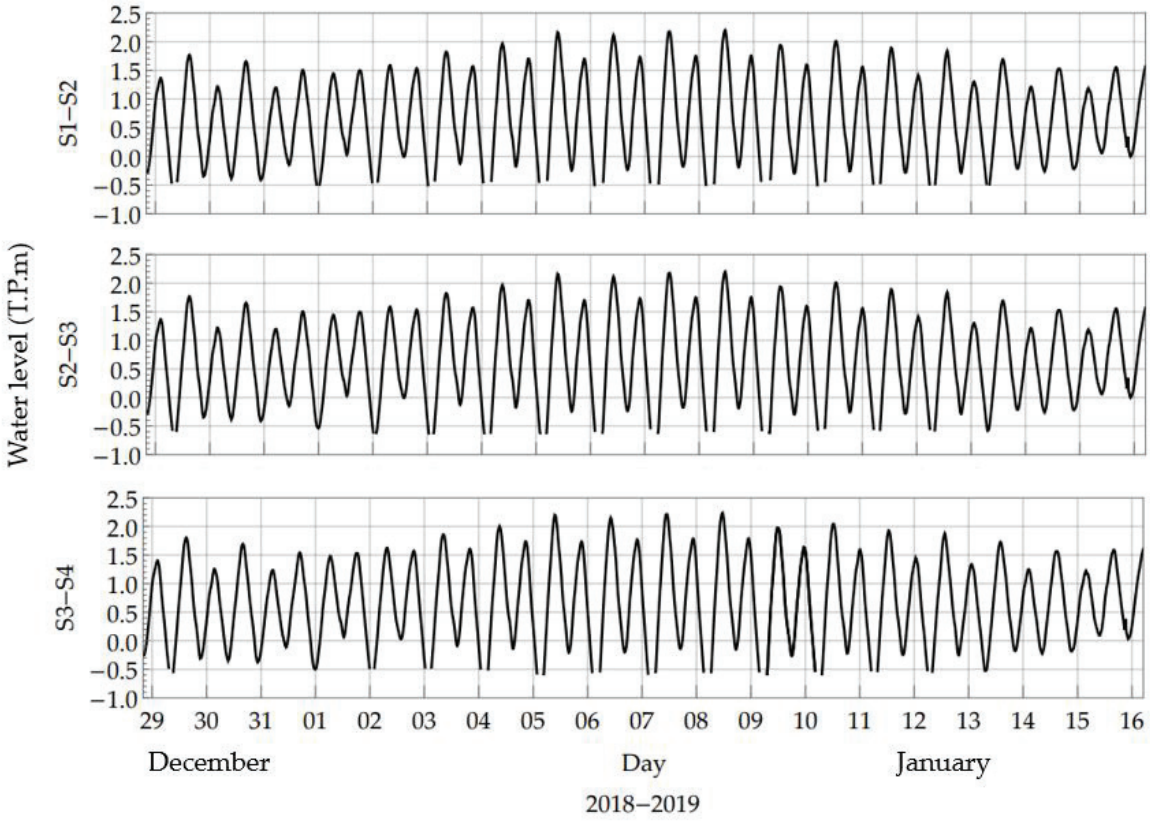

Figure 3.4 Temporal variations of water level during the study period recorded at the observed cross-sections.

3.5.2 Temporal variations in tidal velocity distribution along the channel

3.5.2.1 Tidal velocity

The time series of the tidal current (denote by black lines) and residual current (denote by red lines) velocities recorded by the FAT stations are shown in Figure 3.5. The missing periods resulted from the abovementioned problems during the monitoring program and the drying out of the transducers.

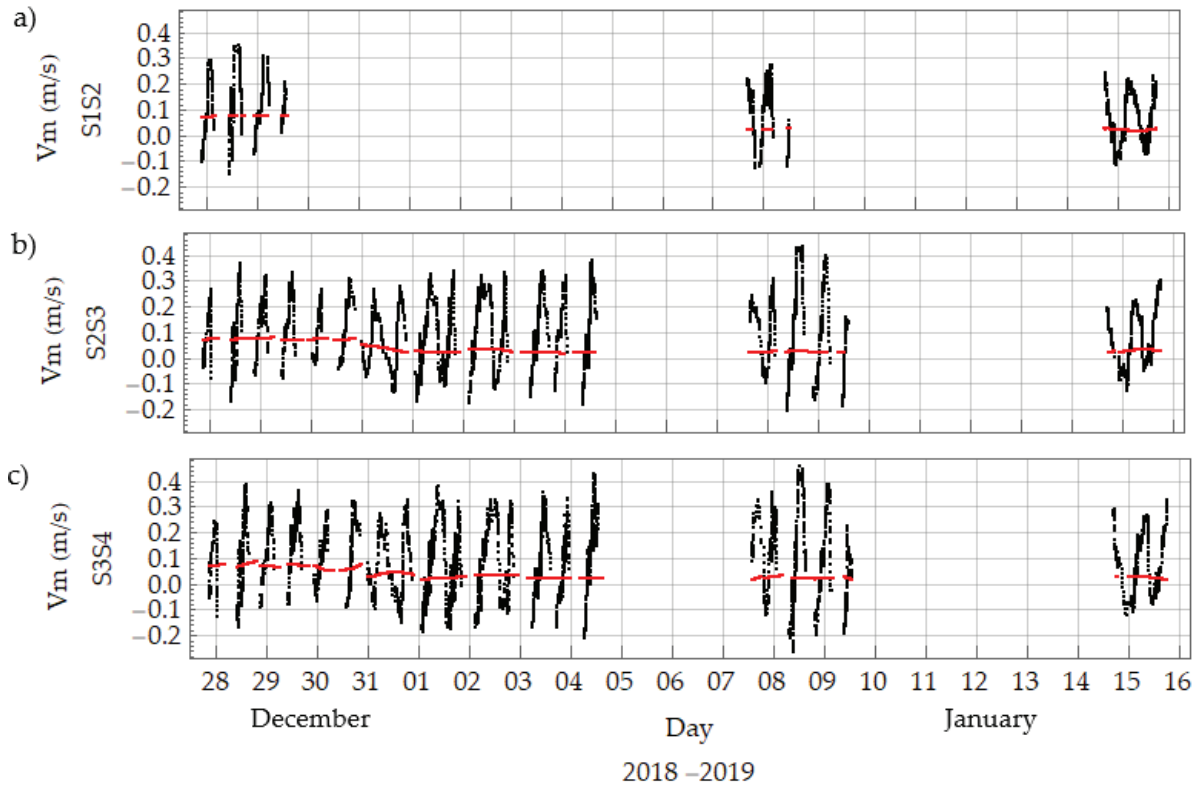

Figure 3.5 Time series for the tidal current velocities (black lines) and the residual mean velocity (red lines) measured using FAT at the selected stations during the study period.

In general, the comparison between Figures 3.4 and 3.5 shows that the tidal current pattern is corresponding to the water level pattern at all three sections.

The observed current velocities at the upstream area (S_1S_2 section) are smaller than those at the downstream area (S_3S_4 section) during the observation period. In the S_2S_3 and S_3S_4 sections (see Fig. 3.5b and 3.5c), the velocity fluctuations during neap tides (December 29th 2018 – January 3rd 2019) were smaller than those during spring tides (January 4–9th 2019). The maximum ebb-tide velocity was roughly 0.45 m/s that found at the downstream areas (S_3S_4 transmission line) and the highest value of flood-tide velocity was estimated as − 0.25 m/s. The

S_3S_4 transmission line registered the highest ebb-tide velocity (approximately − 0.45 m/s), and the lowest velocity (approximately − 0.25 m/s) on 8 January 8th 2019.

3.5.3 Flow direction variations

Equation 3.7 was used to calculate the temporal fluctuations in flow direction using data obtained from the FAT system. The input data for calculating the flow direction are the angle between two transmission lines; the cross-sectional areas; and the current velocity of the three transmission lines.

3.5.3.1 The angle between two transmission lines

The angle between two transmission lines (i.e. S_1S_2 and S_2S_3) is calculated using Equation 3.8. The coordinates of the four acoustic stations are presented in the Table 3.3. Figure 3.6 shows the results of the angles of 63.54° and 82.62° between S_1S_2 - S_2S_3 and S_2S_3 - S_3S_4 transmission lines, respectively.

Table 3.3 The coordinates of the acoustic stations

Acoustic station	Latitude (degree)	Longitude(degree)
S1	34°23'44.6672"N	132°25'54.1499"E
S2	34°23'39.9654"N	132°25'43.5100"E
S3	34°23'29.2019"N	132°25'43.8700"E
S4	34°23'27.9484"N	132°25'34.2716"E

Figure 3.6 The angle between the transmission lines

3.5.3.2 The variations in area cross the channel at the three transmission lines

In this study, the cross-sectional area along the transmission line is estimated from the bathymetry data collected by Stream-Pro ADCP and the water level collected by the water loggers (see Chapter 4, Section 3.4.5). Figure 3.7 shows the cross-sectional areas variations at three transmission lines. The S_3S_4 section has the smallest cross-sectional area while S_2S_3 has the biggest cross-sectional area.

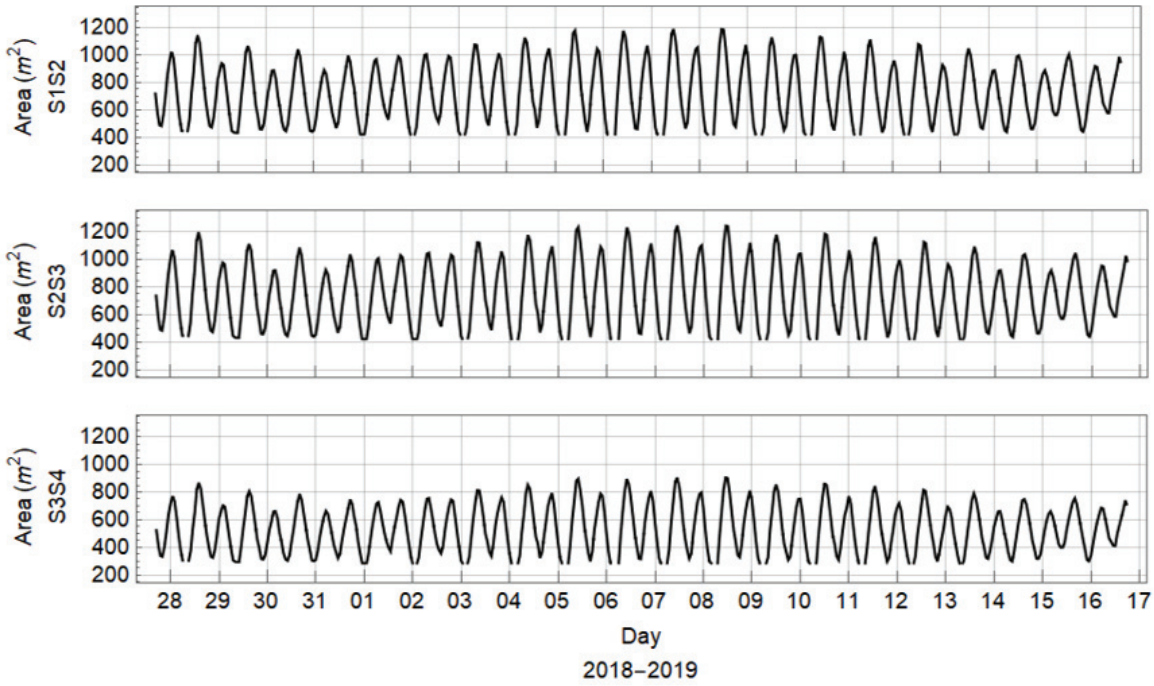

Figure 3.7 Temporal variations of cross-sectional area during the study period recorded at the three observed transmission lines

3.5.3.3 Flow direction variations deduced from FATS

Figure 3.8 shows the variations of the flow direction at three transmission lines. In general, the fluctuated ranges of the angle between the flow and transmission lines for all three sections are approximately 2.2 degrees. Moreover, the variations in the mean flow direction over the three cross-sections are 17.3–19.4°, 45.4–47.6°, and 35.9–38.2° for S_1S_2, S_2S_3 and S_3S_4 section, respectively.

The estimation of the averaged angles gained from ADCP for the monitored cross-sections were θ = 18.29° for S_1S_2, θ = 46.33° for S_2S_3, and θ = 37.31° for S_3S_4. The minor deviations between the FAT and ADCP estimates further confirm the acceptable efficiency of obtaining flow direction measurements using FAT.

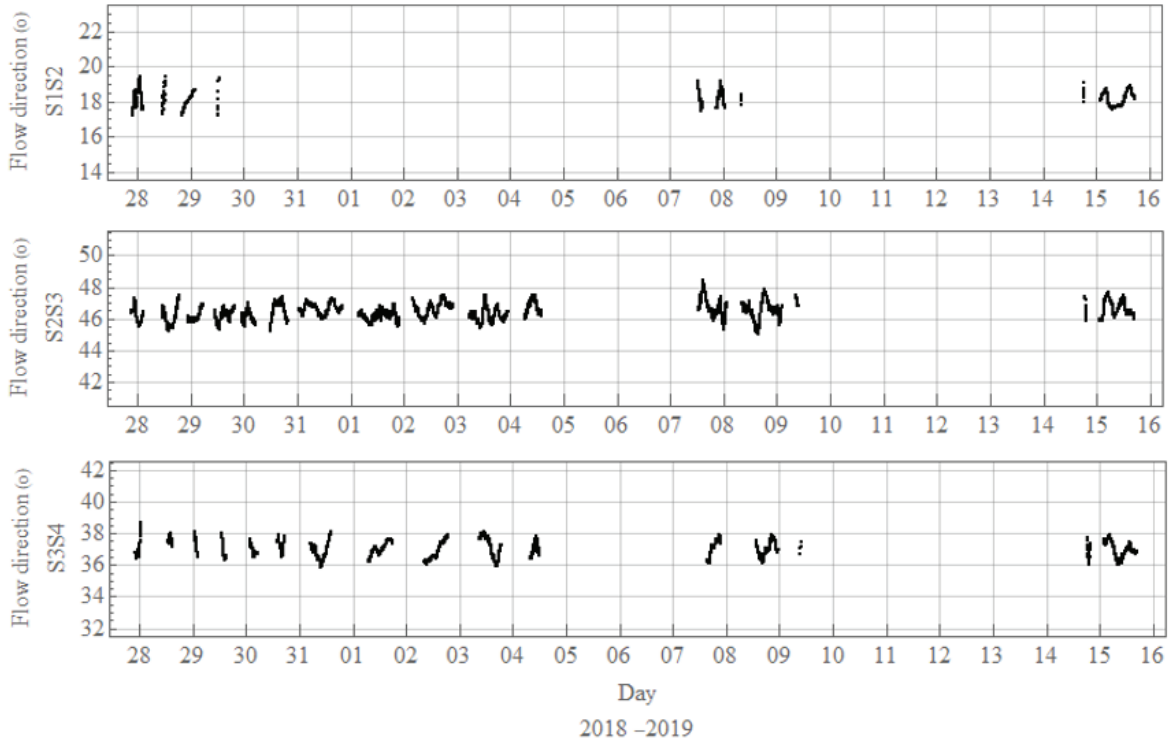

Figure 3.8 The variation of the flow directions along three sections deduced from FATS

3.5.3.4 The relative errors

The error analysis results of the angle estimation $\left(\frac{\delta\theta}{\theta}\right)$ were calculated using Equation 3.9, with the maximum relative errors shown to be approximately ± 6%, which was acceptable.

3.5.4 Estimating water discharge along the channel

3.5.4.1 Estimating water discharge and residual water discharge

The angles with tidal current velocities and cross-sectional areas were used to calculate flow rate using Equation 3.4, as shown in Figure 3.9. The variation in water discharge corresponded with that of the tidal current, with the peak discharge during the ebb tides rising to approximately 200 m^3/s. It is evident that the ebb-tide discharges were twice as high as the flood-tide discharges over the study period.

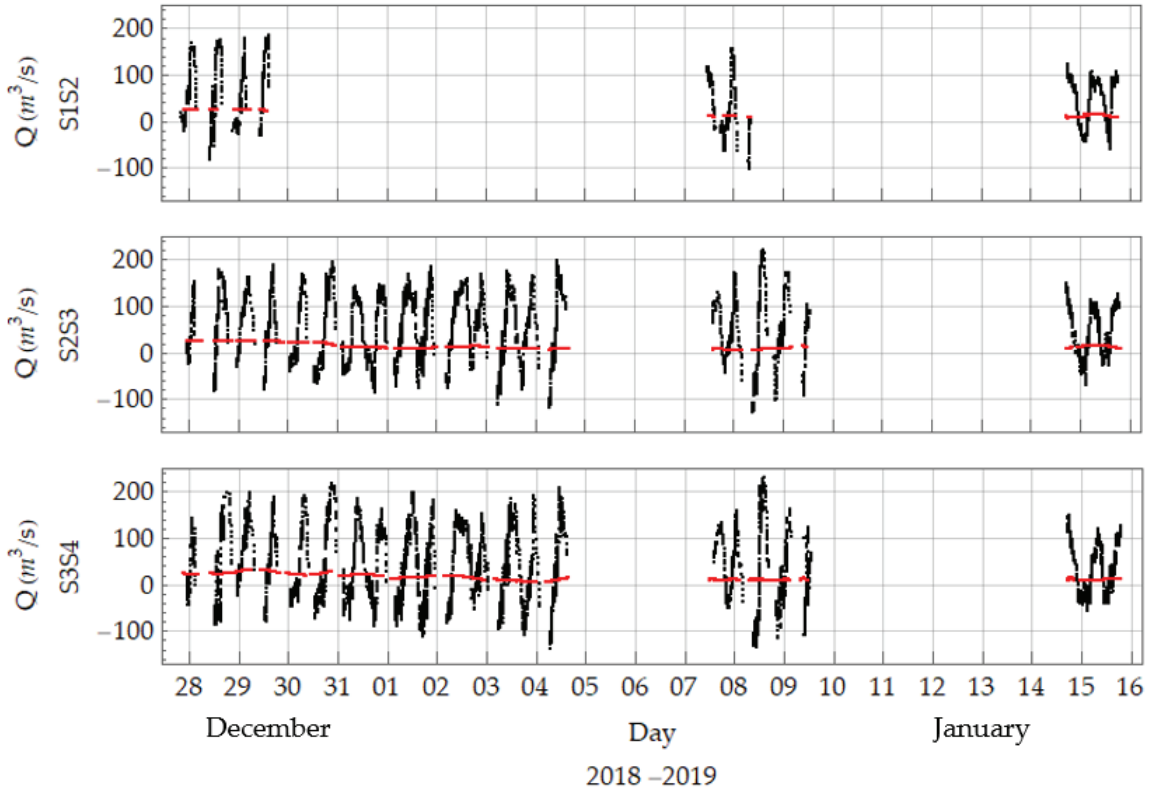

Figure 3.9 Temporal variations in water discharge (black) and residual flow (red) estimated using FAT at the selected stations during the study period

3.5.5 Residual current and residual water discharge

The residual velocities and residual water discharges (plotted in red) of the three cross-sections during the study period are presented in Figures 3.5 and 3.9, respectively. These residuals are relatively complex, as the values reflect the contribution of several elements, including tidal propagation, direct and indirect wind forces, surface waves, horizontal and vertical density gradients, and upstream freshwater velocity. The interaction between the tidal

component and any of these components may significantly affect the generation process of the residual. Therefore, the suitable filtering was used in this study to prevent these non-tidal components from contributing to the residuals.

In this work, the residual (non-tidal) velocities were derived by filtering O_1 that is lunar diurnal constituent with a tidal cycle period of approximately 25.8 h. However, this frequency band removes the tidal component and cannot efficiently judge the effects of this component. As shown in Figure 3.5, the residual current trend is likely to remain unchanged along with the study site. The maximum value of 0.06 m/s occurs in December 2018, declining to around 0.03 m/s in January 2019. Similarly, the mean residual discharge variations at all three sections are largely similar, with the maximum value of 15 m^3/s reaches in the last three days of 2018, and decreases by half to 7 m^3/s by the end of the period.

The freshwater runoff from the upstream of the Ōta River is regulated by an array of gates located near Gion Bridge. Under normal conditions only one gate is open. On regular days, the inflow discharge is around 10–20% of the Ōta River flow rate. As shown in Fig. 3.10, the maximum freshwater runoff recorded at Yaguchi Gauging Station is 60 m^3/s in late 2018. It declined to approximately 35 m^3/s in January 2019. Thus, the residual current at the study site is influenced almost by the upstream freshwater flow.

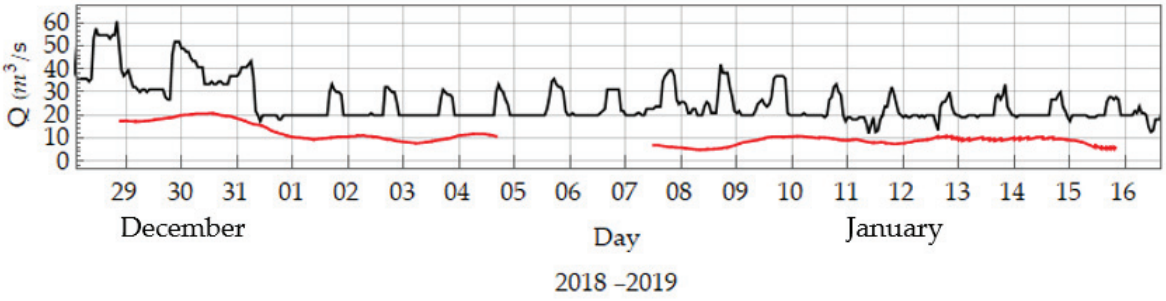

Figure 3.10 Comparison of the freshwater release from the Yaguchi Station (black) and the residual discharge as estimated using FAT (red).

3.5.6 Temporal variations in salinity

3.5.6.1 Cross-sectional average salinity deduced from FATS

Figure 3.11 shows the variations of cross-sectional average salinity deduced from FATs, using Equation 3.6. It is clearly seen that, during the observation site, the maximum value of

the depth-average salinity in the upstream area (section S_1S_2) is lower than that in the downstream area (section S_3S_4).

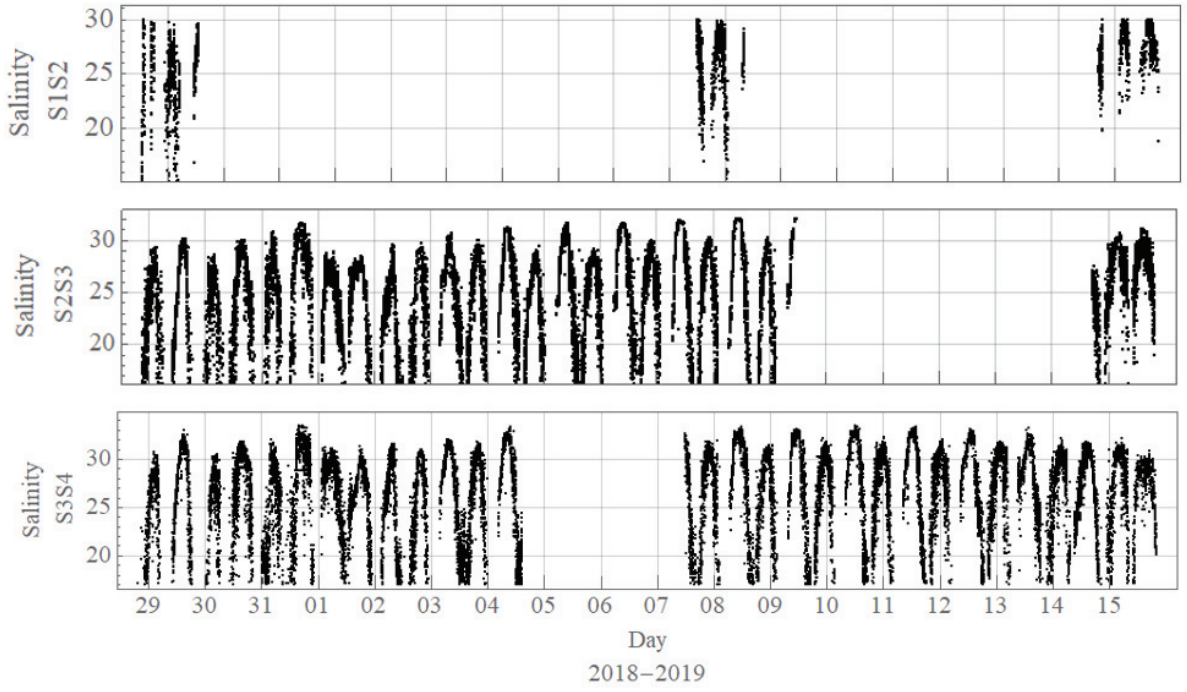

Figure 3.11 The variations of cross-sectional average salinity estimated using FATS at three transmission lines

3.5.6.2 Longitudinal salinity distribution

The longitudinal distributions of salinity and salinity gradient as deduced using the FAT system during a typical spring tide and a typical neap tide, respectively, are shown in Figure 3.12.

In general, along the observation site the depth-averaged salinity and the fluctuations in the salinity gradient followed the opposite trends during both the spring and neap tides, with the former decreasing upward and the latter increasing upward.

As shown in Figure 3.12, the cross-sectional average salinities show a decline in the landward direction throughout the observation period, which was likely attributable to the impact of incoming freshwater.

The differences in cross-sectional average salinity between the downstream and upstream areas of the study site are found to be approximately 0.5–1.6 psu during spring tide and approximately 0.7–1.3 psu during neap tide. Moreover, the axial salinity during neap tide is

approximately 0.5 psu higher than during spring tide, while the salinity gradients along the channel are lower during spring tide than neap tide. Therefore, at the study site, the variations in salinity were significantly lower during spring tide, which may be explained by the different degrees of tidal mixing seen during the two tides, with the larger degree of tidal mixing that occurs during spring tides weakening the salt intrusion.

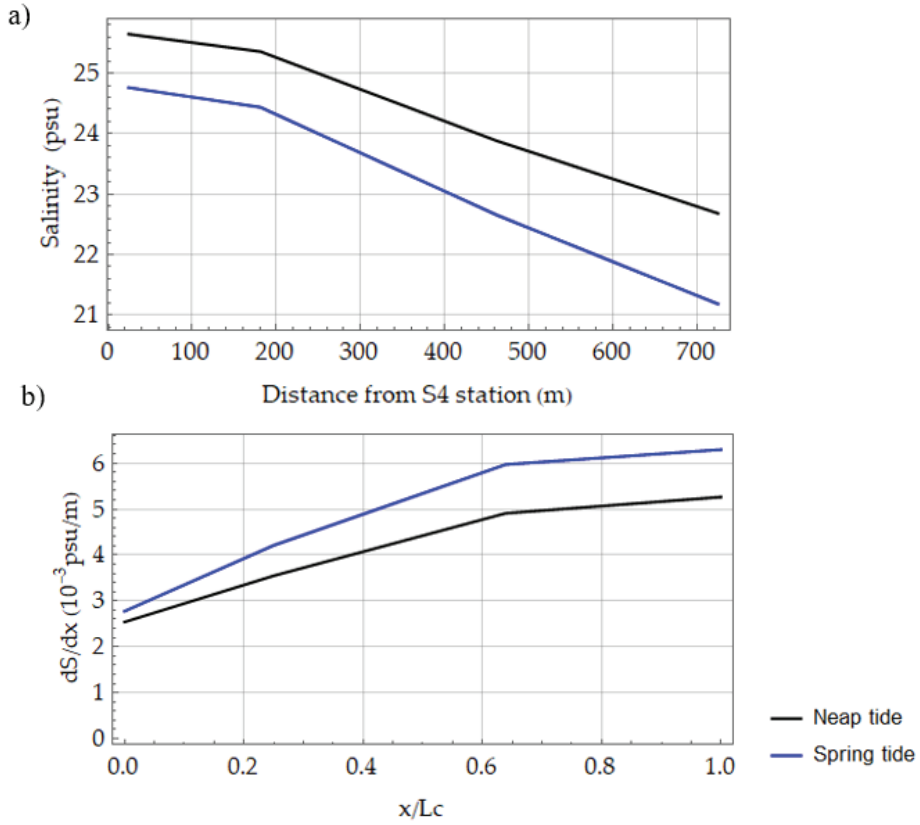

Figure 3.12 a) Longitudinal distributions of salinity, and b) salinity gradient deduced using the FAT system during spring tide and neap tide. "x" is the distance along the river from S_4 station, "L_c" is the longitudinal distance from S_4 to S_1 stations

3.6 Discussions

This work was designed to assess the performance of a promising tomographic system for monitoring the cross-sectional average velocity, discharge and salinity variations with high temporal resolutions over long time periods. The observation program in this study ran for three weeks. During the observation, FAT data were occasionally lost because of factors including transducer cable corruption (due to human error, marine transport, etc.) and battery shutdown. However, the obtained data were adequate to describe the tidal dynamics at the target site.

3.6.1 Tidal asymmetry

Figures 3.4 and 3.5 present the correspondence between the variation trends of water level and tidal current. For further details, Figures 3.13 and 3.14 present the comparison between tidal current and water level along the study site during a typical spring and neap tides, respectively.

During the lowest water slacks, the FATs data and thus, the velocity data are lost because the transducers are out of water. To recover the missing data during the low water slacks, an interpolation method is applied. This method was described in detail in (Bain et al., 2019). Figures 3.13 and 3.14 are plotted after applying the interpolation method.

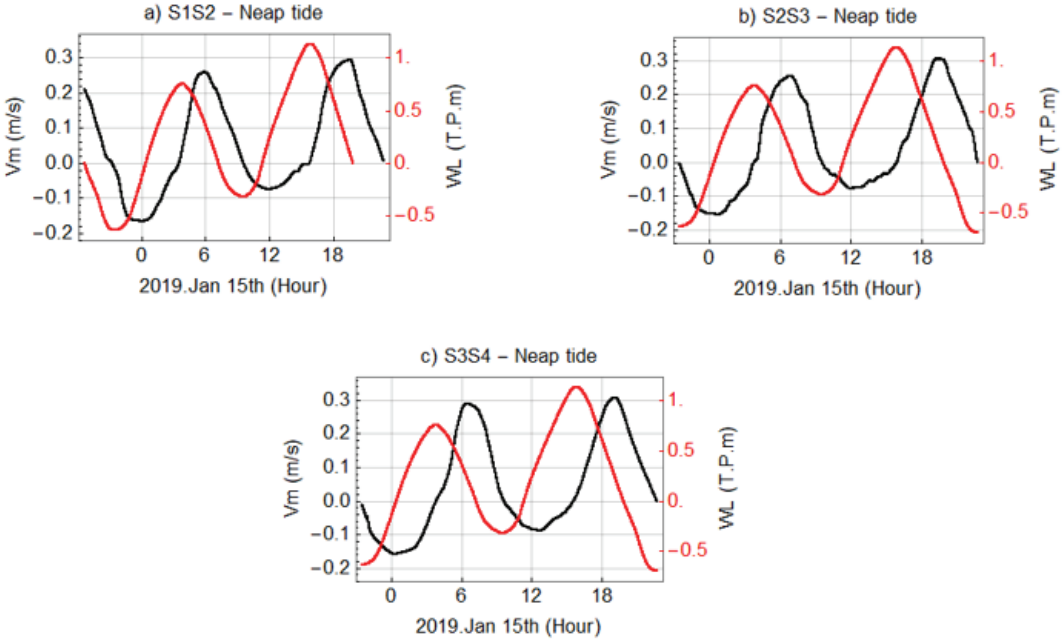

Figure 3.13 Comparison between tidal current (black lines) and water level (red lines) at three sections during a typical spring tide.

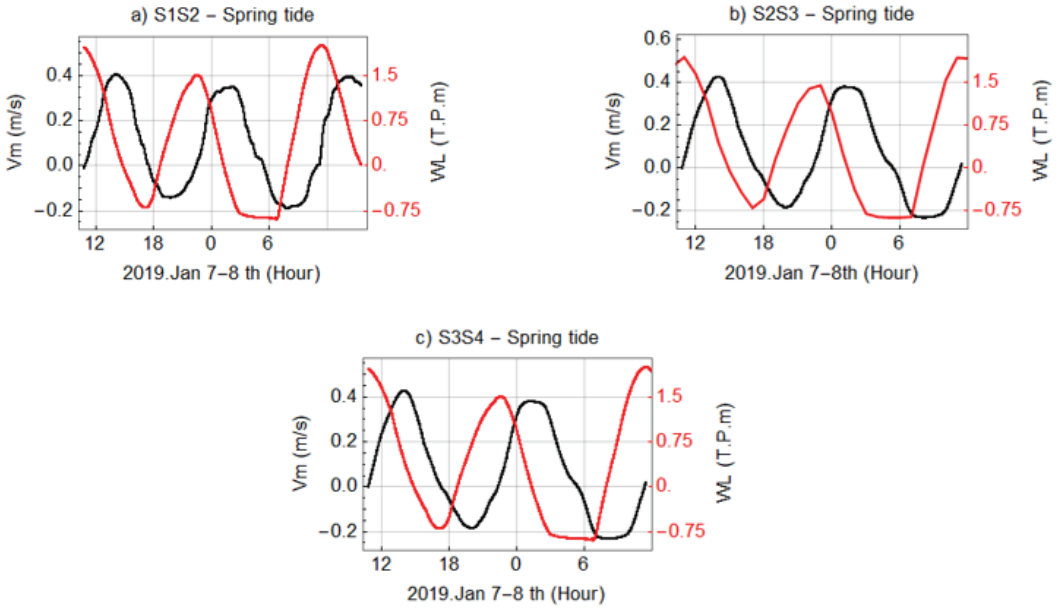

Figure 3.14 Comparison between tidal current (black lines) and water level (red lines) at three sections during a typical neap tide.

In Figures 3.5, 3.13 and 3.14, the tidal current during ebb-tides double the flood-tide current, and the ebb-tide discharges were twice as high as the flood-tide discharges over the study period (see Fig. 9). The asymmetrical character of the tide indicates that the Ōta River estuary is ebb-dominant.

Generally, when tidal waves from the ocean spread into a shallow area, the water tides in that shallow region will surge, which might convince tidal asymmetry (Kang & Jun, 2003, Boon & Byrne, 1981, Fitzgerald & Nummedal, 1983). Furthermore, Hoitink et al. (2003) and Song et al. (2011) addressed that flow asymmetry is closely associated with astronomical tides. The previous researchers suggested that the tidal asymmetry phenomenon in mixed tidal estuaries is usually related to the relationship between the phase of O_1, K_1 and M_2 tidal constituents. Hoitink et al. (2003) proposed an equation to indicate the degree of tidal asymmetry as: $\theta = cos\,(\phi_{u(O1)} + \phi_{u(K1)} + \phi_{u(M2)})$, with $\phi_{u(O1)}$, $\phi_{u(K1)}$, and $\phi_{u(M2)}$ are the phase of O_1, K_1 and M_2 respectively. Tidal flows will be symmetric, flood dominant or ebb dominant if $\theta = 0, > 0$, and < 0, respectively.

The results of the harmonic analysis for observed tidal within the observation time period show that $\phi_{u(O1)} = 191.3°$, $\phi_{u(K1)} = 219.67°$, and $\phi_{u(M2)} = 273.6°$, thus $\theta = -0.736$, revealing an ebb dominance. This is suggested that the ebb tidal asymmetry in the Ōta diversion channel generated by the relation of $O_1 - K_1 - M_2$ tidal constituents.

3.6.2 Confirming the FAT ability to measure water discharge

To investigate the quality of the obtained data, the discharge acquired using the FAT system in this study were compared to independent ADCP data acquired from scans of the Asahi Bridge downstream area (see Fig. 3.15b). The temporal fluctuations in the streamflow computed using the FAT systems were shown to be the same at all cross-sections based on the continuity equation. Thus, the records estimated from the S_3S_4 section were used for further comparisons. As shown in Figure 3.15a, the water flow obtained using the FAT system (black dots) is synchronous with the ADCP estimates (blue points). This provides strong evidence in support of the ability of the FAT system to accurately capture flow variations. Moreover, the association between the respective discharge estimates of FAT and ADCP is illustrated in Figure 3.15b. Both estimates show a similarity with a very high determination coefficient value ($R^2 = 0.994$), a bias of 4.78 m^3/s, and a low RMSE of 10.18 m^3/s (13.82 %).

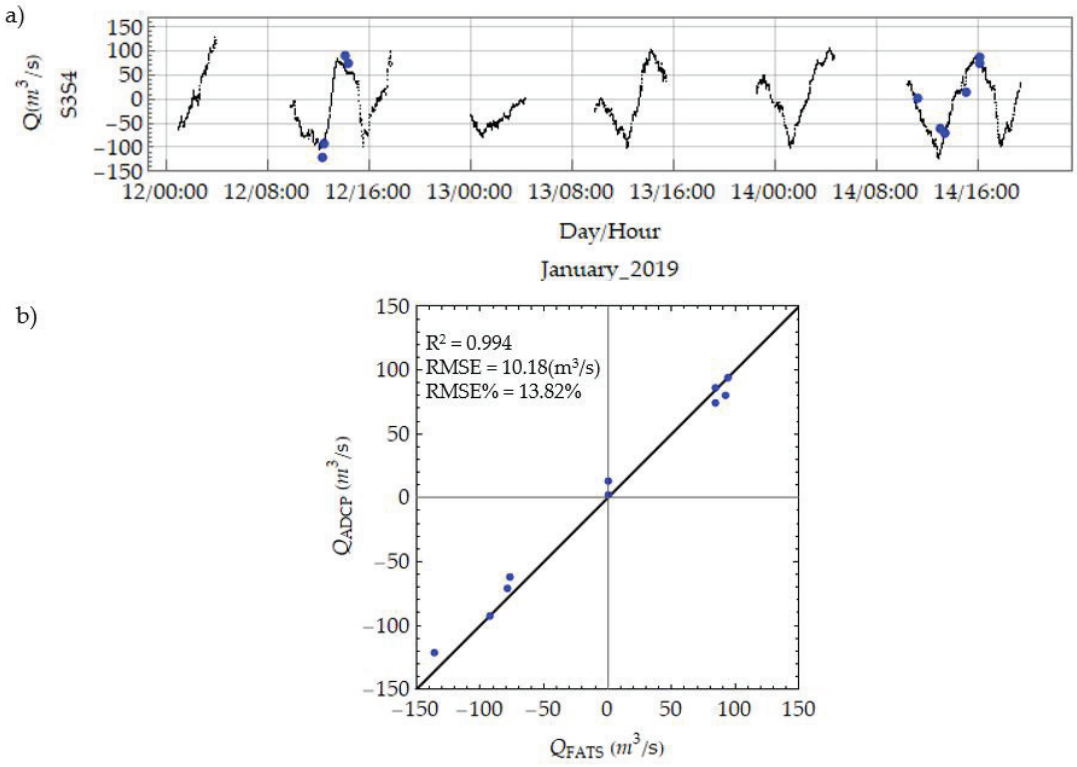

Figure 3.15 Comparison of the discharges acquired using the FAT (black) and ADCP (blue) and (b) The association between the FAT and ADCP estimates.

3.6.3 Error structure for the river discharge measurement

As mentioned in Chapter 3, Section 3.4.4, the deviations in FAT river discharge measurements may be estimated using Equation 3.10. Water depth and area are the functions of mean water depth (H). The measurement errors of the water level loggers and the ADCP moving boat, as obtained from their specification manuals, are $|\delta H|$ = 0.01 m and $|\delta Z_{Bm}|$ = 0.05 m, respectively. Water depths at the study site range from 1 m to 4 m. Hence, the uncertainty of the cross-sectional area ranges from 0.015 to 0.06, or 1.5% −6%.

In addition, the deviations in the velocity term deduced using FAT are $|\delta u_m|$ = 0.012 m/s, and the velocity along the three ray paths vary from − 0.18 m/s to 0.4 m/s (Fig. 3.5). Thus, the measurement errors in the velocity resolution of FAT are 0.03–0.07, or 3%−7%.

The final term in the present case is attributable to the flow direction fluctuations and is given as $\left(\frac{\delta Q_\theta}{Q}\right)$. In this research, the angle between the streamline and the ray path is estimated using Equation 3.6, based on the velocities measured by FAT. Because of the angle between the ray path and the streamline, the terms of discharge uncertainty are around ± 0.045, or 4.5% for all three selected stations during the study period. Thus, the maximum probable error is estimated as 17.5%, which is considered acceptable.

3.6.4 The practicability of using the FATs to measure the depth average salinity

The ability of the FAT system to accurately measure the salinity in a tidal estuary and monitor the salinity intrusion in a tidal floodway was demonstrated previously (Kawanisi et al., 2011, Kawanisi et al., 2015). In previous research, CTD and FAT campaigns were conducted simultaneously to confirm the feasibility of using the FAT system to measure the section-average salinity.

As shown in Figure 3.16a, the salinity deduced using FAT (black line) and Equation 3.6 is similar to the CTD estimates (blue points). The association between the salinity estimates obtained using FAT and Compact CTD, respectively, is illustrated in Figure 3.16b. Both estimates show a similarity with a very high determination coefficient value (R^2 = 0.938), a bias of 0.275 psu, and low RMSE of 1.038 psu (4.325%). These observations provide further evidence that the FAT system is a reliable and accurate technique for the continuous monitoring of variations in salinity. In addition, the FAT dataset collected at three sections along the study site was used to calculate the section-average salinities, which were subsequently used to calculate the longitudinal distributions of salinity.

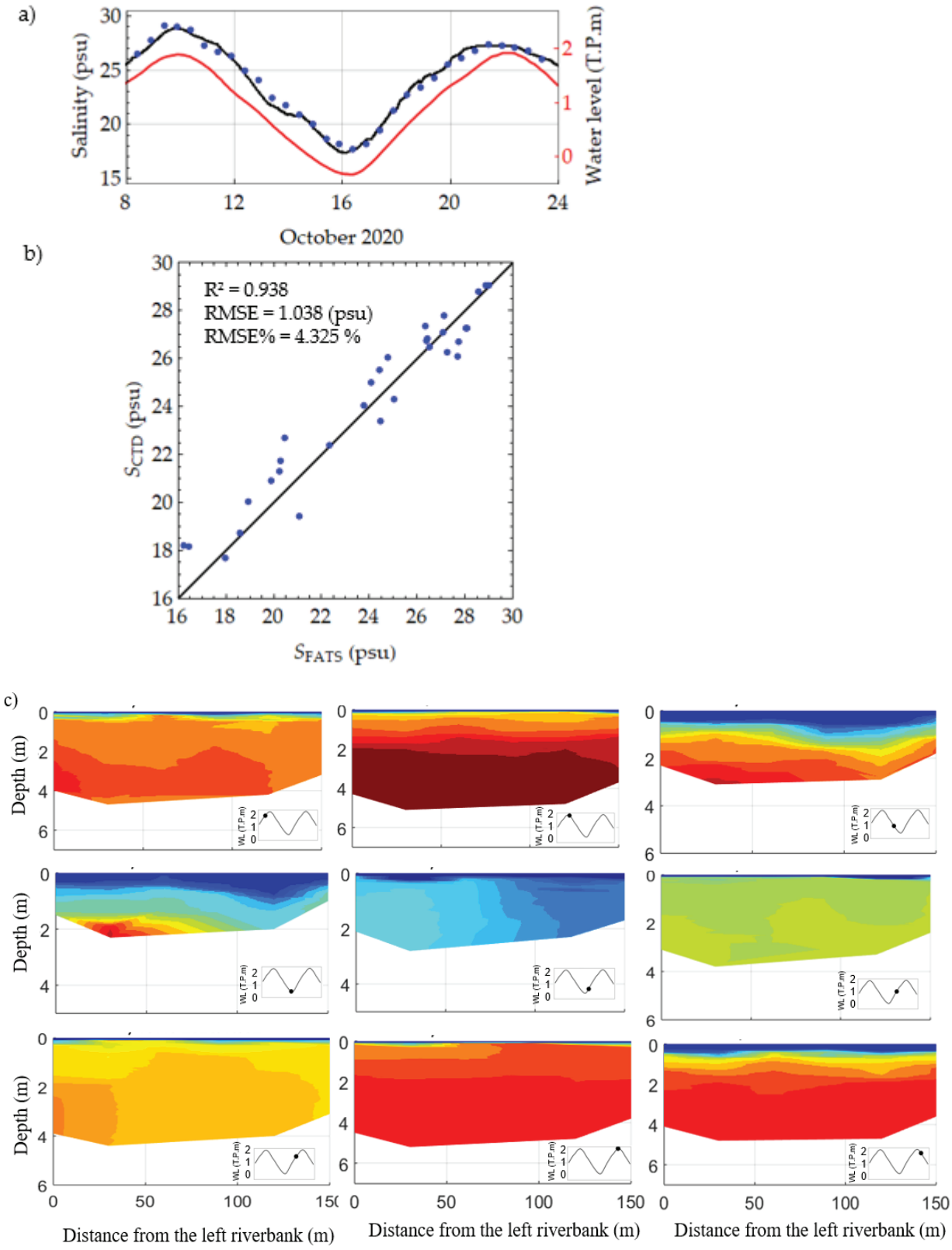

Figure 3.16 (a) Water level variation (red line), and the comparison between the salinity acquired using FAT (black line) and Compact CTD (blue dots) at Shinkoi Bridge, (b) The

association between the FAT and Compact CTD estimates, and (c) Salinity distributions obtained using Compact CTD.

3.6.5 Longitudinal dispersion coefficient

The dispersion coefficient is used to quantify the local scattering of salt to adjacent areas. In this study, only the longitudinal dispersion coefficient was used, as longitudinal scales are generally larger than either transverse or vertical scales. Savenije (1993) stated that the salt intrusion process is ruled by three mechanisms, which include riverine–hydraulic dispersion, tide-driven dispersion, and gravitational circulation or density-driven dispersion.

As riverine-hydraulic dispersion is primarily influenced by geometric shapes and is small compared to tide- and density-driven dispersions, it may be eliminated (Kawanisi et al., 2015). Other researchers have used other approaches (e.g., the longitudinal salt flux decomposition or the modelling approach) to verify which mechanisms are dominant in an estuary. In this research, the longitudinal dispersion coefficient deduced from the water velocity and salinity based on Equation 3.10 is discussed.

As shown in Figure 3.17, the horizontal dispersion generates a relatively small dispersion coefficient upstream and a significantly increased coefficient downstream. In general, the dispersion coefficient depends primarily on the cross-sectional fluctuations in the velocity and salinity (see Eq. 3.11). In the Ōta diversion channel, the change of cross-sectional average velocity is found to increase toward the mouth of the river (see Fig. 3.5), and the axial salinity gradient is higher in the upstream section than the downstream section. As a result, the longitudinal dispersion coefficient increased as the distance to the mouth of the river decreased.

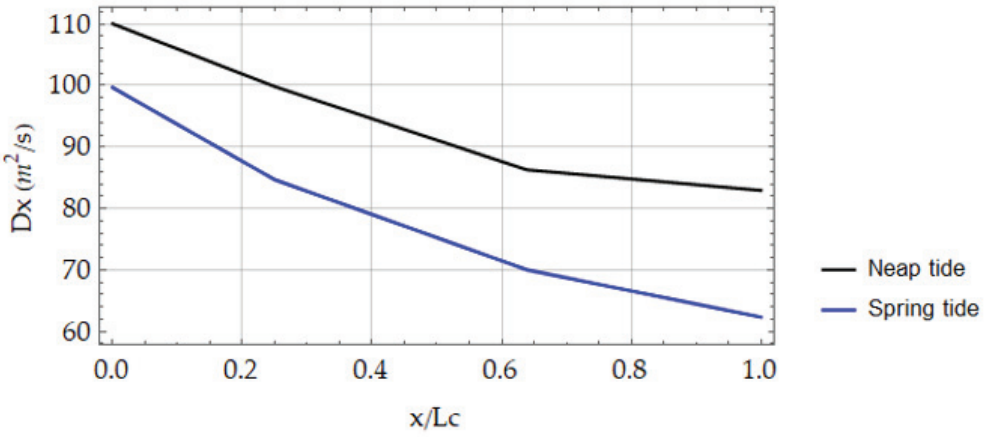

Figure 3.17 Longitudinal distributions of the dispersion coefficient deduced using the FAT system during spring tide and neap tide. "*x*" is the distance along the river from S_4 station, "L_c" is the longitudinal distance from S_4 to S_1 stations

Soltaniasl et al. (2013) decomposed a cross-sectional salt flux into five different components and grouped these into two categories: landward fluxes and seaward fluxes. Although Soltaniasl et al. (2013) did not address the salt dispersion attributable to gravitational circulation due to the lack of related data, in this study, the total salt flux in the Ōta River estuary is found to be controlled significantly by the two categories, with the magnitude of the former category (landward fluxes) measuring half of the later (seaward fluxes). This result shows a significant effect of the tide on the salt flux in the Ōta diversion channel. Furthermore, the channel is narrow and shallow, which is a state in which tide-driven shear mechanisms are often dominant (Savenije, 1993). Thus, the tide-driven mechanism may be the dominant mechanism in the dispersion process in the Ōta diversion channel.

3.6.6 Time delays of the phases of salinity variation

Figures 3.18 and 3.19 show the temporal variations in cross-sectional average salinity deduced from FATS and water level along the channel during a typical spring tide and neap tide, respectively. It is clearly seen that the phases of salinity variation lag behind the high water during both spring and neap tides.

To clarify the process and the reason of this phenomenon, the delays in time of the salinity peaks are calculating using cross-correlation method (see Chapter 2, Section 2.4.4)

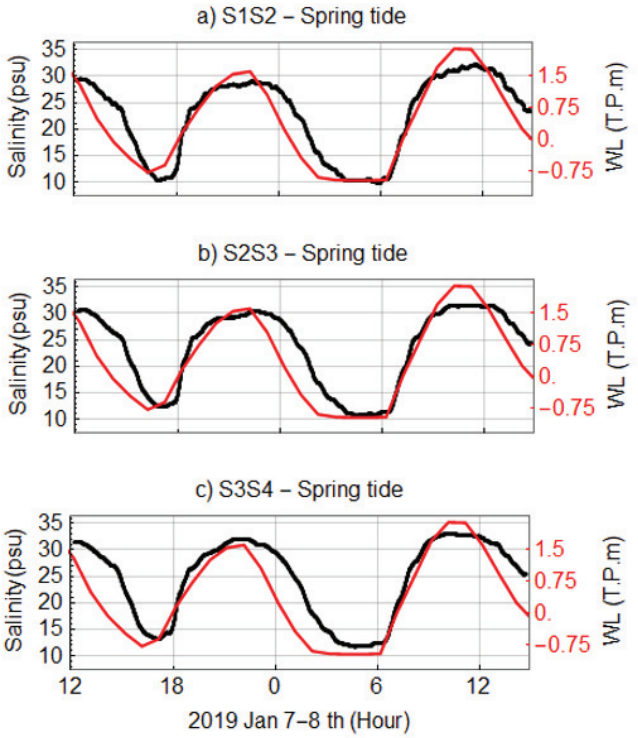

Figure 3.18 Temporal variations in cross-sectional average salinity (black lines) and water level (red lines) at the study site during a typical spring tide.

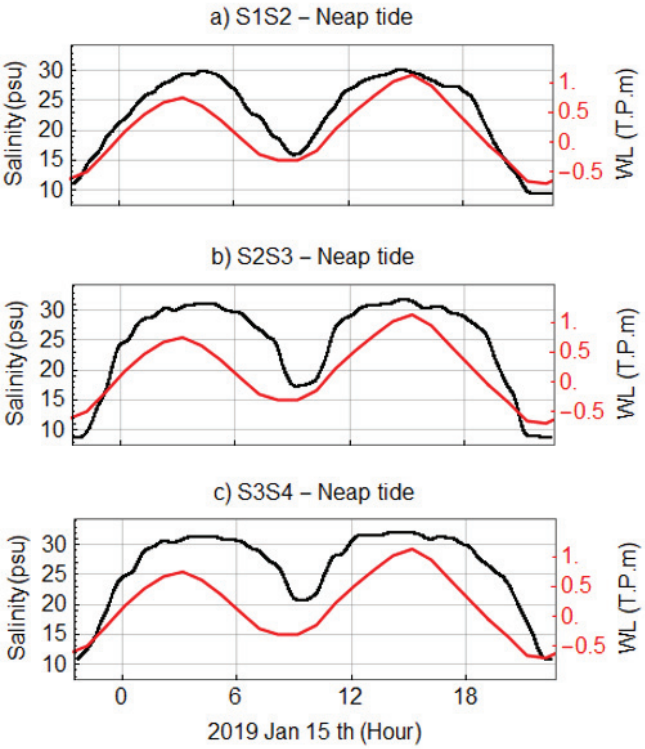

Figure 3.19 Temporal variations in cross-sectional average salinity (black lines) and water level (red lines) at the study site during a typical neap tide.

3.6.6.1 The effect of velocity on the travel time

The travel times, t_{up} and t_{down}, at the upstream and downstream stations were estimated, respectively, using the following equations:

$$t_{up} = \frac{L}{c - u};\ t_{down} = \frac{L}{c + u} \tag{3.12}$$

The travel times in the upstream and downstream sections are not equal due to the direction of flow velocities (seaward or landward). Normally, the mean speed of sound (c), and thus mean salinity, is estimated using the mean travel time, $t_m = (t_{up} + t_{down})/2$. However, in cases where one of the travel times is missing, t_{up} or t_{down} may be used to calculate the speed of sound, as the differences between travel times due to water velocity are small compared to the travel times.

On the S_1S_2 section, the sound transmitting data along the $S_1 \rightarrow S_2$ direction were more often lost than the data along the $S_2 \rightarrow S_1$ direction. Thus, the travel time data from the S_2 station to the S_1 station are used to calculate the salinity along the S_1S_2 section. Figure 3.20 shows the comparison between the cross-section average salinity estimated from the travel time t_{up} (denotes by black dots), and from the mean travel time t_m (denotes by red dots).

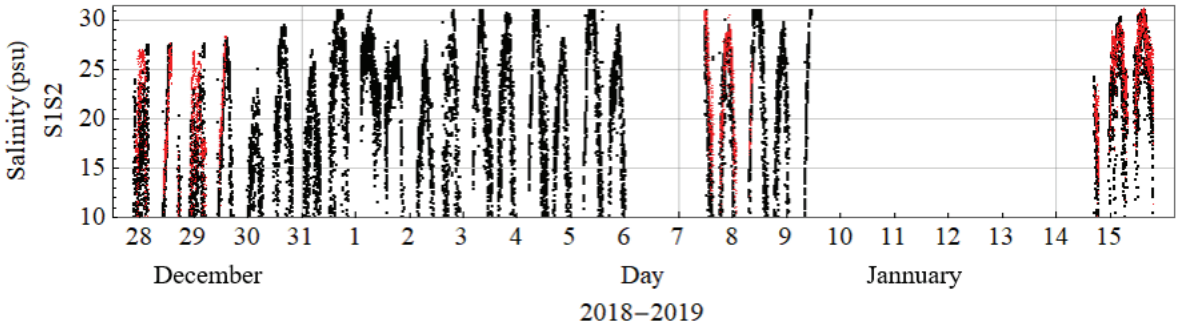

Figure 3.20 The cross-sectional average salinity at S_1S_2 section estimated from FATs, with the mean sound speed is calculated from the travel time t_{up} (black dots), and from the mean travel time t_m (red dots)

Figure 3.21 presents the salinity error induced by the salinity differences (d_S) between the salinity (S_{S1S2}) estimated from the mean travel time (t_m) and salinity estimated from the travel

time t_{up}. The salinity differences are small and the salinity error induced by the time differences between t_{up} and t_m is small as well, approximately 5%.

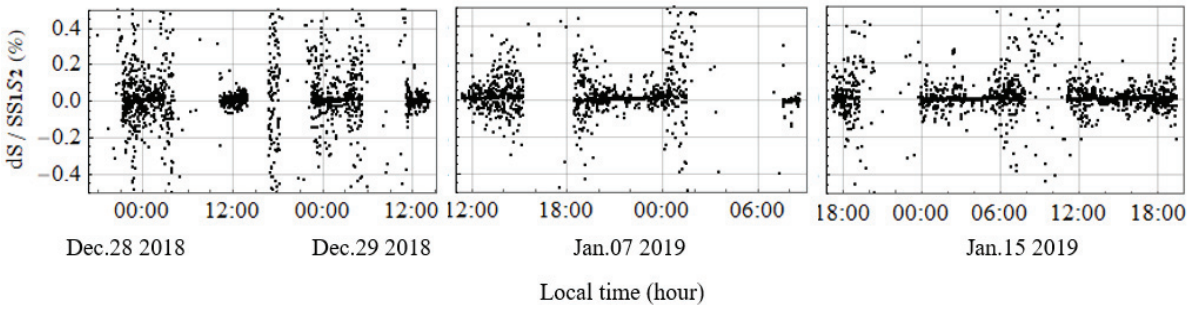

Figure 3.21 The salinity error induced by the time differences between the one way travel time and the mean travel time

3.6.6.2 The delays of the phases of salinity variation

In Figure 3.22, the black dots denote the temporal variations in the cross-sectional average salinities that are estimated from the water temperatures, water depth, and the mean of sound speed collected from FATs at two different cross-sections (S_1S_2 and S_3S_4), while red dots denote the salinities obtained by CT sensors deployed at the S_1 and S_4 stations, respectively. Compared to the stable trend of one-point salinities recorded at the S_1 and S_4 stations using a CT sensor, the cross-sectional average salinities deduced from the FAT data increases slightly at midday on December 31st 2018. The reason for these changes might be the change of freshwater discharge recorded at Yaguchi Station on December 31st 2018 (see Fig. 3.10). The time lags between the salinity maximum and the high water level were examined to clarify the effects of freshwater on the salinity variation.

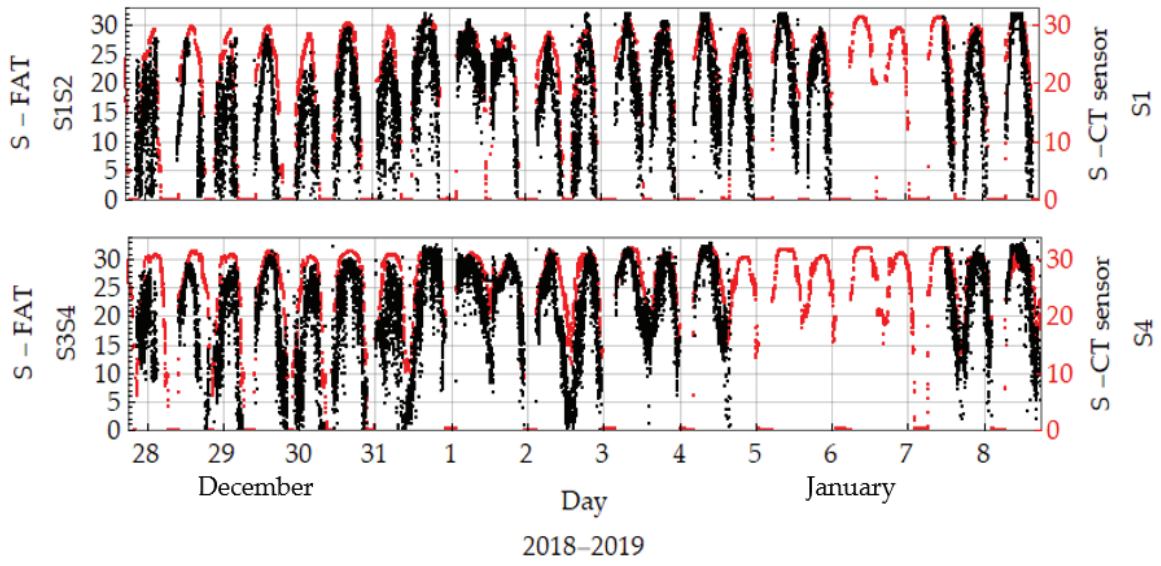

Figure 3.22 Temporal variation of salinity obtained using FAT (black points) at S_1S_2 and S_3S_4 transmission lines and CT sensors (red points) at S_1 and S_4 stations.

For further information, Table 3.4 illustrates the time lags and phase lags between the salinity and water level which are estimated from cross-correlation function (Fig. 2.2). Overall, it was evident that the time delay increased toward the mouth of the river, and the time shift changes significantly from before December 31st 2018 to after December 31st 2018, which is discussed as follow.

Table 3.4 Delays in time of salinity peaks.

S_1S_2 Section		S_2S_3 Section		S_3S_4 Section	
Time Lag (minute)	Phase Lag (°)	Time Lag (minute)	Phase Lag (°)	Time Lag (minute)	Phase Lag (°)
Before December 31st 2018					
14	6.73	17	8.17	28	13.46
21	10.10	27	12.98	37	17.79
15	7.21	24	11.54	31	14.90
12	5.77	24	11.54	36	17.31
16	7.69	26	12.50	40	19.23
After December 31st 2018					
22	10.58	31	14.90	87	41.83
32	15.38	26	12.50	94	45.19

23	11.06	42	20.19	91	43.75
21	10.10	38	18.27	55	26.44
23	11.06	37	17.79	97	46.63

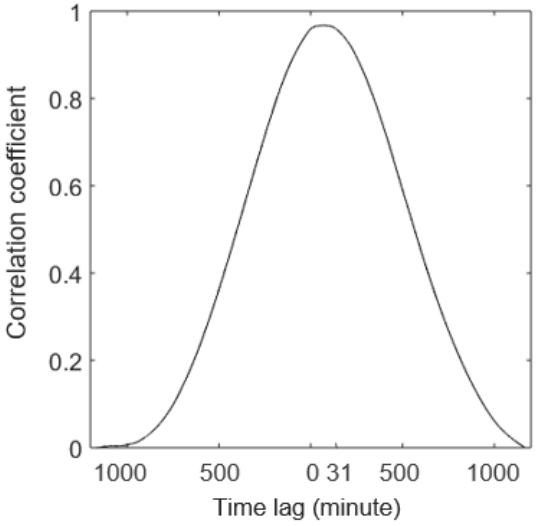

Figure 3.23 A typical cross-correlation function of salinity versus the water level

First of all, the time delay estimated in the downstream area (S_3S_4 section) is twice as high as the time delay in the upstream area (S_1S_2 section) over the study period. Moreover, the delay in the salinity maximum along the channel ranged from 12 min to approximately 1.5 h. All three sections of the channel significantly show higher time delays after 31st December 2018 than before this date.

In general, the delays found at the time of the salinity peaks are likely attributable to density current effects and cross-channel processes such as changes in water depth, differences in vertical velocities (both values and direction), and secondary flows (Dyer, 1973). In this research, the phase lags noted between the water level and salinity exist primarily because of the freshwater flows from the upstream. Figure 2.24 clearly shows a significant response between averaged time lag along the observation area and upstream freshwater discharge. Generally, the time lag is shorter corresponding with an increase in freshwater rate. In the middle of the day December 31st 2018, when upstream freshwater decreases from approximately 60 m^3/s to 20 m^3/s, time lag increases twice, from around 40 minutes to 80 minutes. Similarly, during the days after December 31st 2018, time lag decreases from approximately 65 minutes to 55 minutes when freshwater discharge increases from 20 m^3/s to 35 m^3/s. The shorter time lags are corresponding to the increase in freshwater discharge because

when freshwater flow increases, the impact of tidal velocity also increases, which enhances the salinity intrusion, and resulting in shorter time lag compared to that under the normal condition of freshwater flow (X. Chen et al., 2000).

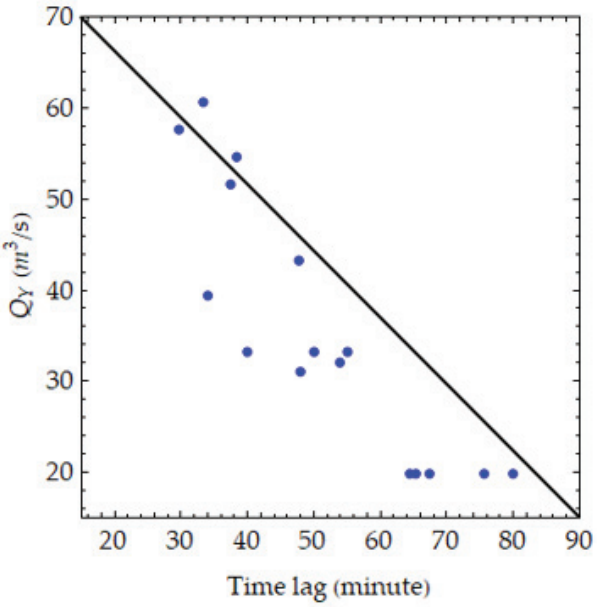

Figure 3.24 The association between freshwater discharge recorded at Yaguchi Gauging Station and delays in time of salinity in the observation site

3.7 Conclusions

This chapter presents longitudinal variation in salinity, tidal flow, and thus, salinity gradient, dispersion coefficient at the Ōta diversion channel. This research was designed to explore the effectiveness of using a novel and promising method of monitoring the continuous salinity intrusion and velocity distribution in a tidal channel using new FAT scheme. In detail, four FAT units were installed near the riverbanks using a new zigzag configuration in a rectangular tomographic domain of 700 m × 170 m.

The longitudinal distribution of intra-tidal changes in the velocity/discharge and salinity in the middle part of the diversion channel was monitored in this study. Velocity was measured concurrently using the FAT system and a moving-boat Stream-Pro ADCP. The section-average speed of sound was measured by placing four acoustic stations installed along the site study located on the broadest branch of the Ōta River system. The cross-sectional average salinity could be deduced from the water temperature, and the speed of sound from FAT using Medwin′s formula.

The results indicate that salinity in the Ōta diversion channel does not response to the water level fluctuations immediately. There are delays in time between the salinity and water level variations. The salinity response time lags ranged from 12 min to 1.5 h, corresponding to a phase lag range of 13°–47°. The time lag is closely related to the upstream freshwater release, with longer time lag corresponding with lower freshwater rate. Besides, the time lags increase seaward along the channel.

The differences in the section-average velocities obtained using FAT and ADCP were not significant. Moreover, the cross-sectional mean salinity derived using the FAT system was acceptably similar to the results obtained using the Compact CTD.

The studied section of the river exhibited asymmetric ebb-tide and flood-tide velocities, with a short-duration ebb phase of the tide and fast ebb currents that created an ebb-dominant phenomenon, which because of interaction of the $O_1 – K_1 – M_2$ tidal constituents, and the topographic effects.

The section-average salinity increased seaward, revealing typical estuarine behavior. In addition, the salinity pattern revealed a completely tide-dominated influence.

The longitudinal dispersion coefficient was found to increase toward the mouth of the river, and the tide-driven mechanism might be the dominant mechanism in the dispersion process in the Ōta diversion channel.

Finally, this study presents the detailed results of using a novel and promising method of continuous salinity and velocity distribution monitoring along a tidal channel.

CHAPTER 4 CONCLUSIONS AND RECOMMENDATIONS

4.1 Summary

The present study attempts to monitor the spatial and temporal variability in salinity and tidal flow in a shallow tidal estuary, with the Ōta Diversion channel, in Hiroshima, Japan as a case study. The research addresses the relationship between the distributions of salinity, water temperature, and water density in lateral and vertical dimensions. Besides, the present research also displays the distributions of salinity and tidal flow in longitudinal dimension under the variational estuarine forces such as freshwater release, tidal motion, and so on.

The three field observations are carried out in a river segment with the length of 850 m at the central part of the Ōta diversion channel (about 4.5 km from the estuary), they are:

(i) Two CTD campaigns in which the Conductivity-Temperature-Sensors (CTDs) are used with others instruments to measure the distribution of salinity, density and water temperature over both spring and neap tidal cycles. The vertical profiles of salinity, density and temperature are analyzed over two periods. The first observation is related to the neap tide of September 5, 2018 and the second observation is related to the spring tide of October 2, 2020.

(ii) A field observation was conducted with four FAT units installing near the riverbank using a new zigzag configuration. The purpose of the observation is to collect the data of tidal flow, water discharge, and salinity along the river segment. The field

observation is conducted during both neap and spring tides with the time period from December 26, 2018 to January 15, 2019.

With the results displayed in the above chapters, these objectives that are mentioned in the introduction section have been meet. As a consequence, the conclusions and recommendations are presented as follow:

4.2 Conclusions

4.2.1 Investigation of vertical and lateral distributions of salinity and density

By using the number and the depth of stratification layers as well as the vertical gradients of salinity and density deduced from the transverse and vertical distributions of salinity, the process of stratification/de-stratification in the Ōta diversion channel is evaluated. In detail, in the lateral and vertical dimensions, density driven is the main mechanism that controls the stratification in the Ōta diversion channel.

The new findings are that the stratification occurs during spring-ebb tides and early of neap-flood tides because of the combination of tidal straining, tidal asymmetry and freshwater inflow from upstream, while the lateral distribution of salinity appears during spring-flood tide and the late of neap-flood tides owing to the lateral density gradient. The study results also reveal that salinity dominates the density change in the Ōta diversion channel and the effect of temperature variation on salinity dynamics is not significant during the observation period.

The density distributions at the observation points have clear tidal cycle characteristics. The lateral density distributions are found at the end of the flood spring tides, and the vertical density distributions appear in the early of the ebb spring tides. During flood tides, the vertical density gradient increases in the central water column in the center of the stage. The onset of the phenomenon that shows vertical density gradient is stronger at the middle of the water column than that at the surface and the bottom parts can be controlled by the vertical straining due to the surface-to-bottom difference of transverse velocity. In addition, the turbulent mixing in the late of the flood tides decreases which maintains the lateral density gradient, and pushes the surface flows to the channel center and leading to lateral salinity distribution of the water column.

4.2.2 The longitudinal distributions of salinity and tidal flow

Both salinity and tidal flow patterns revealed a completely tide-dominated influence.

The tidal asymmetry (the ebb-tide velocities higher than flood-tide velocities) shows that the Ōta diversion channel is an ebb-dominant estuary. To consider the mechanisms that control this phenomenon, the relationship between the tidal constituents O_1, K_1 and M_2 is analyzed by using the harmonic analysis for observed tidal within the observation time period. The results of the tidal harmonic analysis show that $\phi_{u(O1)} = 191.3°$, $\phi_{u(K1)} = 219.67°$, and $\phi_{u(M2)} = 273.6°$, thus $\theta = cos\ (\phi_{u(O1)} + \phi_{u(K1)} + \phi_{u(M2)}) = -0.736$. This parameter suggests that the reasons for that ebb-dominant tidal phenomenon are the interaction of the $O_1 – K_1 – M_2$ tidal constituents.

This study investigates salinity and tidal flow distributions along the channel by using new configuration of FATs. Besides, the flow directions, and thus water discharge are estimated. The error structure for the river discharge measurement using that new configuration is analyzed in order to consider its feasibility. Four error components of this error structure are relative to the mean water depth; the imperfection of the bathymetry survey and the variations of the bottom shape; the velocity deduced from FATs; and the angle between the flow direction and the transmission line. The maximum probable value of that error structure is estimated as 17.5%. The small errors in the analyzed results suggest that the new zigzag configuration of FATs, which needs the lower instrument number, can be a cost-effective measurement method for monitoring estuarine physics.

The salinity in the Ōta diversion channel does not response to the water level fluctuations immediately: there are delays in time between the salinity and water level variations. The salinity response time lags ranged from 12 min to 1.5 h, corresponding to a phase lag range of 13°–47°. The time lags increase seaward along the channel, and decreases corresponding to the increase of the upstream freshwater flow. The shorter time lags are corresponding to the increase in freshwater discharge because when freshwater flow increases, the impact of tidal velocity also increases, which enhances the salinity intrusion, and resulting in shorter time lag compared to that under the normal condition of freshwater flow.

4.3 Novelties and new findings

- ✓ To find out the lateral circulation driven by the lateral density gradient leading to the lateral salinity gradient during flood tides;
- ✓ To improve the estuarine physics monitoring using the new zigzag configuration of FATs;

- ✓ To use a dimensionless parameter (number of stratification layers) and the stratification layer depth to evaluate the stratification/de-stratification degree in a tidal shallow estuary.

4.4 Recommendations

- ✓ This study addressed vertical and lateral distributions of salinity along a river segment with the length of 850m in the Ōta diversion channel during both neap and spring tides. The surface to bottom salinity differences at the two locations (upstream and downstream areas) of the observation site is expected to be different due to several contributions, i.e. bathymetry effects, longitudinal salinity gradient effects, horizontal density gradient effects. However, these differences were insignificant may due to the short distance of the observation site. Thus, a research on vertical distribution of salinity along the Ōta diversion channel with longer distance apart is recommended in the future.
- ✓ This study focused on the evaluation the transverse salinity dynamics through the stratification layer forming process, and the obtained data reflected good information about the transverse salinity dynamics. However, it will be interesting to see some quantitative analysis of the turbulent development from the velocity profile corresponding with salinity profile during a full tidal cycle. Thus, it is recommended to carry out a study in the future to consider the salinity dynamics base on vertical and lateral distributions of salinity as well as vertical and lateral distributions of velocity.

APPENDIX

The detailed equation of the relative errors of flow direction estimation:

$$\frac{\delta\theta}{\theta} = \frac{\delta\theta_{\emptyset}}{\theta} + \frac{\delta\theta_{A_1}}{\theta} + \frac{\delta\theta_{A_2}}{\theta} + \frac{\delta\theta_{u_1}}{\theta} + \frac{\delta\theta_{u_2}}{\theta}$$

where:

$$\frac{\delta\theta_{\emptyset}}{\theta} = 0.25\frac{-1.41\sqrt{A_1^2u_1^2 + 6A_1A_2u_1u_2 + A_2^2u_2^2 + (A_1u_1 - A_2u_2)^2Cos[2\emptyset]}Sin[\emptyset] - 2(-A_1u_1 + A_2u_2)Sin[2\emptyset] - \frac{1.41(A_1u_1 - A_2u_2)^2Cos[\emptyset]Sin[2\emptyset]}{\sqrt{A_1^2u_1^2 + 6A_1A_2u_1u_2 + A_2^2u_2^2 + (A_1u_1 - A_2u_2)^2Cos[2\emptyset]}}}{(A_1u_1 + A_2u_2)\theta},$$

$$\frac{\delta\theta_{A_1}}{\theta} = 0.25\frac{\frac{3u_1 - u_1Cos[2\emptyset] + \frac{0.7Cos[\emptyset](2A_1u_1^2 + 6A_2u_1u_2 + 2u_1(A_1u_1 - A_2u_2)^2Cos[2\emptyset])}{\sqrt{A_1^2u_1^2 + 6A_1A_2u_1u_2 + A_2^2u_2^2 + (A_1u_1 - A_2u_2)^2Cos[2\emptyset]}}}{A_1u_1 + A_2u_2} - \frac{u_1\left(3A_1u_1 + A_2u_2 + (-A_1u_1 + A_2u_2)Cos[2\emptyset] + 1.41Cos[\emptyset]\sqrt{A_1^2u_1^2 + 6A_1A_2u_1u_2 + A_2^2u_2^2 + (A_1u_1 - A_2u_2)^2Cos[2\emptyset]}\right)}{(A_1u_1 + A_2u_2)^2}}{\theta},$$

$$\frac{\delta\theta_{A_2}}{\theta} = 0.25\frac{\frac{u_2 + u_2Cos[2\emptyset] + \frac{0.7Cos[\emptyset](6A_1u_1u_2 + 2A_2u_2^2 - 2u_2(A_1u_1 - A_2u_2)Cos[2\emptyset])}{\sqrt{A_1^2u_1^2 + 6A_1A_2u_1u_2 + A_2^2u_2^2 + (A_1u_1 - A_2u_2)^2Cos[2\emptyset]}}}{A_1u_1 + A_2u_2} - \frac{u_2\left(3A_1u_1 + A_2u_2 + (-A_1u_1 + A_2u_2)Cos[2\emptyset] + 1.41Cos[\emptyset]\sqrt{A_1^2u_1^2 + 6A_1A_2u_1u_2 + A_2^2u_2^2 + (A_1u_1 - A_2u_2)^2Cos[2\emptyset]}\right)}{(A_1u_1 + A_2u_2)^2}}{\theta},$$

$$\frac{\delta\theta_{u_1}}{\theta} = 0.25\frac{\frac{3A_1 - A_1Cos[2\emptyset] + \frac{0.7Cos[\emptyset](2A_1^2u_1 + 6A_1A_2u_2 + 2A_1(A_1u_1 - A_2u_2)\,Cos[2\emptyset])}{\sqrt{A_1^2u_1^2 + 6A_1A_2u_1u_2 + A_2^2u_2^2 + (A_1u_1 - A_2u_2)^2Cos[2\emptyset]}}}{A_1u_1 + A_2u_2} - \frac{A_1\left(3A_1u_1 + A_2u_2 + (-A_1u_1 + A_2u_2)Cos[2\emptyset] + 1.41Cos[\emptyset]\sqrt{A_1^2u_1^2 + 6A_1A_2u_1u_2 + A_2^2u_2^2 + (A_1u_1 - A_2u_2)^2Cos[2\emptyset]}\right)}{(A_1u_1 + A_2u_2)^2}}{\theta},$$

$$\frac{\delta\theta_{u_2}}{\theta} = 0.25\frac{\frac{A_2 + A_2Cos[2\emptyset] + \frac{0.7Cos[\emptyset](6A_1A_2u_1 + 2A_2^2u_2 - 2A_2(A_1u_1 - A_2u_2)\,Cos[2\emptyset])}{\sqrt{A_1^2u_1^2 + 6A_1A_2u_1u_2 + A_2^2u_2^2 + (A_1u_1 - A_2u_2)^2Cos[2\emptyset]}}}{A_1u_1 + A_2u_2} - \frac{A_2\left(3A_1u_1 + A_2u_2 + (-A_1u_1 + A_2u_2)Cos[2\emptyset] + 1.41Cos[\emptyset]\sqrt{A_1^2u_1^2 + 6A_1A_2u_1u_2 + A_2^2u_2^2 + (A_1u_1 - A_2u_2)^2Cos[2\emptyset]}\right)}{(A_1u_1 + A_2u_2)^2}}{\theta}$$

REFERENCES

Al Sawaf, M. B., Kawanisi, K., & Xiao, C. (2020). Measuring Low Flowrates of a Shallow Mountainous River Within Restricted Site Conditions and the Characteristics of Acoustic Arrival Times Within Low Flows. *Water Resources Management*, *34*(10), 3059–3078. https://doi.org/10.1007/s11269-020-02557-w

Bahreinimotlagh, M., Kawanisi, K., Danial, M. M., Al Sawaf, M. B., & Kagami, J. (2016). Application of shallow-water acoustic tomography to measure flow direction and river discharge. *Flow Measurement and Instrumentation*, *51*, 30–39. https://doi.org/10.1016/j.flowmeasinst.2016.08.010

Bain, R. L., Hale, R. P., & Goodbred, S. L. (2019). Flow Reorganization in an Anthropogenically Modified Tidal Channel Network: An Example From the Southwestern Ganges-Brahmaputra-Meghna Delta. *Journal of Geophysical Research: Earth Surface*, *124*(8), 2141–2159. https://doi.org/10.1029/2018JF004996

Boon, J. D., & Byrne, R. J. (1981). On basin hyposmetry and the morphodynamic response of coastal inlet systems. *Marine Geology*, *40*(1–2), 27–48. https://doi.org/10.1016/0025-3227(81)90041-4

Chen, Q., Zhu, J., Lyu, H., Pan, S., & Chen, S. (2019). Impacts of topography change on saltwater intrusion over the past decade in the Changjiang Estuary. *Estuarine, Coastal and Shelf Science*, *231*(January), 106469. https://doi.org/10.1016/j.ecss.2019.106469

Chen, X., Flannery, M. S., & Moore, D. L. (2000). Response times of salinity in relation to changes in freshwater inflows in the Lower Hillsborough River, Florida. *Estuaries*, *23*(5), 735–742. https://doi.org/10.2307/1352899

Conroy, T., Sutherland, D. A., & Ralston, D. K. (2020). Estuarine exchange flow variability in a seasonal, segmented estuary. *Journal of Physical Oceanography*, *50*(3), 595–613. https://doi.org/10.1175/JPO-D-19-0108.1

DYER, K. R. (1973). *Estuaries: a Physical Introduction* (2nd ed., Issue (1973)).

Dyer, K. R., Gong, W. K., & Ong, J. E. (1992). The cross sectional salt balance in a tropical estuary during a lunar tide and a discharge event. *Estuarine, Coastal and Shelf Science*, *34*(6), 579–591. https://doi.org/10.1016/S0272-7714(05)80063-0

Fischer. H.B. (1976). *Mixing and Dispersion in Estuaries*. 107–133. https://doi.org/10.1017/cbo9780511813177.015

Fischer, H. (1972). Mass transport mechanisms in partially stratified estuaries. *J. Fluid Mech.*,

53, 671–687.

Fitzgerald, D. M., & Nummedal, D. A. G. (1983). Response characteristics of an ebb-dominated tidal inlet channel. *Sedimentary Petrology*, *53*(3).

Garel, E., & D'Alimonte, D. (2017). Continuous river discharge monitoring with bottom-mounted current profilers at narrow tidal estuaries. *Continental Shelf Research*, *133*, 1–12. https://doi.org/10.1016/j.csr.2016.12.001

Geawhari, M. A., Huff, L., Mhammdi, N., Trakadas, A., & Ammar, A. (2014). Spatial-temporal distribution of salinity and temperature in the Oued Loukkos estuary, Morocco: using vertical salinity gradient for estuary classification. *Computational Statistics*, *3*(1), 1–9. https://doi.org/10.1186/2193-1801-3-643

Geyer, W. R., & MacCready, P. (2014). The estuarine circulation. *Annual Review of Fluid Mechanics*, *46*, 175–197. https://doi.org/10.1146/annurev-fluid-010313-141302

Gotoh, T., Fukuoka, S., & Miyagawa, Y. (2013). *Topographic changes of tidal flats in the Ota River estuary by flood flows*. 1337–1345.

Gusti, G. N. N., & Kawanisi, K. (2020). the Influence of Flood Control Structure on Secondary Flow Dynamics in a Meandering Tidal Estuarine Channel. *Journal of Japan Society of Civil Engineers, Ser. B1 (Hydraulic Engineering)*, *76*(2), I_1393-I_1398. https://doi.org/10.2208/jscejhe.76.2_i_1393

Hoitink, A. J. F., Hoekstra, P., & Van Maren, D. S. (2003). Flow asymmetry associated with astronomical tides: Implications for the residual transport of sediment. *Journal of Geophysical Research: Oceans*, *108*(10), 1–8. https://doi.org/10.1029/2002jc001539

Jay, D. A., & Smith, J. D. (1990). Residual circulation in shallow estuaries: 2. Weakly stratified and partially mixed, narrow estuaries. *Journal of Geophysical Research*, *95*(C1), 733. https://doi.org/10.1029/jc095ic01p00733

Kang, J. W., & Jun, K. S. (2003). Flood and ebb dominance in estuaries in Korea. *Estuarine, Coastal and Shelf Science*, *56*(1), 187–196. https://doi.org/10.1016/S0272-7714(02)00156-7

Kawanisi, K., Al Sawaf, M. B., & Danial, M. M. (2018). Automated real-time stream flow acquisition in a mountainous river using acoustic tomography. *Journal of Hydrologic Engineering*, *23*(2). https://doi.org/10.1061/(ASCE)HE.1943-5584.0001604

Kawanisi, Kiyosi, Bahrainimotlagh, M., Al Sawaf, M. B. B., Razaz, M., M.B., M. B., & Razaz, M. (2016). High-frequency streamflow acquisition and bed level/flow angle estimates in a mountainous river using shallow-water acoustic tomography. *Hydrological Processes*,

30(13), 2247–2254. https://doi.org/10.1002/hyp.10796

Kawanisi, Kiyosi, Razaz, M., & Bahreinimotlagh, M. (2015). Monitoring Flow Rate and Salinity Intrusion in a Tidal Floodway Using Fluvial Acoustic Tomography. *36th World Congress of the International Association of Hydro-Environment Engineering and Research (IAHR-APD 2015), The Hague, The Netherlands*, *Figure 1*, 1–8.

Kawanisi, Kiyosi, Razaz, M., Kaneko, A., & Watanabe, S. (2010). Long-term measurement of stream flow and salinity in a tidal river by the use of the fluvial acoustic tomography system. *Journal of Hydrology*, *380*(1–2), 74–81. https://doi.org/10.1016/j.jhydrol.2009.10.024

Kawanisi, Kiyosi, Razaz, M., Soltaniasl, M., Kaneko, A., Kawanishi, K., & Hiroshima, H. (2011). Long-Term Salinity Measurement in a Tidal Estuary By the Use of Acoustic Tomography. *4th International Conference and Exhibition on Underwater Acoustics*, 401–408.

Kawanisi, Kiyosi, Zhu, X. H., Fan, X., & Nistor, I. (2017). Monitoring Tidal Bores using Acoustic Tomography System. *Journal of Coastal Research*, *33*(1), 96–104. https://doi.org/10.2112/JCOASTRES-D-15-00172.1

Kenneth Hunkins. (1981). *Salt dispersion in the Hudson Estuary*.

Lacy, J. R., Stacey, M. T., Burau, J. R., & Monismith, S. G. (2003). Interaction of lateral baroclinic forcing and turbulence in an estuary. *Journal of Geophysical Research: Oceans*, *108*(3), 1–15. https://doi.org/10.1029/2002jc001392

Laenen, A., & Smith, W. (1983). *Acoustic systems for the measurement of streamflow.*

Lerczak, J. A., & Geyer, W. R. (2004). Modeling the lateral circulation in straight, stratified estuaries. *Journal of Physical Oceanography*, *34*(6), 1410–1428. https://doi.org/10.1175/1520-0485(2004)034<1410:MTLCIS>2.0.CO;2

Li, L., Zhu, J., & Wu, H. (2012). Impacts of wind stress on saltwater intrusion in the Yangtze Estuary. *Science China Earth Sciences*, *55*(7), 1178–1192. https://doi.org/10.1007/s11430-011-4311-1

Maghrebi, M. F., Ahmadi, A., Attari, M., & Maghrebi, R. F. (2016). New method for estimation of stage-discharge curves in natural rivers. *Flow Measurement and Instrumentation*, *52*, 67–76. https://doi.org/10.1016/j.flowmeasinst.2016.09.008

Martyr-Koller, R. C., Kernkamp, H. W. J., van Dam, A., van der Wegen, M., Lucas, L. V., Knowles, N., Jaffe, B., & Fregoso, T. A. (2017). Application of an unstructured 3D finite volume numerical model to flows and salinity dynamics in the San Francisco Bay-Delta.

Estuarine, Coastal and Shelf Science, *192*, 86–107. https://doi.org/10.1016/j.ecss.2017.04.024

McManus, J. (2005). Salinity and suspended matter variations in the Tay estuary. *Continental Shelf Research*, *25*(5–6), 729–747. https://doi.org/10.1016/j.csr.2004.11.003

Medwin, H. (1975). Speed of sound in water: A simple equation for realistic parameters. *Journal Acoustical Society of America*, *6*, 1318–1319.

Millero, F. J., & Poisson, A. (1981). International one-atmosphere equation of state of seawater. *Deep Sea Research Part A, Oceanographic Research Papers*, *28*(6), 625–629. https://doi.org/10.1016/0198-0149(81)90122-9

Nguyen, H. T., & Kawanisi, K. (2021). *Acoustic Monitoring of Tidal Flow and Salinity in a Tidal Channel*.

Nunes, R. A., & Simpson, J. H. (1985). Axial convergence in a well-mixed estuary. *Estuarine, Coastal and Shelf Science*, *20*(5), 637–649. https://doi.org/10.1016/0272-7714(85)90112-X

Prandle, D. (2006). Dynamical controls on estuarine bathymetry: Assessment against UK database. *Estuarine, Coastal and Shelf Science*, *68*(1–2), 282–288. https://doi.org/10.1016/j.ecss.2006.02.009

Ralston, D. K., Geyer, W. R., & Lerczak, J. A. (2010). Structure, variability, and salt flux in a strongly forced salt wedge estuary. *Journal of Geophysical Research: Oceans*, *115*(6), 1–21. https://doi.org/10.1029/2009JC005806

Razaz, M., Kawanisi, K., Kaneko, A., & Nistor, I. (2015). Application of acoustic tomography to reconstruct the horizontal flow velocity field in a shallow river. *Water Resources Research*, *51*(12), 9665–9678. https://doi.org/10.1002/2015WR017102

Razaz, M., Kawanisi, K., Nistor, I., & Sharifi, S. (2013). An acoustic travel time method for continuous velocity monitoring in shallow tidal streams. *Water Resources Research*, *49*(8), 4885–4899. https://doi.org/10.1002/wrcr.20375

Robins, P. E., & Davies, A. G. (2009). Morphodynamic processes in shallow estuaries: Influence of tidal flats and channels on sand transport. *RCEM2009: The 6th IAHR Symposium on River, Coastal and Estuarine Morphodynamics*, *January 2009*, 161–167.

Savenije, H. H. G. (1993). Composition and driving mechanisms of longitudinal tidal average salinity dispersion in estuaries. *Journal of Hydrology*, *144*(1–4), 127–141. https://doi.org/10.1016/0022-1694(93)90168-9

Schumann, R., Baudler, H., Glass, Ä., Dümcke, K., & Karsten, U. (2006). Long-term

observations on salinity dynamics in a tideless shallow coastal lagoon of the Southern Baltic Sea coast and their biological relevance. *Journal of Marine Systems*, *60*(3–4), 330–344. https://doi.org/10.1016/j.jmarsys.2006.02.007

Scully, M. E., & Geyer, W. R. (2012). The Role of Advection, Straining, and Mixing on the Tidal Variability of Estuarine Stratification. *Journal of Physical Oceanography*, *42*(5), 855–868. https://doi.org/10.1175/JPO-D-10-05010.1

Simpson, J. H., Brown, J., Matthews, J., & Allen, G. (1990). Tidal straining, density currents, and stirring in the control of estuarine stratification. *Estuaries*, *13*(2), 125–132. https://doi.org/10.2307/1351581

SOLTANIASL, M., KAWANISI, K., & RAZAZ, M. (2013). Investigation of Salt Intrusion Variability Using Acoustic Tomography System. *Journal of Japan Society of Civil Engineers, Ser. B1 (Hydraulic Engineering)*, *69*(4), I_91-I_96. https://doi.org/10.2208/jscejhe.69.i_91

Soltaniasl, M., Kawanisi, K., Yano, J., & Ishikawa, K. (2013). Variability in salt flux and water circulation in Ota River Estuary, Japan. *Water Science and Engineering*, *6*(3), 283–295. https://doi.org/10.3882/j.issn.1674-2370.2013.03.005

Song, D., Wang, X. H., Kiss, A. E., & Bao, X. (2011). The contribution to tidal asymmetry by different combinations of tidal constituents. *Journal of Geophysical Research: Oceans*, *116*(12), 1–12. https://doi.org/10.1029/2011JC007270

Stacey, M. T., Fram, J. P., & Chow, F. K. (2008). Role of tidally periodic density stratification in the creation of estuarine subtidal circulation. *Journal of Geophysical Research: Oceans*, *113*(8), 1–13. https://doi.org/10.1029/2007JC004581

Valle-Levinson, A., & Lwiza, K. M. M. (1997). Bathymetric influences on the lower Chesapeake Bay hydrography. *Journal of Marine Systems*, *12*(1–4), 221–236. https://doi.org/10.1016/S0924-7963(96)00099-1

Vaz, N., Dias, J. M., Leitão, P., & Martins, I. (2005). Horizontal patterns of water temperature and salinity in an estuarine tidal channel: Ria de Aveiro. *Ocean Dynamics*, *55*(5–6), 416–429. https://doi.org/10.1007/s10236-005-0015-4

Wang, Q., Golden, B. L., Wasil, E. A., & Dinardo, G. (1992). Modeling Salinity Dynamics in the Chesapeake Bay. *American Journal of Mathematical and Management Sciences*, *12*(2–3), 227–247. https://doi.org/10.1080/01966324.1992.10737332

Xiao, C., Kawanisi, K., Torigoe, R., & Al Sawaf, M. B. (2021). Mapping tidal current and salinity at a shallow tidal channel junction using the fluvial acoustic tomography system.

Estuarine, Coastal and Shelf Science, *258*(November 2020), 107440. https://doi.org/10.1016/j.ecss.2021.107440

LIST OF FIGURES

LIST OF TABLES

NOTATIONS AND ABBREVIATIONS

Symbols

A	Cross-section area along the ray path (L^2)
B	Cross-section length of the channel (L)
D_x	Longitudinal dispersion coefficient (-)
c	Sound speed (LT^{-1})
D	Water depth (L)
E	Expected value of variance (-)
H	Water level (L)
K_1	The diurnal tidal constituent
L	The distance between the upstream and downstream stations (L)
M_2	The principal semidiurnal lunar constituent.
O_1	The diurnal tidal constituent
$Q_{Y1,2}$	Fresh water discharge (L^3T^{-1})
Q	Water discharge (L^3T^{-1})
R^2	Determination coefficient (-)
S	Section-averaged salinity (psu)
$S_{1,2,3,4}$	Name of the acoustic stations (-)
S_1S_2	Name of the transmission line between S_1, S_2 stations (-)
S_2S_3	Name of the transmission line between S_2, S_3 stations (-)
S_3S_4	Name of the transmission line between S_3, S_4 stations (-)
T	Temperature along the ray path (C)
t	Time (T)
t_{up}	Travel times in the upstream section (T)
T_{down}	Travel times in the downstream section (T)
u	Mean velocity along the transmission line (LT^{-1})

V	Section-averaged velocity (LT^{-1})
X	Random variable (-)
$\bar{X}$	Mean of random variable X (-)
$X_{1,2}$	Coordinates of the acoustic stations
Y	Random variable (-)
$\bar{Y}$	Mean of random variable Y (-)
$Y_{1,2}$	Coordinates of the acoustic stations
x	Longitudinal distance (L)
y	Lateral distance (L)
z	Vertical distance (L)
τ	Time lag (T)
θ	Angle between the ray path and streamline
ϕ	Angle between two transmission lines
$\phi_{u(O1)}$	The phase of O_1 tidal constituent
$\phi_{u(K1)}$	The phase of K_1 tidal constituent
$\phi_{u(M2)}$	The phase of M_2 tidal constituent

Abbreviations

ADCP	Acoustic Doppler Current Profiler
CTD	Conductivity- Temperature- Depth sensor
CT	Conductivity-Temperature sensor
FATs	Fluvial Acoustic Tomography system
HWL	Highest Water Level
LWL	Lowest Water Level
RMSE	Root Mean Square Error
T.P	The average water level in Tokyo Bay